The boundary layer on a sharp cone in high-enthalpy flow

Thesis by

Patrick Germain

In Partial Fulfillment of the Requirements

for the Degree of

Doctor of Philosophy

California Institute of Technology

Pasadena, California

1994

(Submitted November 5, 1993)

to my parents, Jacqueline and Lucipe.

Acknowledgments

I would like to thank my advisor, Dr. Hans G. Hornung, for his support and ideas during the course of this project at GALCIT.

I would also like to thank Karen Cheetham, Dr. Hornung's secretary. I have appreciated the help of the Aero machine shop staff: George Lundgren (now retired), Joe Haggerty, Larry Frazier, and Phil Wood. I have also appreciated the help of the T5 team members: Eric Cummings, Jacques Bélanger, Simon Sanderson, Chih-yung Wen, Bernard Rousset, and Bahram Valiferdowsi. I am particularly thankful to Eric for the time he spent on the design of the tunable dye-laser, and to Simon for the time he spent on implementing the data acquisition system.

This work was supported by NASA Grant NAG-1-1209 (Dr. Griffin Anderson), and by AFOSR Grant F49610-92-J-0110 (Dr. Leonidis Sakell). I would like to thank Roger Campbell, John Medley and Jim Davis (Rocketdyne Division of Rockwell International Corporation) for use of the thermocouple sensors.

Finally, I would like to acknowledge the Natural Sciences and Engineering Research Council of Canada (NSERC) for support of the first four years of my study and the Fonds pour la Formation de Chercheurs et l'Aide à la Recherche (FCAR) of the province of Québec for tuition support of the first two years.

Abstract

An exploratory study of the laminar, transitional and turbulent boundary layer on a 5 deg. half-angle cone in hypervelocity flow was conducted in the high-enthalpy shock tunnel T5 by measurement of the heat flux distribution and by qualitative flow visualization. A novel flow visualization technique using sodium seeding to increase the sensitivity of conventional interferometric techniques by resonant enhancement of the refractivity of the medium was developed to study the boundary layer structure. The experiments were designed to cover a large range of specific reservoir enthalpy, ranging from the perfect-gas regime to the range where significant oxygen and some nitrogen dissociation and recombination effects may be expected in the boundary layer. The presence of atomic species is due to the combined effect of nozzle freezing and frictional heating in the boundary layer. In the laminar regime and in the latter range, the following effects were found to be present: At the same nominal conditions, heat flux levels are higher in air than in nitrogen because of a larger heat release from oxygen recombination at the wall. By varying the reservoir specific enthalpy in air and nitrogen, and from measurements in carbon dioxide, it was found that real-gas effects stabilize the boundary layer. If the transition Reynolds number is renormalized by evaluating it at the reference temperature, the data for a given gas becomes correlated in a plot against reservoir enthalpy. Increasing enthalpy stabilizes the flow. The stabilizing effect is stronger with gases whose lowest activation energy is low. This behavior is opposite to the prediction made by the linear stability theory regarding the second linear mode of instability. The linear stability theory predicts, however, that real-gas effects stabilize the Tollmien-Schlichting mode. Flow visualization results suggest that the dominant instability mode in the present experiments was the Tollmien-Schlichting mode. Finally, the flow visualization pictures show structures that are not qualitatively different from those of an incompressible turbulent boundary layer, but they do not indicate if real-gas effects change significantly the structure of the turbulent boundary layer. The heat transfer measurements compare well with semi-empirical predictions.

Table of contents

List of figures

List of tables

List of symbols

Latin symbols

A	area; amplitude of a disturbance wave
C	compressibility correction factor (laminar regime)
c	complex phase velocity; specific heat of a solid material
c_f	skin friction coefficient
c_p	specific heat of a gas at constant pressure
D	dissociation energy per molecule
$\mathcal{D}$	diffusion coefficient of the species
e	difference between a prediction and an experimental datum at the same Re
F	dimensionless frequency ($\equiv 2\pi f/(u_e^2\rho_e/\mu_e)$)
f	frequency of a disturbance wave
f'	u/u_m
F_c	compressibility correction factor (turbulent regime)
g	h/h_m
h	enthalpy
$\mathcal{K}$	atomic species production rate coefficient
k	heat conductivity
k_b	Boltzmann constant
k_r	recombination reaction rate
L	dummy coefficient
Le	Lewis number
M	Mach number
m	atomic weight of a species
p	pressure
Pr	Prandtl number
Q	general flow property; integrated heat

$\overline{Q}$	average value of Q
$\dot{q}$	heat transfer rate
R	gas constant; $\sqrt{Re}$
r	recovery factor
Re	Reynolds number
S	temperature constant ($\equiv$ 111 K)
Sc	Schmidt number
St	Stanton number
T	temperature
$T1$	dummy coefficient
$T2$	dummy coefficient
t	time variable
u	velocity component along the x-direction
v	velocity component along the y-direction
x	distance from the tip of the cone along the centerline
y	direction normal to the flow direction and the model surface
z	direction normal to x and y

Greek symbols

α	angle of attack; growth rate of a disturbance; atomic mass fraction
α_{diff}	thermal diffusivity, ($\equiv k/(\rho/c)$)
γ	ratio of specific heats of a gas
δ	thickness of the boundary layer
η	similarity variable, ($\equiv \frac{u_e}{\sqrt{2\xi}} \int_0^y \rho \mathrm{d}y$)
θ	roll position
θ_d	characteristic temperature for dissociation
μ	viscosity (obtained from Sutherland's law)
ξ	similarity variable, ($\equiv \rho_e \mu_e u_e x$)
ς	dummy variable

ρ	density
ρ_d	characteristic density for dissociation
σ	dummy variable
ϕ	rate at which atoms are recombining (in m/s)
ψ	angle between a plane wave propagation direction and the x-direction; stream function
Ω	dimensionless reaction rate parameter

Superscript symbols

$'$	fluctuating component
$cone$	on a cone
$planar$	inside a hollow cylinder
*	based on the reference temperature T^*; throat location

Subscript symbols

0	reservoir, stagnation or total (in the case of h: specific)
∞	free stream or upstream of the shock layer
aw	adiabatic wall or recovery
c	heat transfer by conduction
e	outer edge of the boundary layer
i	imaginary part
inc	incompressible
m	point of maximum static temperature or enthalpy inside the boundary layer
max	maximum value
$peak\ tr$	peak of transition
r	heat transfer by atomic species diffusion
t	turbulent
tr	beginning of transition
w	wall

CHAPTER 1

Introduction

1.1 Background and problem statement

During the last three decades, there has been an interest in studying the aerodynamics of vehicles reentering the Earth's atmosphere at orbital speeds up to 7 km/s and a need to understand the behavior of the air flow around these vehicles. Recently, this interest has grown as there is also a need to understand the aerodynamics of single-stage-to-orbit vehicles and of planetary probes entering the atmospheres of other planets such as Mars.

The peculiarities of the gas behavior need to be understood in an experimental simulation which has to be performed with the same gas as in the real flow and at the same speed. These peculiarities are called 'real-gas effects' and they appear when the flow kinetic energy of the molecules becomes comparable to their specific dissociation energy: for instance as they are brought to rest on the skin of an object, the excess of their energy is dissipated in the form of frictional heat therefore raising the local temperature. Dissociation occurs and, even in thermodynamic equilibrium, the gas can no longer be considered a perfect gas. When the rate of this dissociation is finite, a time scale (which is a property of the gas) is introduced. This peculiarity is called a 'nonequilibrium effect'. When the total enthalpy of the flow is high enough to bring about such real-gas effects, it is called a 'high-enthalpy flow'.

One of the fundamental projects in the field of fluid mechanics is the study of the boundary layer. This project includes for example the transition mechanism from the laminar to the turbulent regime and the structure of the zero pressure-gradient boundary layer. The ultimate goal is to find out how and at what levels the friction and heat loads are distributed

on the body. For subsonic and supersonic flow regimes, the distribution of these loads is relatively well understood from an engineer's point of view.

This project is an extension of boundary layer studies for high-enthalpy flows which are generated by a free-piston shock tunnel. For a short time (in the order of a few milliseconds), this kind of wind tunnel is capable of producing flows of air or nitrogen up to specific reservoir enthalpy, h_0, of 25 MJ/kg at reservoir pressure, p_0, up to 100 MPa. This means that the Reynolds number, Re, on a slender cone of 1 m length at Mach number 5 can be as high as 10 million at h_0 = 8 MJ/kg and 2 million at h_0 = 25 MJ/kg. The model used in this experiment is a 5 deg. half-angle cone at zero-angle of incidence.

1.2 Review of earlier work

In this section, an overview of the literature is divided into three parts. The first part covers the laminar boundary layer studied by researchers who have access to other high enthalpy wind tunnels. One should refer for example to Schlichting (1979) which covers earlier work on perfect-gas compressible boundary layers. Some of these investigations are mentioned in the next chapter. The second part covers the work done to study the transition process of a compressible boundary layer. Most of the previous experimental work does not include real-gas effects but provides insight into the physical process of transition. The third part covers the compressible turbulent boundary layer. The studies done on this subject show some peculiarities due to compressibility but none due to nonequilibrium chemistry.

1.2.1 Laminar boundary layer

A mathematical solution of the conservation equations for a laminar boundary layer on a flat plate at zero-angle of attack was obtained ninety years ago by Blasius. The flow considered was incompressible and the velocity field just outside the boundary layer was assumed constant everywhere. Since then, more general solutions were obtained by relaxing some of the assumptions. Mathematical solutions have also been found for compressible flows. As chemical effects are introduced, the problem becomes more complicated and solutions must be obtained by numerical computations. Blottner (1964) considered a hypersonic flow of a binary mixture of atoms and molecules with finite reaction rates on a flat plate and on a cone. At high Re (on the order of 1 to 10 million), the boundary layer on a cone can be very thin with respect to the radius of curvature of the wall. Also, the pressure gradient is zero, so that many of the flow properties are similar to those of a flow on a flat plate. Fig. 1.1 shows that a perfect gas would reach a higher maximum temperature (shown by the nonequilibrium profile corresponding to $x = 0$) than a gas in chemical equilibrium. This difference is due to the dissociation reactions taking place in the outer part of the boundary layer which are endothermic (the reaction process absorbs heat). Near the cold wall, the slower exothermic recombination reactions take place to a certain degree depending (among other conditions) on the catalyticity of the cold wall: whether or not its material has an influence on the rate of the recombination reactions. Blottner assumed a fully catalytic wall for his computations. It is presumed that this boundary condition affects the species concentration profiles throughout the boundary layer and the heat transfer rate at the wall. Fig. 1.1 also shows that, as x increases, the maximum-temperature decreases and the temperature profile comes close to that of a gas in chemical equilibrium.

It is very difficult to determine experimentally the degree of nonequilibrium inside the boundary layer. Without disturbing the flow, one would need to measure the static temperature and the local composition of the gas. While modern non-intrusive optical diagnostic methods are promising, such as PLIF (Planar Laser Induced Fluorescence), no reference has been found where they are applied to high-enthalpy boundary layers. The following two experiments were nevertheless conducted in such facilities.

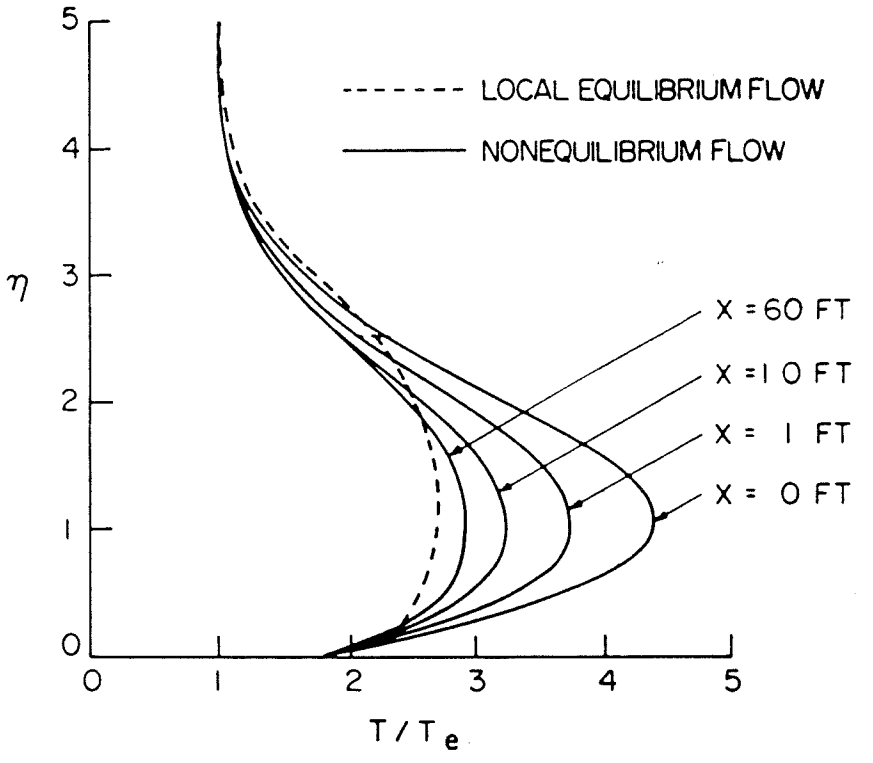

FIG. 1.1. Temperature profiles of an air flow on a 5 deg. half-angle cone with $u_e = 6,280$ m/s and $T_e = 1,100$ K. η is a similarity variable ($\equiv (u_e/\sqrt{2\rho_e\mu_e u_e x}\int_0^y \rho dy)$. x is the distance from the cone tip along the centerline. Taken from Blottner (1964).

Vidal and Golian (1967) instrumented a flat plate with thin-film heat transfer gauges and exposed it to a flow of pure oxygen in a shock tube facility. By coating the gauges with catalytic and non-catalytic materials, they observed different heat transfer rates at the surface of the model under the same flow conditions. They claim it could become possible to use these gauges as a catalytic probe to measure the quantity of dissociated species in the free stream or the degree of nonequilibrium in the boundary layer after a proper calibration procedure.

East *et al.* (1980) installed similar gauges on a longer flat plate submitted to the flow generated by the free-piston shock tunnel T3. The calculations they made indicate that the boundary layer has reached steady state and under most of their conditions is frozen. They conclude that no recombination reactions are taking place at the wall. Like Vidal and Golian (1967), they are unable to determine the degree of nonequilibrium in the boundary layer at high specific enthalpy. The solution to this problem relies on the exact knowledge of the

degree of cataliticity of the wall material. The heat transfer levels they obtained with their gauges are below their prediction for both a perfectly catalytic wall and a non-catalytic wall (see Fig. 1.2). A reason they invoke is that there are other chemical reactions (endothermic in nature) where nitric oxide is produced, which account for these lower levels. They also mention that there is an uncertainty in determining the viscosity, μ, because of possible helium contamination (helium is the driver gas of the shock tunnel). This uncertainty is especially important for runs where $h_0 > 25$ MJ/kg (for which the test time in their facility is very short). This problem could explain why the predictions they used overestimate the measured heat transfer rate distribution. They do not mention that there is also an uncertainty in determining the heat conductivity, k, because of helium contamination.

A review of the theoretical work concerning laminar boundary layers is postponed to Chapter 2 and comparison with experiments is postponed to Chapter 4.

1.2.2 Transition

Since transition is being studied in this project, an understanding of previous interpretations of the phenomenon is necessary even though the transition mechanism involved in our case has not been detected explicitly. The location of the transition region can be determined experimentally by measuring the skin friction distribution on a body. The skin friction and the heat transfer are related approximately by the Reynolds analogy and the same information can be obtained more easily by deriving the heat flux from surface temperature measurements. An example of experimental data is shown in Fig. 1.3 taken from Stetson and Rushton (1967). The data normally follow a set of two curves. The first curve corresponds to the laminar part of the boundary layer. The second curve corresponds to the turbulent part. The data 'jump' from the first to the second as x increases. The extent of the jump is called the transitional zone where the last point on the laminar curve at x_{tr} defines the beginning of transition and the first point on the turbulent curve defines the end of transition[1] (the Reynolds number corresponding to x_{tr} will be denoted Re_{tr}). The insta-

[1] Sometimes the data reach a maximum above the turbulent curve: this point is called the peak of transition.

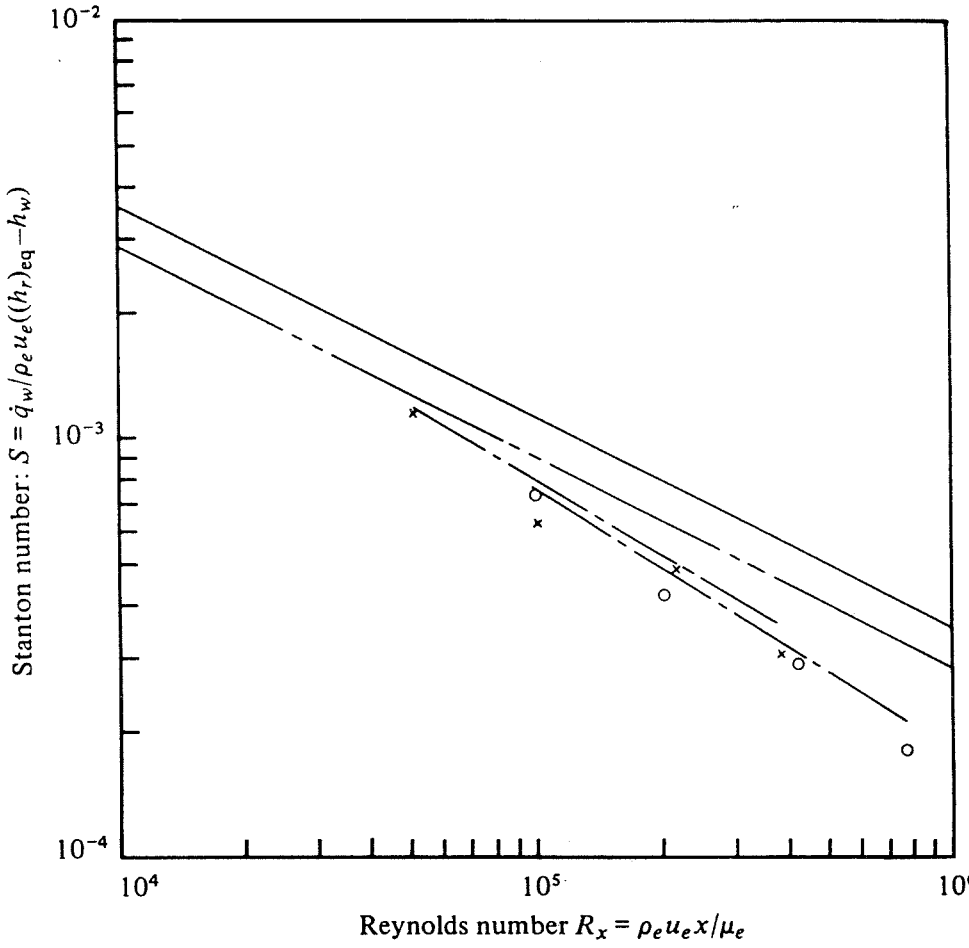

FIG. 1.2. Stanton number versus Reynolds number for a flat plate at zero-angle of incidence. ——————: theoretical prediction, fully catalytic wall. ——— – ———: theoretical prediction, non-catalytic wall. ——— – ———: theoretical prediction, non-catalytic wall plus endothermic reactions. o: experiment, h_0 = 17 MJ/kg and p_0 = 43 MPa. ×: experiment, h_0 = 16.6 MJ/kg and p_0 = 22 MPa. Taken from East *et al.* (1980).

bility process starts earlier in general at around $x = x_{tr}/2$ and this region is referred to as the 'transition onset zone' by previous investigators. An experimental study of this region is called a 'stability experiment'. A study involving only surface temperature measurement is called a 'transition experiment'. These kinds of experiments have also been made in high-enthalpy flow, for example, by Morgan and Stalker (1986) and by He and Morgan (1989). Transition experiments do not provide insight into the instability mechanism taking place in the boundary layer.

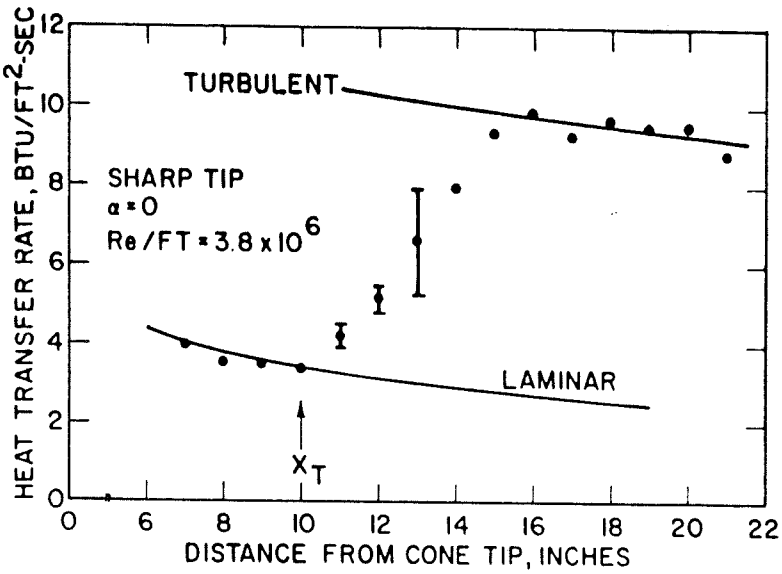

FIG. 1.3. An example of boundary-layer transition data (on an 8 deg. half-angle cone). The beginning of transition is at x_{tr} = 10 inches (254 mm) from the tip. The peak of transition (a small overshoot is sometimes present) would be at $x_{peak\ tr}$ = 16 inches (406 mm). The heat flux is displayed on a Btu/(ft^2·s) scale which should be multiplied by 0.0114 to obtain a MW/m^2 scale. This example corresponds to u_∞ = 1320 m/s, M_∞ and T_0 = 1020 K. Taken from Stetson and Rushton (1967).

It has been shown previously by Demetriades (1974) that fluctuations start well upstream of x_{tr} in the laminar boundary layer. For his stability experiments, Demetriades was able to use hot-wire anemometry to measure the magnitude of these fluctuations anywhere in the boundary layer. The frequency spectra of his time traces reveal the presence of a major mode of instability (as shown in Fig. 1.4). Its associated frequency and growth rate compare well with the theoretical predictions of the linear stability theory described below.

Throughout the last four decades, both theoretical and experimental stability analyses have been performed in the high Mach number flow regime but at low specific enthalpy. Even if the test gas behaves as a perfect one, such studies give a qualitative idea of the transition mechanism. The first kind of theoretical study is an extension of the linear stability theory to compressible flows (which sometimes today includes nonlinearity), *e.g.*, Mack (1969,1986), Stuckert and Reed (1990), Malik and Spall (1991), and Simen and Dallmann (1992). A second kind is the direct simulation method developed by Pruett and

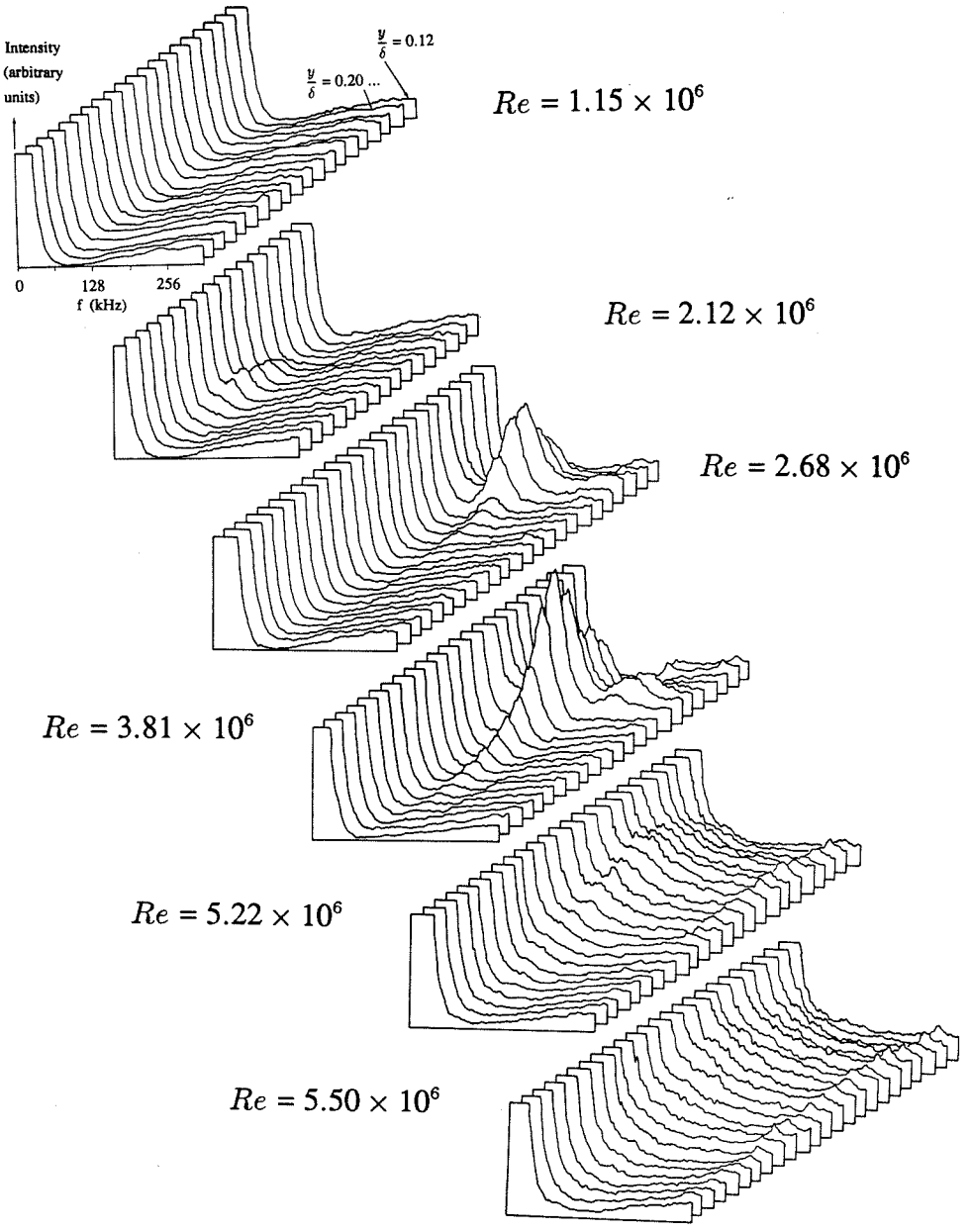

FIG. 1.4. Three-dimensional view of spectrum evolution in the boundary layer on a 5 deg. half-angle cone. The hot-wire anemometer was traversed at six locations in the x-direction and its time signal was Fourier analyzed to give its spectrum at various positions. The conditions of this experiment were $M_e = 7$ and $T_0 = 750$ K. It can be seen that there is a dominant harmonic frequency at $Re = 3.81 \times 10^6$ and at around $y/\delta = 0.68$. Taken from Demetriades (1974).

Ng (1991).

Reshotko (1976) provides a well known review of the linear stability theory. Essen-

tially, the formulation starts with adding to each flow quantity, say Q, a small perturbation component Q'.

$$Q = \overline{Q}(\underline{x}) + Q'(\underline{x}, t), \tag{1.1a}$$

where

$$Q'(\underline{x}, t) = q(y) \cdot e^{i\alpha(x\cos\psi + z\sin\psi - ct)}. \tag{1.1b}$$

ψ is the angle between the plane wave propagation direction and the x-direction (along the wall). α is the complex wave number and y is the direction normal to the wall (z is normal to x and y). c is the complex phase velocity of this plane wave. $\overline{Q}$ is the steady-state value of that flow quantity obtained from the solution of the laminar flow problem (with the proper boundary conditions). This value of Q is substituted in the continuity, momentum, and energy equations (also in the species mass conservation equations if chemical effects are taken into account). Secondly, the mean values are subtracted, and products and squares of primed quantities neglected.[2] The next step is to find the eigensolution of this system of equations, thus obtaining the values of the eigenmodes including the most amplified frequency and its spatial growth rate. Since there are several ways (because of different assumptions) to state these conservation differential equations, there will be as many basic flow solutions yielding slightly different results when the eigenvalue problem is solved.[3] This is shown, for example, in Fig. 1.5 for the case of the second mode.

The first mode is known as the Tollmien-Schlichting mode. The associated instability mechanism is viscous in nature and its growth rate decreases with Mach number. It is the only instability mode of incompressible boundary layer flows. It is sensitive to free-stream

---

[2] If the flow is incompressible and two-dimensional, it is possible to introduce a perturbation stream function ψ' such that

$$u' = \frac{\partial \psi'}{\partial y} \qquad \text{and} \qquad v' = -\frac{\partial \psi'}{\partial x}.$$

Substitution in the momentum conservation equation results in the well known Orr-Sommerfeld equation discussed by Schlichting (1979).

[3] For instance, the equations can be simplified by assuming that the streamlines are all parallel to the wall as Mack (1969) did. Recent studies have relaxed this assumption.

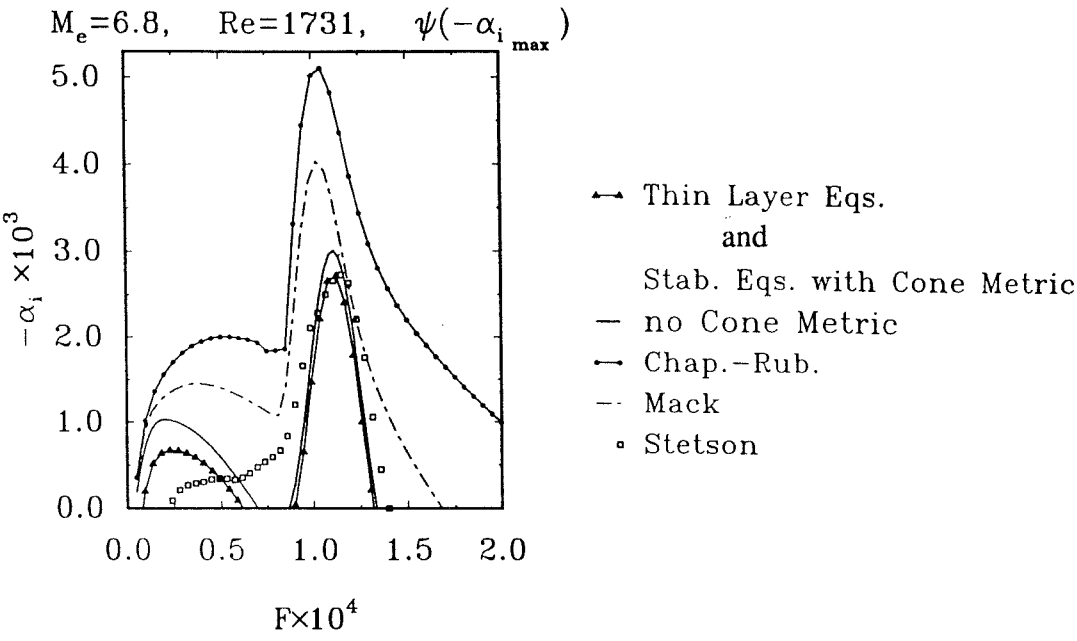

FIG. 1.5. Comparison of maximum amplification rates α_i of the second mode as a function of the dimensionless frequency F obtained from different basic-state computation methods and formulations of the stability equations. Comparison also with Stetson (1983) experimental data. Taken from Simen and Dallmann (1992).

vorticity and surface roughness. The second mode is the most strongly amplified one above Mach number 4. Its instability mechanism is inviscid in nature and appears essentially in the laminar boundary layer as periodic density and wall-parallel velocity fluctuations propagating in the flow direction. It is sensitive essentially to acoustic perturbations present in the free stream. Fig. 1.6 shows the growth rate of each of these two modes as a function of the free-stream Mach number.

There are higher order modes but they have rarely been observed experimentally (their corresponding frequencies are too high to be detected). Finally, there are the nonlinear modes about which very little is known, and which may not be predicted with certainty. They 'compete' with linear modes according to Stetson (1988) and could therefore prevent the detection of the latter. If the transition is dominated by nonlinear modes over a short distance, the process is called a 'high intensity bypass' as defined by Morkovin (1969).

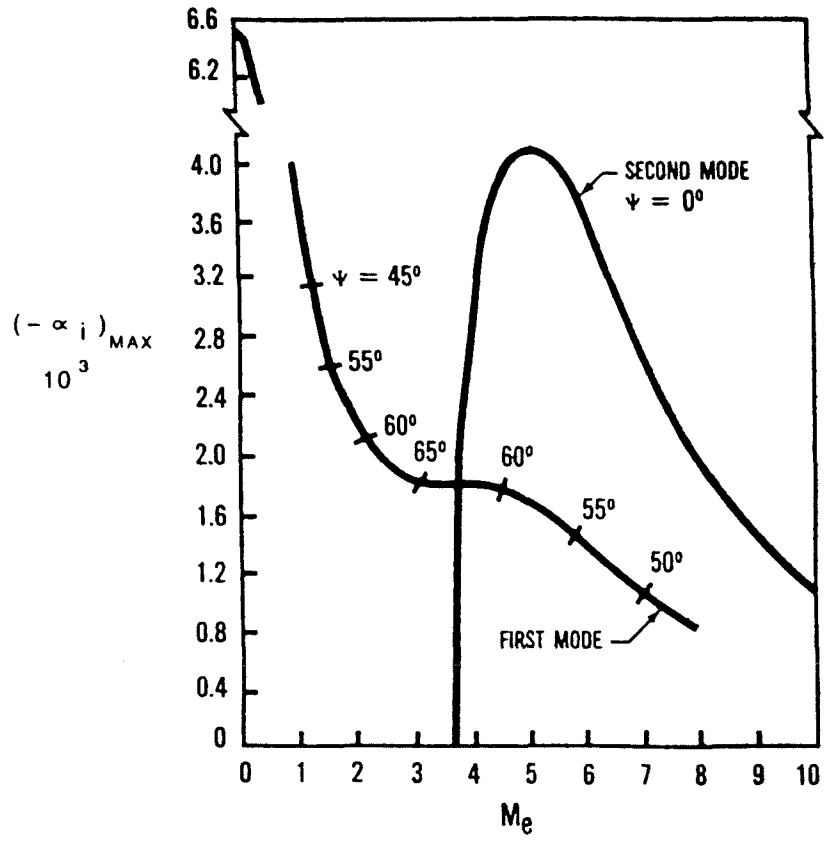

FIG. 1.6. Maximum growth rate α_i versus M_e of the first and second linear modes of instability. For the first mode, the corresponding value of ψ, the plane wave angle, decreases as M_e increases. Taken from Stetson and Kimmel (1992).

The effect of wall temperature is significant in the stability analysis at high Mach number. The first mode is stabilized by wall cooling whereas the higher order modes are destabilized. This has been found by Demetriades (1977) and by Stetson (1989) who have performed experiments in air flow over a 7 deg. half-angle cone at zero incidence either cooled or uncooled. They confirm that the transition Reynolds number is smaller when the model is highly cooled and when the second mode dominates the transition process without cooling. With a high flow velocity and with a constant wall temperature of 300 K, it is not possible to show evidence of this phenomenon as well as he did since wall cooling is always important in shock tunnel experiments.

Real-gas effects in flat-plate flows have been considered theoretically by Malik and An-

derson (1991) and by Stuckert and Reed (1990). The two groups conclude that equilibrium real-gas effects have a destabilizing influence on the growth rate of the second mode (with a slight decrease of its frequency), whereas the first mode is stabilized[4]. The effect is similar to wall cooling since the static temperature in the boundary layer is lowered as noted in the previous section on the laminar regime. No experimental investigation has addressed real-gas effects on these instability modes however.

Malik and Spall (1991) have included the effect of transverse surface curvature in their analysis. They found that it had a stabilizing influence on the axisymmetric first and second modes but had a destabilizing one on the asymmetric first mode. Furthermore, the surface divergence of a cone is found to stabilize all of them. According to Fedorov (1993), Russian researchers have found that the growth rates of these modes are lower on a cone than on a flat plate, at M_∞ = 2. They conducted an experiment in which they forced disturbances at a given frequency (typically 10, 20 or 30 kHz) at the surface of the model or in the free stream along the lines of the classic experiment of Schubauer and Skramstad (1947). Both groups used hot-wire anemometry as their diagnostic tool.

Fig. 1.7 was taken from Pate (1971) and shows a compilation of data taken from several facilities. For the same unit Reynolds number, the ratio $Re^{cone}_{peak\ tr}/Re^{planar}_{peak\ tr}$ is plotted as a function of M ($Re^{cone}_{peak\ tr}$ and $Re^{planar}_{peak\ tr}$ denote peak-of-transition Reynolds numbers). In the region of interest of this investigation, the ratio goes from 2 at M_e = 4.5 to 1.5 at M_e = 7.

This phenomenon has sometimes been referred to as the 'cone-planar anomaly'. According to Stetson and Kimmel (1992):

> "In the boundary layer of a cone at zero angle of attack the disturbance growth follows the characteristics of that predicted by classical linear stability theory. In the planar boundary layer, the dominant disturbances are low frequency disturbances which are growing in a frequency band expected to be stable. The identity of these dominant low frequency disturbances remains unsettled. The Mack (1986) and Kendall (1975) results imply that the low frequency disturbances are forced disturbances which, in some unknown way, become first mode disturbances beyond the neutral stability point."

---

[4] Stuckert and Reed (1990) also conclude that "the first mode results at low frequencies vary a great deal from the equilibrium to nonequilibrium and ideal gas models."

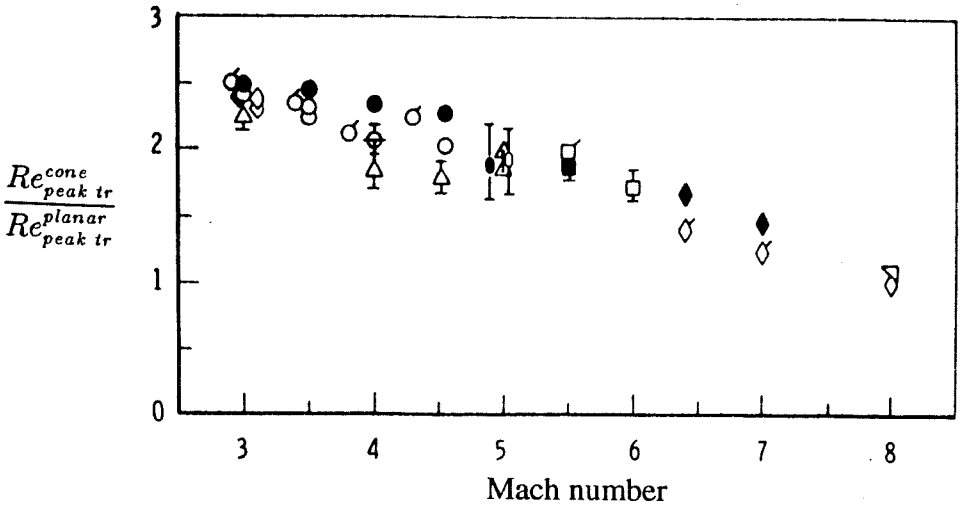

FIG. 1.7. Compilation of data obtained from different facilities where either a cone, a flat plate or a hollow cylinder were used as models in a low specific enthalpy flow ($h_0 < 1$ MJ/kg). The data are shown as the ratio $Re^{cone}_{peak\ tr}/Re^{planar}_{peak\ tr}$ versus either the M_∞ (open symbols) or M_e (solid and flagged symbols). Taken from Pate (1971).

Fig. 1.8 taken from Stetson and Kimmel (1992) shows that the second-mode frequency on a cone can be two or three times larger than inside a hollow cylinder. Hence for the same free-stream environment, the transition process is different because of the cone divergence. The planar boundary layer is not sensitive enough to the presence of high-frequency perturbations (in their wind tunnel) which actually trigger the second-mode instability on a cone.

Transition and stability experiments have been conducted by Stetson (1983), Kendall (1975), Owen (1970), Martellucci and Laganelli (1974), and Demetriades (1974) in continuous hypersonic wind tunnels. They all reported a so-called 'unit Reynolds number effect'; a compilation of data from Stetson and Potter is shown in Fig. 1.9 for example. This effect has been reported by Potter (1975) who has performed his experiments in an aeroballistic range where free-stream perturbations are presumed less severe than in a conventional wind tunnel. A dependence of a dimensionless number (Re_{tr}) on a dimensional parameter (Re/m) is not possible. The data of Fig. 1.9 therefore imply the existence of at

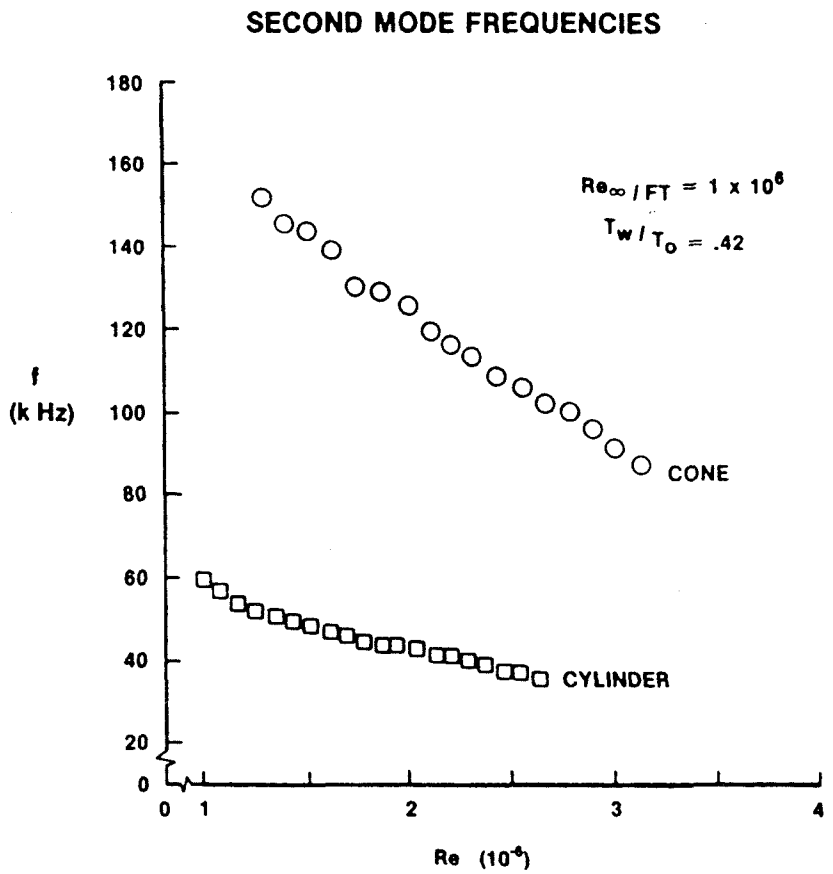

FIG. 1.8. Second mode frequencies f versus Re for a cone (circle symbols) and a hollow cylinder (square symbols). The survey was performed in a low specific enthalpy flow ($h_0 < 1$ MJ/kg) using hot-wire anemometry. Taken from Stetson and Kimmel (1992).

least one other unaccounted length scale, and the 'unit Reynolds number effect' is spurious. Beckwith (1975,1990) has been developing a 'quiet' supersonic wind tunnel and the transition Reynolds numbers that he measured are higher by a factor of 4 to 5 than those measured by other experimentalists. The 'unit Reynolds number effect' problem has finally been solved by King (1992) who observed that this effect is absent in a quiet tunnel. Potter had also reported problems with model vibrations, and these could explain his observation of this effect. He and Morgan (1989), using the free-piston shock tunnel T4, have reported a weaker dependence of Re_{tr} on Re/m but they neglected to show their data as a function of the Mach number.

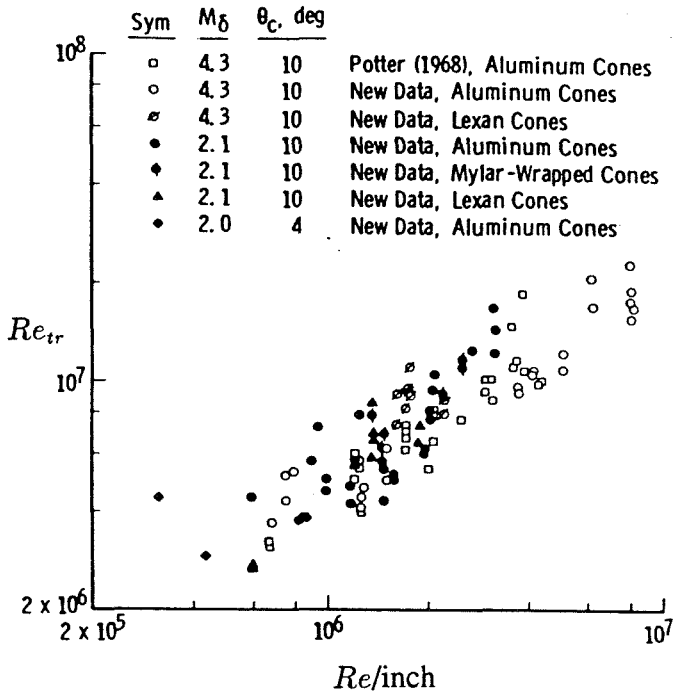

FIG. 1.9a. Re_{tr} versus unit Reynolds number Re/inch obtained in a free-flight facility. The apparent dependence is probably due to model vibrations and/or to a non-uniform wall temperature. Taken from Potter (1975). The units shown here are those used by this author.

All these clues about the various instability modes (whether they are linear or nonlinear in nature) feed several possible scenarios that describe what is happening in the transition onset zone of the laminar boundary layer. Pruett and Ng (1991) have performed a high-resolution direct numerical simulation that could be called a numerical stability experiment. They introduced in the steady-state solution (of the laminar boundary layer problem) initial perturbations consisting of axisymmetric 'second-mode' primary disturbances. They observed temporally developing subharmonic secondary instabilities not confirmed by any experiments. Maestrello *et al.* (1991) report interactions between the first and second linear modes from their direct numerical simulations. Clearly, there is not yet a consensus on the transition mechanism. There appears to be a strong dependence on the type of experimental facility used to simulate the flow, because the free-stream disturbances vary from one facility to another. Flight measurements need to be performed. It is presumed that 'second-mode' perturbations are absent in the free stream. Consequently, the second linear mode of

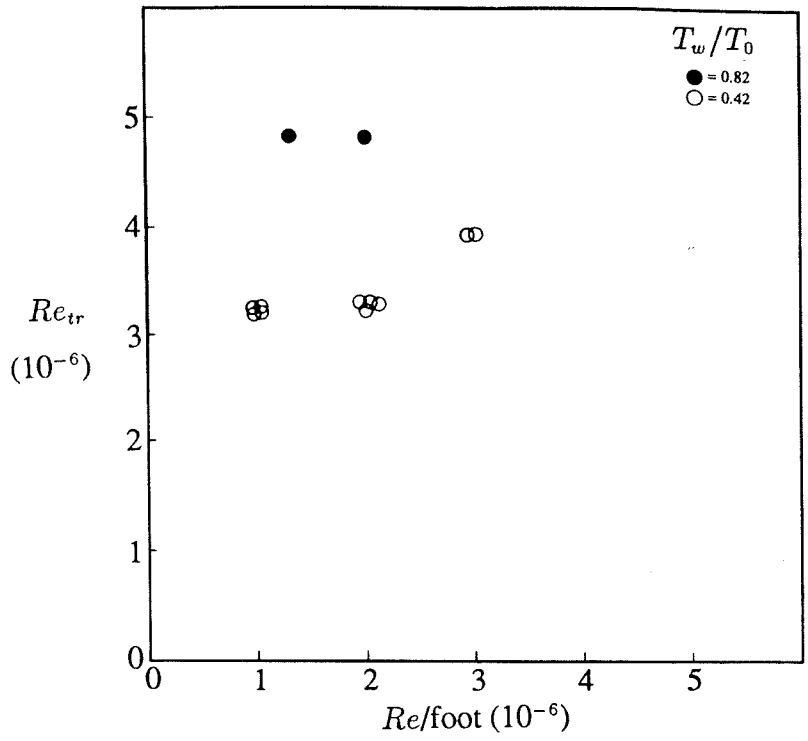

FIG. 1.9b. A few data points taken from Stetson (1986) showing also a dependence of Re_{tr} on Re/foot. Besides such an 'influence', Re_{tr} varies also according to T_w/T_0. For a given T_w/T_0 ratio, the different values of Re_{tr} are most likely due to free-stream noise specific to the continuous-flow facility used by Stetson. The units shown here are those used by this author.

instability would not dominate the transition mechanism.

1.2.3 Turbulent boundary layer

One of the problems in studying the hypersonic turbulent boundary layer was in obtaining sufficiently high Reynolds number. Although high Mach number (and sometimes high speed) was achieved in laboratory simulations, densities were never high enough and the characteristic dimension of the model (its length for example) was always short. Helium was often used as a test gas to benefit from its lower viscosity μ and its lower condensation temperature. Therefore most early studies concern the nozzle-wall boundary layer. Kemp and Owen (1972) conducted such a study with air and have shown that one of the main features of the nozzle-wall boundary layer structure is a very thick viscous sublayer (up to 40% of the boundary layer thickness). At the high Mach number of these tests (M_∞ going

from 20 to 47), it is well known that the viscous sublayer extends over a large fraction of the boundary layer thickness.

In the study of compressible turbulent shear layers, there is a well known assumption called Morkovin's hypothesis which states that the effect of density fluctuations is small if their root-mean-square value is small compared with the density mean value. This assumption holds for M_e less than five (and for free jets with $M_e < 1.5$). This means that the already known turbulence structure, *e.g.*, from the Law of the Wall, still gives good results when approximation methods are used to predict the wall heat flux (such as Van Driest's method described in the next chapter). The Morkovin hypothesis leads to the 'strong Reynolds analogy' which states that density, temperature, and velocity fluctuations are fully correlated. The experiments of Kistler (1959), Demetriades (1968), Demetriades and Laderman (1973), Johnson (1974), and Rose (1974) have confirmed this assumption with the use of hot-wire anemometry. The Mach number range $M_e > 5$ has also been investigated in the work described in the remainder of this section.

For higher Mach number at around 7, Owen and Horstman (1972) have concluded from measurements using the same diagnostic technique that the turbulent fluctutions originate close to the wall because the shear stresses there are higher. This suggestion is in agreement with incompressible flow experiments. However, for the same Mach number, Laderman (1974) has observed that rms temperature fluctuations are 20 to 30% of the mean value and dominate the turbulence, whereas velocity fluctuations are not significantly larger than in low-speed flow. At high Mach number, the temperature fluctuations are greatly reduced as the wall temperature decreases while velocity fluctuations do not change according to Laderman.

Lin and Harvey (1989) have studied the boundary layer on a 5 deg. half-angle cone at M_e = 9 in a gun tunnel with the electron beam fluorescence technique as a non-intrusive measurement tool. They conclude that a steady turbulent state is reached first at the outer edge of the boundary layer because shear stresses are higher. This observation is consistent with the calculations of Pruett and Ng (1991). This turbulent region spreads at a small an-

gle until it reaches the wall. From there, the shear stresses stay maximum and the turbulent boundary layer achieves self-similarity. Their final conclusion is that within the error margins the zero-pressure gradient boundary layer shows little fundamental difference from an incompressible one. The situation is different in other cases (such as when a shock impinges on the boundary layer).

According to Bradshaw (1977), the size of the viscous sublayer is the biggest difference between compressible and incompressible boundary layers. At $M_e = 5$, the size of a viscous sublayer thickness in compressible flow can be ten times bigger than that of an incompressible boundary layer at the same Re. No study of the structure of the turbulent boundary layer has ever been undertaken to address real-gas effects.

1.3 Research goals

The objective of this project is to find out at what Reynolds number the boundary layer becomes turbulent and then to compare it with the results obtained in previous studies. Since heat transfer measurements can be performed, another objective is to check if these measurements also relate to previous results and the existing theories , *e.g.*, the similarity theory. Ultimately, the goal of this project is to find what are the real-gas effects on transition. Real-gas effects are directly related to the presence of atomic species in the boundary layer. As the specific enthalpy, h_0, increases, the concentration of atomic species is expected to increase in the free stream due to the freezing of the gas composition in the nozzle expansion and in the boundary layer due to frictional heating. To achieve these goals, it was important to develop and build a new and inexpensive method of flow visualization capable of the high sensitivity required to show the boundary layer structure.

1.4 Thesis overview

Chapter 2 is a description and a discussion of various existing theories that predict the heat transfer rates for the laminar and turbulent regimes and therefore a more detailed extension of this chapter. Chapter 3 describes the experimental facility T5, the instrumentation and the flow visualization method mentioned above. This chapter also presents the method used for estimating the free-stream conditions. Chapters 4 through 6 are a presentation of the results. Chapter 7 addresses some potential problems such as the undesirable presence of effects due to either an angle of incidence or a small tip bluntness (a few tips were replaced as they were wearing out). The last chapter is a summary in which sample results from chapters 4 through 6 are put together to show an overall 'picture' of the heat transfer rate measurements. The observations made in this project are also then reviewed.

CHAPTER 2

Heat transfer model

This chapter is a description and a discussion of existing methods which we will use to predict heat flux levels in the laminar and turbulent regimes. The chapter covers the behavior of the test gas, whether it is pure nitrogen or air, in the limits of a frozen flow and of a flow in chemical equilibrium. A flow is frozen when there are no chemical reactions taking place anywhere: the behavior of the test gas is the same as that of a perfect gas with a constant ratio of specific heats γ. A flow is in chemical equilibrium when all possible chemical reactions (including dissociation of molecules and recombination of atoms) have infinitely large reaction rates.

2.1 The Reynolds analogy

The heat transfer rate, $\dot{q}$, is usually normalized by an expression depending on free-stream and wall conditions. This is called the Stanton number, St, which is defined as

$$St(x) = \frac{\dot{q}_w(x)}{\rho_e u_e (h_{aw} - h_w)}, \tag{2.1}$$

where h_{aw} is the adiabatic wall enthalpy and h_w is the enthalpy at the wall. This definition is used in most aerodynamic heating problems even in nonequilibrium cases. The following relation to evaluate h_{aw} is valid for this investigation as h_0 is conserved throughout the nozzle expansion and the cone shock layer. Chemical, vibrational, translational, and rotational enthalpy are all included in h_0.

$$h_{aw} = h_0 - \frac{{u_e}^2}{2}(1 - r). \tag{2.2}$$

h_0 is the total or reservoir enthalpy and r is the recovery factor. r is approximately $\sqrt{Pr}$ for a laminar boundary layer and about $r = (Pr)^{1/3}$ for a turbulent one according to Dorrance (1962). h_w is usually very small compared with h_{aw} in high enthalpy experiments and so can be neglected despite the fact that it is not known exactly. At low specific enthalpy, h_w is very close to $c_{pw}T_w$. The Reynolds number is defined as

$$Re(x) = \frac{\rho_e u_e x}{\mu_e}, \tag{2.3}$$

where x is the distance from the tip of the cone along its centerline.

An experimental set of data points can be plotted as St vs. Re. To obtain a theoretical prediction, the Reynolds analogy is used to link the heat transfer rate to the skin friction shear stress, τ_w, which is reduced to c_f by the following definition:

$$c_f = \frac{\tau_w}{\frac{1}{2}\rho_e u_e^2}. \tag{2.4}$$

The Reynolds analogy is, for gases,

$$St = \frac{c_f}{2} Pr^{-2/3}. \tag{2.5}$$

Fig. 2.1, taken from Van Driest (1959), shows the distribution of $c_f/(2St)$ vs. M_e. Clearly, for the Mach number range of interest, $c_f/2St = Pr^{2/3}$ is a good approximation where we take the Prandtl number, Pr, to be constant at $Pr = 0.7$ for air and nitrogen. This value of Pr is a reasonable choice over a wide range of temperatures according to Van Driest. It will be used for the laminar and transitional regime. As Pr is not uniform in a turbulent boundary layer along the y-direction, the Reynolds analogy has the same form, but Pr has to be redefined as an effective Prandtl number, Pr_t, and it is close to 0.86 according to Van Driest (1959). For very cold walls, the data of Cary and Bertram (1974) and Keener and Polek (1972) suggest that the Reynolds analogy should simply be, for a hypersonic boundary layer ($M_e > 5$),

$$St = \frac{c_f}{2}. \tag{2.6}$$

To obtain c_f, the compressibility transformation (see next section) is applied to c_{finc}, which is the skin friction coefficient predicted for an incompressible boundary layer at the same Reynolds number. The value of c_{finc} comes from the similarity theory in the case of a laminar boundary layer or a good correlation in the case of a turbulent one.

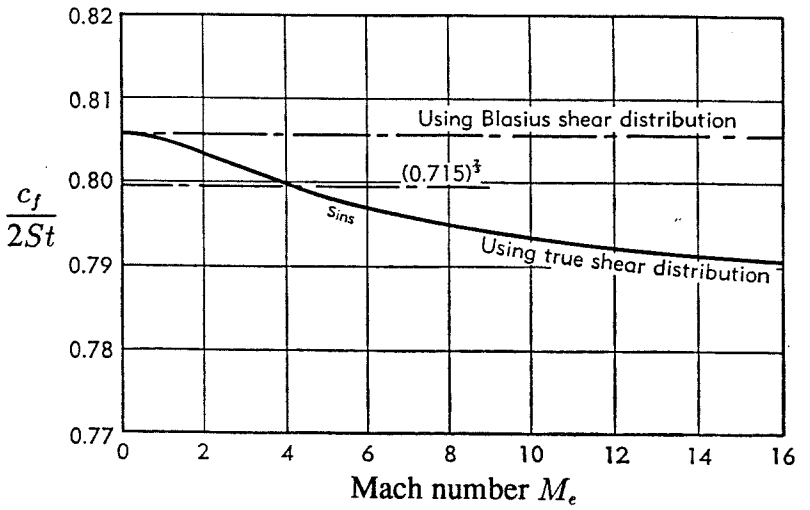

FIG. 2.1. The Reynolds analogy factor as a function of M_e for both a true shear distribution and the Blasius shear distribution. T_e = 222 K and Pr = 0.715 were used in the true shear distribution computation (the line $c_f/(2St) = 0.715$ is also plotted). Taken from Van Driest (1959).

2.2 The laminar flow regime

For a laminar boundary boundary layer, the correction factor is

$$c_f = c_{finc}\sqrt{C^*}, \tag{2.7a}$$

where

$$C^* = \frac{\rho^*\mu^*}{\rho_e\mu_e} = \left(\frac{T^*}{T_e}\right)^{1/2} \cdot \frac{T_e + S}{T^* + S}. \tag{2.7b}$$

In this case, C^* is the Chapman-Rubesin parameter and the viscosity ratio has been eliminated by using Sutherland's law. For air, and by extension for nitrogen, S = 111 K. T^* is a reference temperature obtained from

$$\frac{T^*}{T_e} = 0.5 + 0.039M_e^2 + 0.5\frac{T_w}{T_e}. \tag{2.8}$$

The above expression is taken from the reference-temperature concept introduced by Eckert (1955)[1]. From the similarity theory (Liepmann and Roshko, 1957, for example),

$$c_{finc}(Re) = \frac{0.664}{\sqrt{Re}}. \tag{2.9}$$

[1] The expression introduced by Eckert is an empirical relation. Other authors have found similar expressions

2.3 The turbulent flow regime

From a correlation mentioned by White (1974),

$$c_{finc}(Re) = \frac{0.455}{ln^2(0.06Re)}. \tag{2.10}$$

The compressibility correction factor is calculated following Van Driest (1956). According to White (1974), the following method, although developed for an adiabatic flat-plate flow, is the best over a wide range of conditions including cases with heat transfer. White (1974) computed a 14% rms error[2] of this method when compared to 230 experimental data points (with heat transfer present). The correction factor takes the form

$$c_f = \frac{1}{F_c} c_{finc}(ReF_{Re}), \tag{2.11a}$$

where

$$F_c = \frac{\frac{T_{aw}}{T_e} - 1}{\text{asin}(A) + \text{asin}(B)} \qquad \text{and} \qquad F_{Re} = \frac{\mu_e}{\mu_w}\frac{1}{F_c}. \tag{2.11b}$$

As the free-stream dissociation level is generally zero at conditions corresponding to the turbulent regime ($T_w \approx T_e$), we assume that $h_{aw}/h_e = T_{aw}/T_e$ and that $M_e = \sqrt{\gamma RT_e}$. The adiabatic wall temperature T_{aw} is evaluated from the definition

$$\frac{T_{aw}}{T_e} = 1 + r\frac{\gamma - 1}{2}M_e^2. \tag{2.12}$$

---

with slightly different coefficients. Eq. 2.8 is presented in the usual way. It can be written as

$$\frac{T^*}{T_e} = \frac{T_w + T_e}{2} + 0.039M_e^2,$$

where the first term on the right side of the equality is the mean temperature. According to Dorrance (1962), a theoretical approximation is

$$\frac{T^*}{T_e} = 0.5 + \frac{\gamma - 1}{2}\frac{\sqrt{Pr}}{6}M_e^2 + 0.5\frac{T_w}{T_e}.$$

This relation is valid for any perfect gas.

[2] White defined this rms error as

$$\text{Rms error} = \sqrt{\frac{1}{230}\sum e_i^2},$$

where e_i is the difference between the prediction and the experimental datum at the same Re.

The recovery factor r is approximately $Pr^{1/3}$ for a turbulent boundary layer. A, B, and F_{Re} are determined as follows:

$$A = \frac{2a^2 - b}{\sqrt{b^2 + 4a^2}} \qquad \text{and} \qquad B = \frac{b}{\sqrt{b^2 + 4a^2}}, \tag{2.13}$$

$$a = \sqrt{\frac{\gamma - 1}{2} M_e^2 \frac{T_e}{T_w}} \qquad \text{and} \qquad b = \frac{T_{aw}}{T_w} - 1, \tag{2.14}$$

$$F_{Re} = \frac{\mu_e}{\mu_w} \cdot \frac{1}{F_c} = \left(\frac{T_e}{T_w}\right)^{3/2} \cdot \frac{T_e + S}{T_e + S} \cdot \frac{1}{F_c}. \tag{2.15}$$

The last relation comes from Sutherland's law.

2.4 Conical flow correction factor

A second correction factor is applied to c_f to account for the axisymmetrical geometry of the flowfield. Mangler (1948) showed that the conservation equations can be transformed from axisymmetric to planar flow. This leads to c_f being multiplied by $\sqrt{3}$ in the case of a laminar flow. For the turbulent flow case, the transformation, also a multiplication factor, is determined by an approximate cone rule: Van Driest (1952) recommends a value varying between 1.087 and 1.176.

2.5 Flow in chemical equilibrium

This section is divided into two parts. The first part describes how a correction factor is obtained to account for flow in chemical equilibrium. As this factor depends on the maximum static enthalpy inside the boundary layer, the second part is a description of the method used to derive its value.

2.5.1 Chemical equilibrium correction factor

As the gas molecules are brought to rest on the skin of the cone, the excess of their flow kinetic energy is dissipated in the form of frictional heat therefore raising the local temperature. Dissociation and recombination reactions become active and the heat load on the model is different. If one considers that these chemical reaction rates are infinitely large, a correction factor can be applied to the Stanton number, St. The idea for the following derivation was taken from Park (1990). The total heat flux to the wall can be defined as

$$\dot{q}_{w\,total} = \dot{q}_r + \dot{q}_c = \dot{q}_c + \frac{\dot{q}_r}{\dot{q}_c}\dot{q}_c. \tag{2.16}$$

$\dot{q}_c$ is the conductive heat flux and $\dot{q}_r$ is the flux of chemical energy by species diffusion ($\dot{q}_r$ is also called surface recombination heat transfer rate). For a steady two-dimensional flow of an ideal dissociating gas over a flat plate, with no pressure gradient, the conservation equations reduce approximately to (see, *e.g.*, Anderson, 1989, or Dorrance, 1962):

$$\frac{\partial(\rho u)}{\partial x} + \frac{\partial(\rho v)}{\partial y} = 0 \qquad \text{(continuity)}, \tag{2.17}$$

$$\rho u\frac{\partial u}{\partial x} + \rho v\frac{\partial u}{\partial y} = \frac{\partial}{\partial y}\left(\mu\frac{\partial u}{\partial y}\right) \qquad \text{(momentum), and} \tag{2.18}$$

$$\rho u\frac{\partial h}{\partial x} + \rho v\frac{\partial h}{\partial y} = \frac{\partial}{\partial y}\left(k\frac{\partial u}{\partial y}\right) + \mu\left(\frac{\partial u}{\partial y}\right)^2 \qquad \text{(energy)}. \tag{2.19}$$

From Vincenti and Kruger (1967) and Park (1990), the atom mass conservation equation for ideal dissociating gas model (Lighthill, 1957) reduces to

$$\rho u\frac{\partial \alpha}{\partial x} + \rho v\frac{\partial \alpha}{\partial y} = \frac{\partial}{\partial y}\left(\rho\mathcal{D}\frac{\partial \alpha}{\partial y}\right) + \mathcal{K}\rho^2 e^{\left(-\frac{\theta_d}{T}\right)}(\alpha_{equil} - \alpha). \tag{2.20}$$

The left-hand side terms are the convective terms. The first right-hand side term is the diffusion term, where $\mathcal{D}$ is the diffusion coefficient of the atomic species. The second term is the source or production term where

$$\mathcal{K} = k_r\frac{\rho_d}{m^2}\frac{\alpha_{equil} + \alpha - \alpha\alpha_{equil}}{\alpha_{equil}^2}. \tag{2.21}$$

α_{equil} is the local equilibrium atom mass fraction. ρ_d and m are, respectively, the characteristic density for dissociation and the atomic weight of the species. k_r is the recombination reaction rate. θ_d is the characteristic temperature for dissociation (113,200 K for nitrogen and 59,500 K for oxygen, according to Vincenti and Kruger, 1967). From Vincenti and Kruger (1967), the atomic mass fraction, α_{equil}, and the temperature of a binary mixture of species (of molecules and atoms), such as pure nitrogen, are related by the following way:

$$\frac{\alpha_{equil}^2}{1-\alpha_{equil}} = \frac{\rho_d}{\rho} e^{\left(-\frac{\theta_d}{T}\right)}. \tag{2.22}$$

At the outer edge near the free stream, thermodynamic and flow properties are given the subcript e. At the point where the static temperature reaches a maximum (which will be higher than anywhere else because of frictional heating), thermodynamic and flow properties have the subcript m. As y decreases past this point, the temperature drops rapidly and becomes relatively low (at around 300 K) with respect to the maximum temperature, T_m, and the production term of the mass conservation equation becomes negligible with respect to the other ones at such a temperature. Because this term is neglected, the flow is considered frozen. The heat is therefore carried to the wall through conduction and through diffusion of the atomic species. We are mainly interested in this region since we can only measure the heat transfer to the wall. We introduce the compressibility transformation to obtain a self-similar solution for this region (it is assumed that $(\rho\mu)/(\rho_m\mu_m)$ is a constant).

$$\xi = \rho_m \mu_m u_m x. \tag{2.23}$$

$$\eta = \frac{u_m}{\sqrt{2\xi}} \int_0^y \rho \mathrm{d}y. \tag{2.24}$$

Now, we define

$$f' \equiv \frac{\partial f}{\partial \eta} = \frac{u}{u_m} \qquad \text{and} \qquad g \equiv \frac{h}{h_m}. \tag{2.25}$$

The computation of h_m is shown in the next section. After substitution, the conservation equations reduce to (assuming f and g are independent of ξ)

$$\left(\frac{\rho\mu}{\rho_m\mu_m} f''\right)' + f f'' = 0, \tag{2.26}$$

$$\left(\frac{1}{Pr}\frac{\rho\mu}{\rho_m\mu_m}g'\right)' + fg' + \frac{\rho\mu}{\rho_m\mu_m}\frac{u_m^2}{h_m}(f'')^2 = 0, \tag{2.27}$$

$$\left(\frac{1}{Sc}\frac{\rho\mu}{\rho_m\mu_m}\alpha'\right)' + f\alpha' = 0. \tag{2.28}$$

$$Pr \equiv \frac{\mu c_p}{k} \qquad \text{and} \qquad Sc \equiv \frac{\mu}{\rho\mathcal{D}}. \tag{2.29}$$

The problem can be simplified such that we do not need to find f and g explicitly. We want an approximate expression for α_w and g_w valid close to the wall. If we integrate these differential equations from $\eta = 0$ to η_m, where η_m is the location where α and h are maximum, the boundary conditions are

$$f(0) = 0, \qquad f'(0) = 0, \qquad f'(\eta_m) = 1.0, \tag{2.30}$$

$$g(0) = g_w, \qquad g(\eta_m) = 1.0, \tag{2.31}$$

$$\alpha(0) = \alpha_w \qquad \text{amd} \qquad \alpha(\eta_m) = \alpha_m. \tag{2.32}$$

It will be shown in the next section that h_m is of order h_0 (which is very high, of order 20 MJ/kg) and that u_m is of order $0.6u_e$. The strong assumption is made that the third term of Eq. 2.27 becomes negligible compared to the other terms (f'' and $(\rho\mu)/(\rho_m\mu_m)$ are of order g'' and 1, respectively). The solution to Eq. 2.28 can be found in textbooks on ordinary differential equations. For simplicity, we define

$$G(\varsigma, \sigma) = \int_0^\sigma e^{\left(-\int_0^\eta \varsigma \frac{\rho_m\mu_m}{\rho\mu} f\, d\eta\right)} d\eta, \tag{2.33}$$

where ς and σ are dummy variables. Assuming that f is known, it can be shown that the solution to the mass conservation equation is

$$\alpha = \frac{(\alpha_m - \alpha_w)G(Sc, \eta)}{G(Sc, \eta_m)}. \tag{2.34}$$

From this expression, it can be shown that

$$\left.\frac{\partial\alpha}{\partial\eta}\right|_w = \frac{(\alpha_m - \alpha_w)}{G(Sc, \eta_m)}. \tag{2.35}$$

The rate at which atoms are diffusing close to the wall is equal to the rate at which they recombine. Therefore,

$$\rho\mathcal{D}\left.\frac{\partial\alpha}{\partial y}\right|_w = \frac{1}{Sc}\sqrt{\frac{u_m}{2\rho_m\mu_m x}}\rho_w\mu_w\left.\frac{\partial\alpha}{\partial\eta}\right|_w = \phi_w\rho_w\alpha_w. \tag{2.36}$$

ϕ_w is a variable for the rate at which atoms are recombining (with the dimension of velocity) at the wall. Therefore, combining Eq. 2.35 and Eq. 2.36, we obtain

$$\alpha_w = \frac{\alpha_m}{1 + Sc\,G(Sc,\eta_m)\frac{\mu_m}{\mu_w}\frac{\phi_w}{u_m}\sqrt{2\rho_m u_m x/\mu_m}}. \tag{2.37}$$

$\dot{q}_r = \phi_w \rho_w \alpha_w D$, where D is the dissociation energy per unit mass[3]. Hence,

$$\dot{q}_r = \frac{1}{Sc\,G(Sc,\eta_m)} \frac{\alpha_m D \rho_w \mu_w \sqrt{u_m/2\rho_m\mu_m x}}{1 + \frac{1}{Sc\,G(Sc,\eta_m)}\frac{\mu_w}{\mu_m}\frac{u_m}{\phi_w}\sqrt{\mu_m/\rho_m u_m x}}. \tag{2.38}$$

The conduction heat tranfer rate is

$$\dot{q}_c = k\left.\frac{\partial T}{\partial y}\right|_w = \frac{\mu_w}{Pr}\left.\frac{\partial g}{\partial \eta}\right|_w \rho_w h_m \sqrt{\frac{u_m}{2\rho_m\mu_m x}}. \tag{2.39}$$

The solution to the energy conservation Eq. 2.27 (without the third term) is

$$\left.\frac{\partial g}{\partial \eta}\right|_w = \frac{1 - g_w}{G(Pr,\eta_m)} = \frac{1}{G(Sc,\eta_m)}. \tag{2.40}$$

The last equality is derived as follows: It is generally assumed that the Prandtl number, Pr, is equal to the Schmidt number, Sc, for gases , *i.e.*, the diffusion rate of heat is the same as the diffusion rate of the species[4]. $g_w << 1$ means that the wall enthalpy is small compared to the static enthalpy at the maximum-temperature point which is the case for a high-enthalpy boundary layer in chemical equilibrium.

$$\frac{\dot{q}_r}{\dot{q}_c} = \frac{\alpha_m D}{h_m} \frac{1}{1 + \frac{1}{Sc\,G(Sc,\eta_m)}\frac{\mu_w}{\mu_m}\frac{u_m}{\phi_w}\sqrt{u_m/2\rho_m\mu_m x}}. \tag{2.41}$$

Chemical equilibrium means that all reactions are infinitely fast. Therefore,

$$\frac{\phi_w}{u_m}\sqrt{\frac{2\rho_m u_m x}{\mu_m}} >> 1. \tag{2.42}$$

Since Sc and $G(Sc,\eta_m)$ are of order 1, this implies that

$$\frac{\dot{q}_r}{\dot{q}_c} \approx \frac{\alpha_m D}{h_m}. \tag{2.43}$$

The heat flow prediction for an equilibrium gas flow is the one predicted for a frozen flow multiplied by $1+\frac{\alpha_m D}{h_m}$ which only depends on the conditions at the point where h is maximum (and denoted h_m).

---

[3] The values of D are 33.5 MJ/kg and 15.5 MJ/kg for nitrogen and oxygen, respectively, according to Vincenti and Kruger (1967).

[4] This means that the Lewis number $Le\ (\equiv Pr/Sc) = 1$.

2.5.2 Flow conditions at the maximum-temperature point

The next step is to compute the flow properties at the point where the static temperature is maximum. We need an expression for α_m and h_m. We seek first an expression $h = h(u)$ along the line of the derivation of the familiar Crocco-Busemann integral to the energy equation.

$$\frac{\partial h}{\partial x} = \frac{\partial h}{\partial u}\frac{\partial u}{\partial x} \qquad \text{and} \qquad \frac{\partial h}{\partial y} = \frac{\partial h}{\partial u}\frac{\partial u}{\partial y}, \tag{2.44}$$

$$\mathrm{d}h = c_p \mathrm{d}T \qquad \text{for any gas, so} \tag{2.45}$$

$$\frac{\partial h}{\partial u} = c_p \frac{\partial T}{\partial u} \qquad \text{or} \qquad \frac{\partial T}{\partial u} = \frac{1}{c_p}\frac{\partial h}{\partial u}. \tag{2.46}$$

Including the viscous dissipation term, the energy equation becomes

$$\frac{\partial h}{\partial u}\left(\rho u \frac{\partial u}{\partial x} + \rho v \frac{\partial u}{\partial y}\right) = \frac{1}{c_p}\frac{\partial h}{\partial u}\frac{\partial}{\partial y}\left(k\frac{\partial u}{\partial y}\right) + \frac{1}{c_p}\frac{\partial^2 h}{\partial u^2}k\left(\frac{\partial u}{\partial y}\right)^2. \tag{2.47}$$

Substituting the momentum conservation equation,

$$\frac{\partial h}{\partial u}\frac{\partial}{\partial y}\left(\mu\frac{\partial u}{\partial y}\right) = \frac{1}{c_p}\frac{\partial h}{\partial u}\frac{\partial}{\partial y}\left(k\frac{\partial u}{\partial y}\right) + \frac{1}{c_p}\frac{\partial^2 h}{\partial u^2}k\left(\frac{\partial u}{\partial y}\right)^2. \tag{2.48}$$

Rearranging the terms and knowing that $Pr \equiv (\mu c_p/k)$,

$$\left(\frac{Pr-1}{Pr}\right)\frac{\partial h}{\partial u}\frac{\partial}{\partial y}\left(\mu\frac{\partial u}{\partial y}\right) = \left(\frac{\partial^2 h}{\partial u^2}\frac{k}{c_p} + \mu\right)\left(\frac{\partial u}{\partial y}\right)^2. \tag{2.49}$$

At T5 conditions, the ratio of the left-hand side term of the above equation and the right-hand side term is of order 10^{-3} across the boundary layer. Neglecting the former, Eq. 2.49 becomes

$$\frac{\partial^2 h}{\partial u^2} = -\frac{1}{Pr}. \tag{2.50}$$

Having at the wall $h = h_w$ and $\alpha_w = 0$ and at the outer edge of the boundary layer $h = h_e$ and $\alpha = \alpha_e$, the solution[5] to this equation is

$$\frac{h}{h_e} = \frac{h_w}{h_e} + \left(1 - \frac{h_w}{h_e}\right)\frac{u}{u_e} + \frac{u_e^2}{2Prh_e}\left(1 - \frac{u}{u_e}\right)\frac{u}{u_e} \tag{2.52}$$

---

[5] If there is no dissociation , *i.e.*, $\alpha \equiv 0$ and if the gas is a perfect gas , *i.e.*, $M_e^2 = u_e^2/(\gamma RT)$ with $Pr = 1$, we obtain the Crocco-Busemann relation:

$$\frac{T}{T_e} = \frac{T_w}{T_e} + \left(1 - \frac{T_w}{T_e}\right)\frac{u}{u_e} + \frac{\gamma-1}{2}M_e^2\frac{u}{u_e}\left(1 - \frac{u}{u_e}\right). \tag{2.51}$$

where

$$h_e = h_0 - \frac{u_e^2}{2} \qquad \text{and} \qquad h_w \approx c_{pw} T_w . \tag{2.53}$$

To find u_m and therefore h_m by substitution, we set

$$\left.\frac{\partial(h/h_e)}{\partial(u/u_e)}\right|_m = 0 = \left(1 - \frac{h_w}{h_e}\right) + \frac{u_e^2}{2Prh_e}\left(1 - 2\frac{u}{u_e}\right). \tag{2.54}$$

Hence,

$$\frac{u_m}{u_e} = \frac{1}{2} + \left(1 - \frac{h_w}{h_e}\right)\frac{Prh_e}{u_e^2}. \tag{2.55}$$

Now that we have the value of h_m, we need to extract the value of α_m. We can either use the ideal dissociating gas model or a program that could perform this computation. The problem is especially easy when the gas is in chemical equilibrium as has been assumed here.

Since the static pressure is assumed constant everywhere in the boundary layer,

$$p = p_w = p_e = \frac{k_B}{2m}\rho T\,(1+\alpha) \qquad \text{or} \qquad \rho T = \frac{2mp_e}{k_B\,(1+\alpha)}. \tag{2.56}$$

Substituting in Eq. 2.22, we obtain

$$\alpha_m = \sqrt{\frac{N(T_m)}{1+N(T_m)}} \qquad \text{where} \qquad N(T_m) = \frac{\rho_d k}{2mp_e} T_m e^{\left(-\frac{\theta_d}{T_m}\right)}. \tag{2.57}$$

From Lighthill's ideal dissociating gas model (IDG), we can deduce T_m by solving the algebraic system of equations consisting of the previous relation and the relevant caloric equation of state:

$$h_m = \frac{k_B}{2m}\left((4+\alpha_m)\,T_m + \alpha_m\theta_d\right). \tag{2.58}$$

For an air mixture, the IDG relations between T and α are no longer valid. Instead, we perform an equilibrium calculation[6] to obtain the gas composition at pressure p_e and temperature T_m. From the equilibrium composition of air obtained, we deduce an effective value for α_m, $\alpha_m\theta_d$ and $\alpha_m D$ by a weighted average based on the mass fractions of the species.

---

[6] We used for this purpose a computer program called STANJAN written by Reynolds (1981).

Table 1 presents the results of these calculations for selected cases. Table 2 presented in Chapter 3 completes this table. As discussed in Chapter 3, the free stream is assumed frozen, *i.e.*, $\alpha_e = \alpha_\infty$ (at the chosen conditions, dissociation across the shock in front of a 5 deg. half-angle cone is negligible). The effect of α_e cannot be neglected as seen in Table 1. If the value of α_e were zero, the value of α_m based on the calculation method outlined in this section would not be different than the ones shown in Table 1 for the same values of h_0 and u_e. It is probable that the actual value of α_m is different than the calculated value because of atomic species already present in the free stream (due to the freezing of the gas composition at the exit plane of the nozzle). We will presume that the real-gas effects observed in this project are qualitatively the same as when $\alpha_e = 0$ (the presence of atomic species in this case would only be due to frictional heating in the boundary layer). For simplicity, we define L, $T1$ and $T2$ where, depending on the regime of the boundary layer,

$$St = \frac{L}{Pr^{2/3} Re^{1/2}} \quad \text{and} \quad St = \frac{T1}{ln^2(T2\, Re)}. \tag{2.59}$$

run #	T^*, K	T_m, K	C^*,	L,	$T1$,	$T2$,	α_e,	α_m,	h_m MJ/kg	h_0 MJ/kg
Nitrogen:										
349	820	1000	0.74	0.494	0.119	0.027	0.00	0.000	1.04	3.52
544	2636	3845	0.75	0.498	0.178	0.086	0.00	0.002	4.49	11.60
536	3158	4434	0.78	0.507	0.198	0.109	0.01	0.073	5.48	14.00
140	4831	5488	0.87	0.536	0.263	0.204	0.05	0.073	9.20	22.20
Air:										
336	794	1000	0.74	0.494	0.119	0.027	0.00	0.000	1.04	3.41
545	2455	3024	0.79	0.510	0.196	0.096	0.00	0.072	4.57	11.30
537	3112	3391	0.82	0.521	0.222	0.129	0.04	0.110	5.68	14.00
157	3789	3930	0.85	0.530	0.244	0.163	0.10	0.189	7.65	18.50

Table 1. Results of calculations performed using the model presented in this chapter.

2.6 Chapter summary

In this chapter, we have reviewed the predictions for the heat transfer rate distribution on the surface of a slender cone. We addressed the behavior of the gas in the limits of a frozen flow and of a flow in chemical equilibrium. To obtain these predictions, we start by evaluating the skin friction distribution from an incompressible analysis. Then it is converted into a heat transfer rate distribution via the Reynolds analogy. Various corrections are made to account for the conical geometry, compressibility, and real-gas effects. Before this analysis can be undertaken, it is important to evaluate the free-stream parameters. The calculation method is presented in the next chapter, along with descriptions of the T5 experimental facility, the model, and the instrumentation.

CHAPTER 3

Experimental facility and instrumentation

This chapter is a description of the shock tunnel facility used to generate high-enthalpy flows, the instrumentation which includes thermocouples mounted flush with the surface of the model, and the flow visualization apparatus. The method to evaluate the free-stream parameters is also presented.

3.1 Description and operation of the T5 facility

The facility used for the experimental work was T5, an 'impulse' facility called a free-piston shock tunnel or 'Stalker tube'. The tube is separated into two parts by a diaphragm (typically a 7 mm thick stainless steel plate). On one side of this diaphragm is the test gas (or driven gas) and on the other side the driver gas. When the pressure difference is high enough, the diaphragm bursts and a shock wave propagates into the driven section. The flow behind the shock is brought to rest by the reflection of the shock at the dowstream end of the shock tube, where the stagnant hot gas is expanded and accelerated through a nozzle. The nozzle is isolated initially from the test gas in the shock tube by a thin membrane; the nozzle, the test section, and the dump tank are initially evacuated.

The stagnation conditions (the 'reservoir'), after compression from the reflected shock wave, are typically a temperature of 9,000 K and a pressure of up to 100 MPa. This produces very high heat loads, which no known materials can sustain without melting for more than a few milliseconds.

To achieve these conditions, it is necessary to have a strong shock in the shock tube. It has been shown that, given constraints on pressure, this can be achieved if the speed of sound is high in the driver gas at the time the diaphragm bursts. For this reason, a light gas, helium or a mixture of helium and argon, is chosen for the driver gas. Also, the speed of sound increases with temperature. One of the best ways to efficiently generate high temperature for a short time (so as to not melt the surface of the inner walls) is to compress this light gas with a free piston. For a given compression ratio, the best gain in temperature and pressure is achieved with a monatomic gas.

Compressed air typically stored at 8 MPa (as in run # 534) in a reservoir is used to push the piston. At one point during the travel in the compression tube, the pressure in front of the piston (initially at 120 kPa) becomes higher than behind and the piston starts to decelerate. When the diaphragm bursts later, the driver gas pressure and the temperature are around 90 MPa and 4,000 K, respectively. The shock propagates in the shock tube at 3.2 km/s and reflects from the end wall, creating a reservoir zone. From there the test gas expands in the nozzle to a velocity of 4.3 km/s and free-stream Mach number M_∞ = 5. The speed of this shock wave is measured by piezoelectric pressure transducers installed at locations along the length of the tube as shown in Fig. 3.1. The pressure in the stagnation region is also measured with the same type of transducer. These two values are the only ones needed to perform a chain of calculations of the flow conditions at the outer edge of the boundary layer on the model. To optimize the test time, the pressures of all the gases in the different sections of the facility prior to a shot, as well as the mixture composition of the driver gas, are tuned so the piston velocity at diaphragm rupture just matches the flow into the shock tube. Fig. 3.1 shows an example of a pressure trace recorded from a transducer located just upstream of the nozzle (this gives the reservoir pressure).

The data acquisition system (DAS) consists of amplifiers, digitizers, power supplies for the pressure tranducers, threshold detectors (used to trigger the data acquisition process), and a control circuit for the laser and the camera shutter. Fig. 3.2 is a schematic of the arrangement of these components.

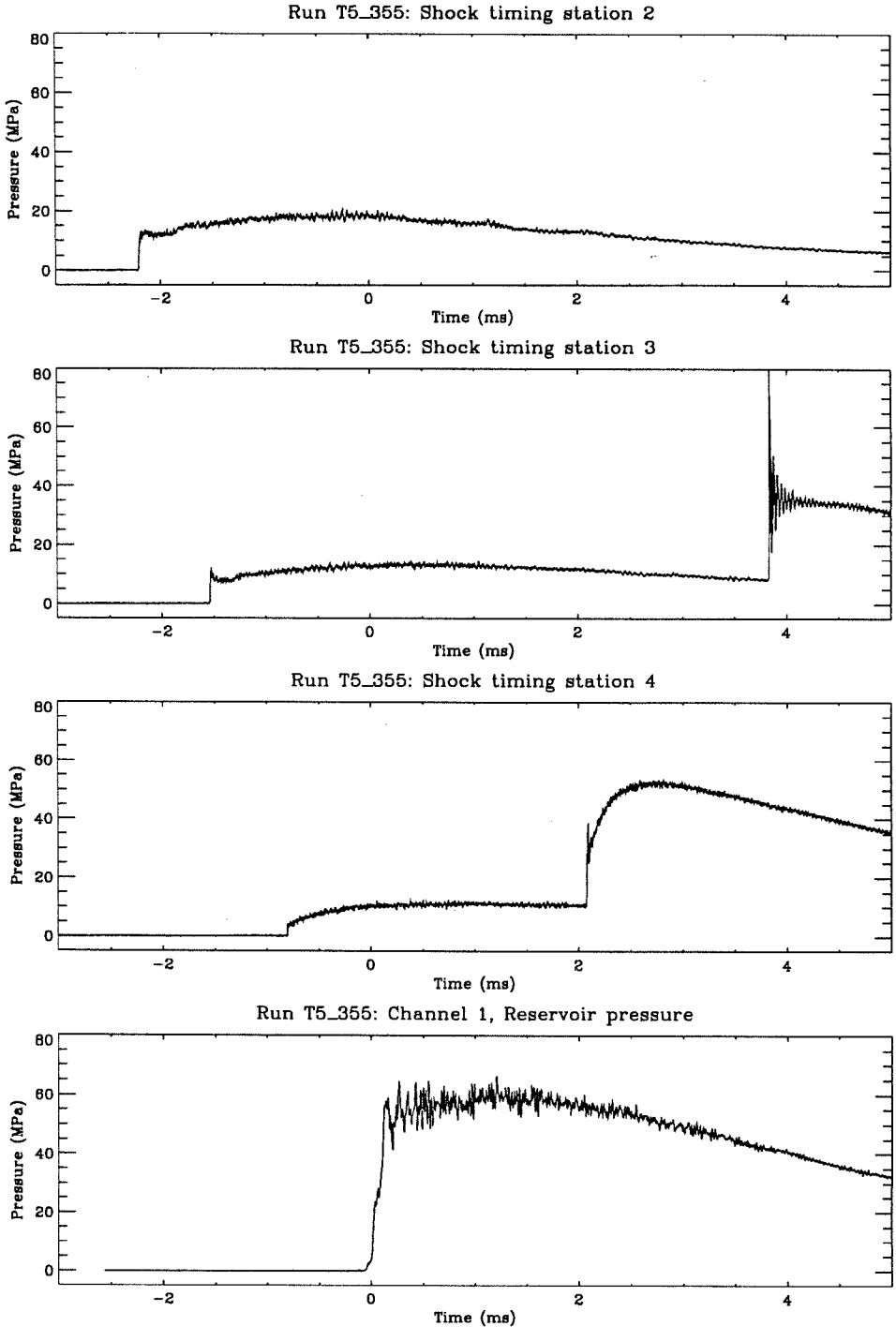

FIG. 3.1. Time traces given by four pressure transducers (during a test run) located at different stations along the shock tube. The velocity of the incident shock wave is obtained from the distance separating stations 3 and 4 divided by the time difference of the signal rises. The fourth transducer gives the value of the reservoir pressure, p_0, as the average of the time signal between t = 1.0 ms and t = 1.5 ms is made.

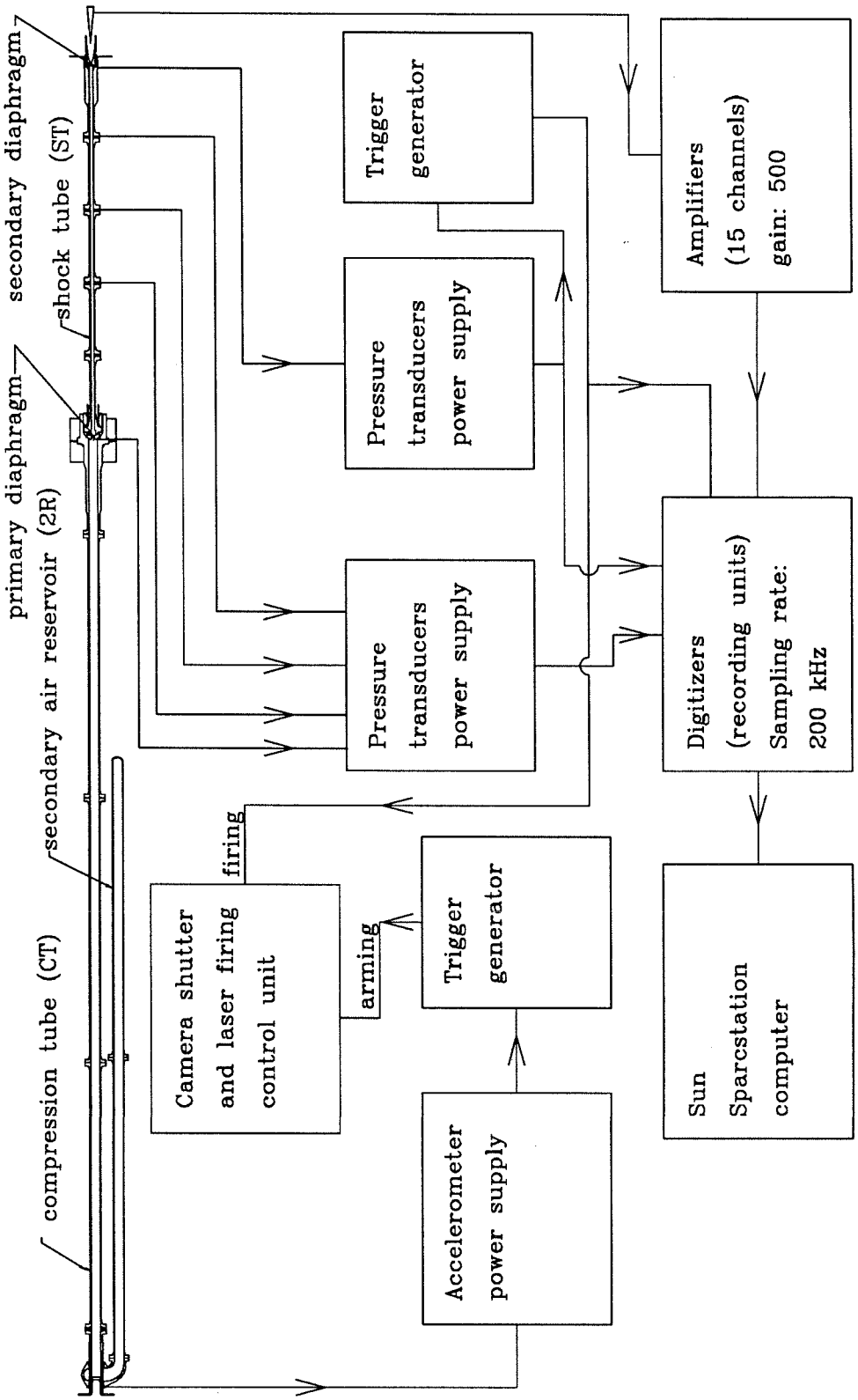

FIG. 3.2. Schematic diagram of the data acquisition system arrangement.

3.2 Free-stream conditions

Table 2 gives the reservoir and test section conditions chosen for the present investigation. The reservoir specific enthalpy is determined from the measured shock speed, the measured reservoir pressure by using a computer code written by McIntosh (1970) (called ESTC) which performs an equilibrium calculation[1]. The nozzle flow is then computed by using an axisymmetric inviscid nonequilibrium flow code developed by Rein (1989). For all the experiments, the same contoured-wall nozzle was used with an exit/throat area ratio (A/A^*) of 109.5 (exit diameter: 32 cm, throat diameter: 3.1 cm). A perfect gas flow with $\gamma = 1.4$ gives an exit Mach number M_∞ of 7.08. This method of determining free-stream conditions has been tested by measuring test section Pitot pressure distributions (Hornung, 1992) and stagnation-point heat flux (Wen and Hornung, 1993). The gas is partially dissociated at the nozzle exit (see Table 1, p. 32), especially in the case of air at high specific reservoir enthalpy where it also contains some nitric oxide. The presence of atomic species is unavoidable in high-enthalpy reflected shock tunnels unless the reservoir pressure is increased enormously (Hornung and Bélanger, 1990). The achievable repeatability of the facility, an important property when comparisons need to be made between slightly different conditions, has been demonstrated to be approximately $\pm$ 1% for the shock speed and $\pm$ 3% for the reservoir pressure (Hornung, 1992).

To compute the flow conditions at the outer edge of the boundary layer on the cone, the Taylor-Maccoll set of ordinary differential equations (Taylor and Maccoll, 1933) were solved for each of the nozzle exit conditions. For this purpose the cone flow was assumed to be frozen because the shock angle is very small[2]. The ratio of specific heats, γ, was determined by the frozen free-stream composition following Vincenti and Kruger (1967)[3].

---

[1] The formulation of the problem was reduced to one dimension and viscosity was neglected. Also, if the measured value of p_0 (supplied initially to the program) is different from the calculated value of p_0, the adjustment to the measured value is assumed to be isentropic.

[2] The nozzle axial distributions of species concentrations are essentially constant at all the reservoir conditions considered according to computations made with the SURF program.

[3] The value of this effective γ is obtained from a mass-weighted average of the specific heats and varies

run #	p_0, MPa	h_0, MJ/kg	T_0, K	u_e, km/s	ρ_e, g/m^3	T_e, K	M_e,	Re/m, (10^{-6})
Nitrogen:								
542	11	3.50	2902	2.32	44.1	307	6.5	5.45
546	16	5.83	4680	2.95	41.7	495	6.5	4.67
361	19	6.00	4807	2.99	48.2	509	6.5	5.33
*544	24	11.6	7463	4.38	24.1	1379	5.8	2.11
*349	47	3.52	2940	2.34	194.6	312	6.5	23.95
540	57	7.70	5911	3.59	78.1	734	6.5	8.16
548	55	9.68	6958	4.03	62.8	1030	6.2	5.97
534	55	10.60	6329	4.05	66.3	1400	5.4	5.31
*536	60	14.00	8369	4.76	52.9	1814	5.5	4.30
*140	60	22.20	9799	5.67	37.8	3606	4.5	2.52
563	85	13.20	8279	4.65	75.7	1630	5.6	6.37
566	85	14.20	7808	4.63	78.0	2136	4.9	5.63
Air:								
543	11	3.60	2955	2.30	46.8	313	6.5	5.67
547	16	5.61	4055	2.70	49.8	431	6.5	5.59
362	19	6.00	4244	2.76	56.5	450	6.5	6.29
*545	24	11.30	6421	4.14	27.7	1426	5.4	2.24
*336	42	3.41	2826	2.23	187.4	300	6.5	22.96
541	55	7.34	5000	3.45	87.3	700	6.5	9.02
549	52	9.08	5696	3.78	69.8	1119	5.6	5.93
553	55	12.20	6990	4.32	57.6	1749	5.1	4.34
*537	60	14.00	7626	4.59	55.8	2019	5.0	4.12
*157	60	18.5	8788	5.19	44.9	2666	4.7	3.21
343	85	12.80	7329	4.47	85.0	2208	4.9	6.35
564	85	13.00	7410	4.46	83.5	1933	5.0	6.13
CO_2:								
569	55	3.64	2994	2.00	367.4	572	5.3	28.42
573	55	5.88	3611	2.77	156.2	1492	4.4	8.76
570	55	8.32	4163	3.01	126.6	1872	4.5	7.25
He:								
550	40	58.4	11273	10.64	10.1	384	11.9	4.53
551	50	34.0	6563	8.11	21.4	223	11.9	10.39
552	55	26.3	5077	7.17	31.1	174	11.9	15.69

Table 2. Reservoir and outer edge of the boundary layer conditions.
*: run also included in Table 1, p. 32.

The boundary layer thickness was assumed to be negligible for this purpose. The results showed typically a 30 to 40% increase in density, a 1% decrease in gas velocity, and an 8 to 18% decrease in Mach number between the nozzle exit and the cone boundary layer edge.

---

between 1.40 (for $h_0 < 12$ MJ/kg) and 1.42 (for $h_0 \approx 12$ MJ/kg).

The conditions thus obtained at the wall of the cone (or the outer edge of the boundary layer) were used to form the Stanton and Reynolds numbers. The unit Reynolds numbers (Re/m) are also shown in Table 2. This table is completed by Table 1 shown in Chapter 2 for some of the conditions.

3.3 Model and instrumentation

3.3.1 Cone and longitudinal alignment procedure

A 5 deg. half-angle cone was built for this experiment. It is 1 m long and is divided into three sections as shown in Fig. 3.3 The tip section (76 mm long) is a solid piece of Waspalloy, a stainless steel that has good toughness at high temperature. Even so, the tip radius was found to increase progressively by melting from shot to shot, from an initial 0.06 mm to approximately 0.15 mm, at which value it stabilizes after typically 20 shots. This increase of nose radius was found to have no detectable effect on the heat transfer distribution, as will be shown later.

The second section (127 mm long) is a solid piece of aluminum. The third piece (790 mm long, made of aluminum) is hollow and has a wall thickness of 12 mm. It consists of two longitudinal halves held together by a dove-tail joint (see Fig. 3.4), so that they slide into each other without any need for screws, leaving the outside perfectly smooth except for an almost invisible longitudinal seam. The assembled cone is screwed onto a sting-mounted base plate made of steel (see Fig. 3.5).

To make sure that the centerline of the cone-sting assembly is parallel to the centerline of the nozzle, the following longitudinal alignment procedure was adopted. Before the installation of the sting, a 1.2 m long bar was inserted in the sting mount (see Fig. 3.6).

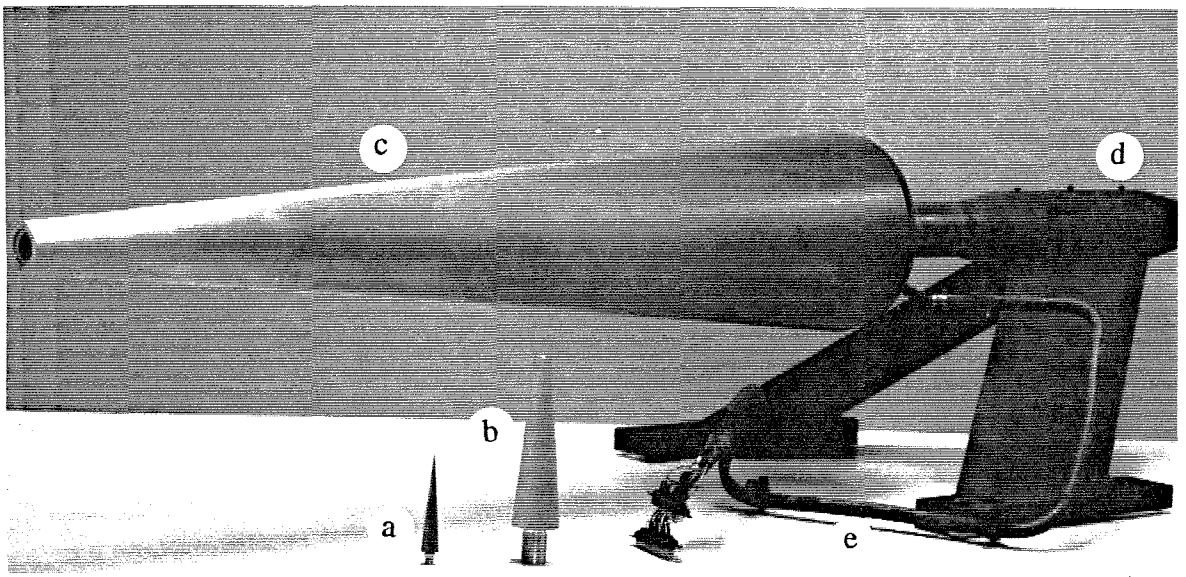

FIG. 3.3. Photograph of the model partly disassembled to show the tip (a), the second section (b) and the main body (c). The sting mount is indicated as (d) and the copper pipe protecting the fifteen thermocouple wires as (e).

This bar is made of stainless steel and its diameter and surface finish are well within acceptable tolerances. The idea is that by sliding a dial-indicator along a portion of it (30 cm), the slope of this beam can be measured. From this value we can deduce the angle of incidence (which was no more than 0.02 deg.). Fig. 3.7 shows the setup: the dial-indicator is mounted on a long rod. This rod is attached to a post clamped on the nozzle support trolley. The trolley is free to move in the same direction as the test section and the shock tube which are all mounted on the same rails. These rails were carefully aligned during the construction phase of the facility. The tolerance in their alignment is in the order of 0.25 mm per 50 m ($1/200000\ m^{-1}$).

The model is positioned in the test section such that it protrudes 330 mm into the nozzle during the test time and such that its centerline is not congruent with the nozzle centerline (the model centerline is above the nozzle centerline and the distance between them is on the order of 64 mm). This allows all the gauges on the cone to be completely inside the uniform

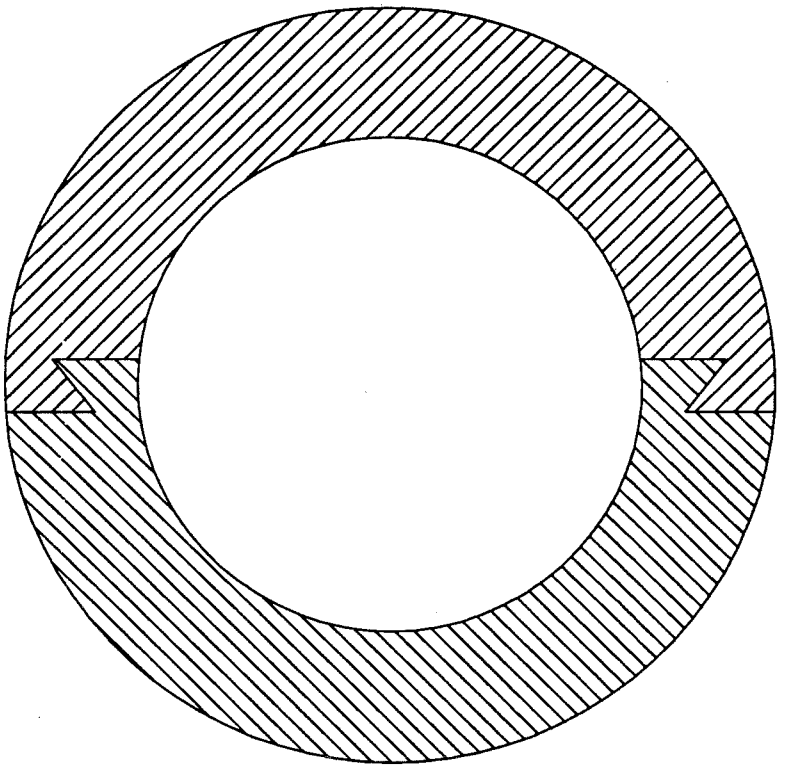

FIG. 3.4. Sketch of the model cross-section showing the assembly of the two longitudinal cone parts.

test rhombus of the nozzle flow above $M_\infty = 5.6$. In other words, the steady expansion from the lip of the nozzle, being deflected away by the cone shock wave, never impinges on the surface between two gauges. At $M_\infty < 5.6$, the last gauge (number 15) probably does not give an accurate reading as the upstream edge of the expansion fan impinges on the cone at this gauge location. This problem might affect the corresponding results of this gauge concerning the laminar regime of the boundary layer. Scale drawings are shown in Fig. 3.8 corresponding to different test conditions. The position of upstream edge of the expansion fan through the shock layer was determined by using the solution to the Taylor-Maccoll set of differential equations.

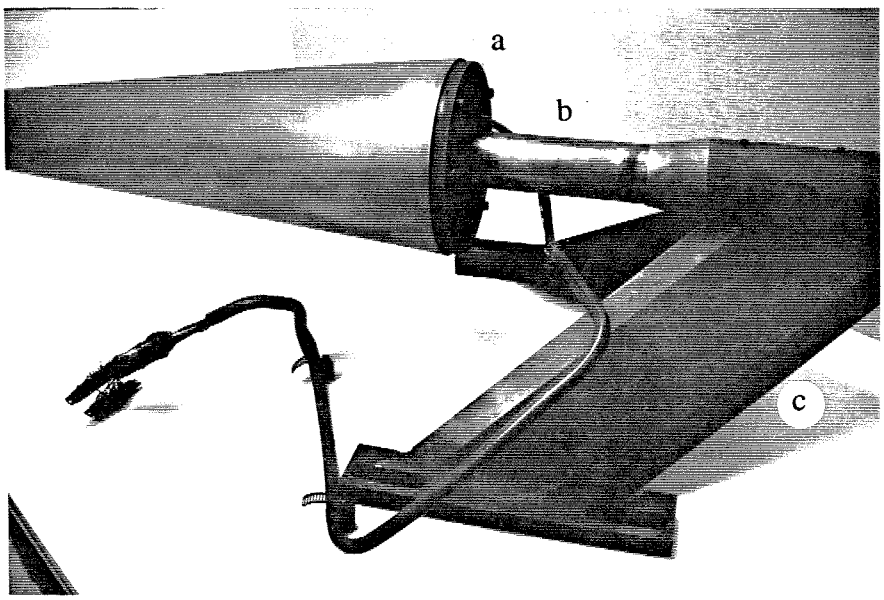

FIG. 3.5. Close-up view of the model back showing the cone base plate (a), the sting (b) and the sting mount (c).

3.3.2 Heat transfer gauges

Fifteen thermocouples of type E (chromel-constantan), manufactured by Medtherm Corp., were mounted flush with the surface of the cone to measure the heat transfer distribution (see Fig. 3.9). Table 3 gives their location as a function of the distance x from the tip along the centerline and as a function of the roll angle θ from the separation plane of the two half-cones. The gauges were distributed in this way to maximize the angle between them. At the time they were installed, it was not known if the first gauges would trip the boundary layer and cause the gauges further downstream to give a false reading[4]. It was desirable also to accommodate the transducers on only one side of the cone (the other half being left free for future investigations).

[4] It was found later that the gauges would probably not trip the boundary layer if they were positioned behind each other. In Chapter 7, experimental results show that an obstacle needs to be much more important in size to trip the boundary layer.

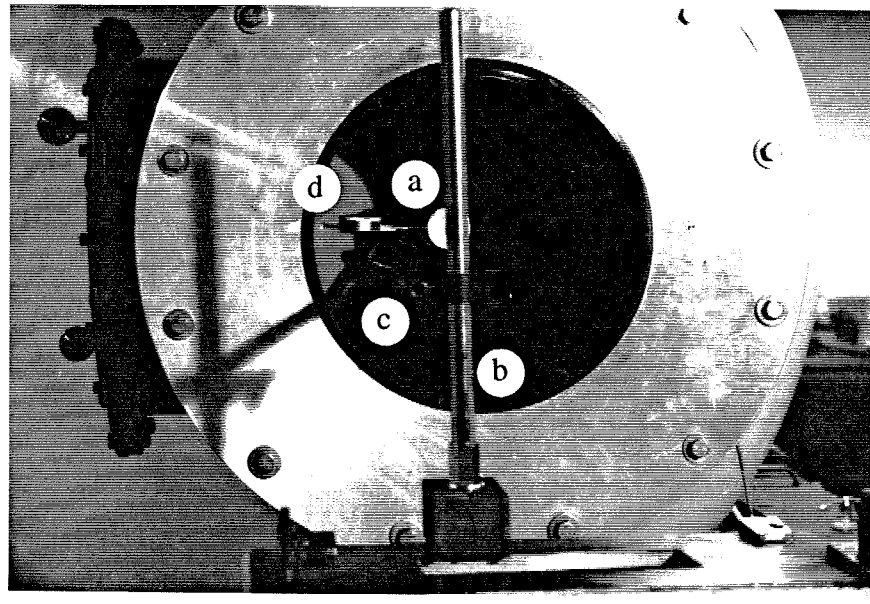

FIG. 3.6. View of the front end of the test section during the longitudinal alignment of the sting mount (yaw angular position). The stainless steel bar (a) is partly hidden by the post (b) supporting the rod (c) and the dial-indicator (d). See text for details of the procedure.

The coaxial thermocouples are 1.6 mm in diameter. They were all sanded flush with the surface and then polished to remove any aluminum particles that could produce a different type of thermoelectric junction. The junction was formed by scribing smoothly the exposed surface with the tip of a sharp razor blade, under a microscope, in order to avoid contamination from the aluminum of the model. The cold junction was the feed-through plate for signal cables from the test section to the laboratory. Since only changes in temperature need to be measured for the determination of the heat transfer rate, the temperature of the cold junction is not important, since it does not change during a shot. The voltage signals were recorded ($\pm 0.5\%$) at a sampling rate of 200 kHz after being amplified by a factor of 500 ($\pm 1.5\%$). A standard correlation, given by Omega Engineering, Inc. (1992), was used to convert these signals to temperature signals ($\pm 1\%$).

Following Schultz and Jones (1973), given that the test time is short compared to the heat penetration time into the gauge, the one-dimensional semi-infinite slab theory was used

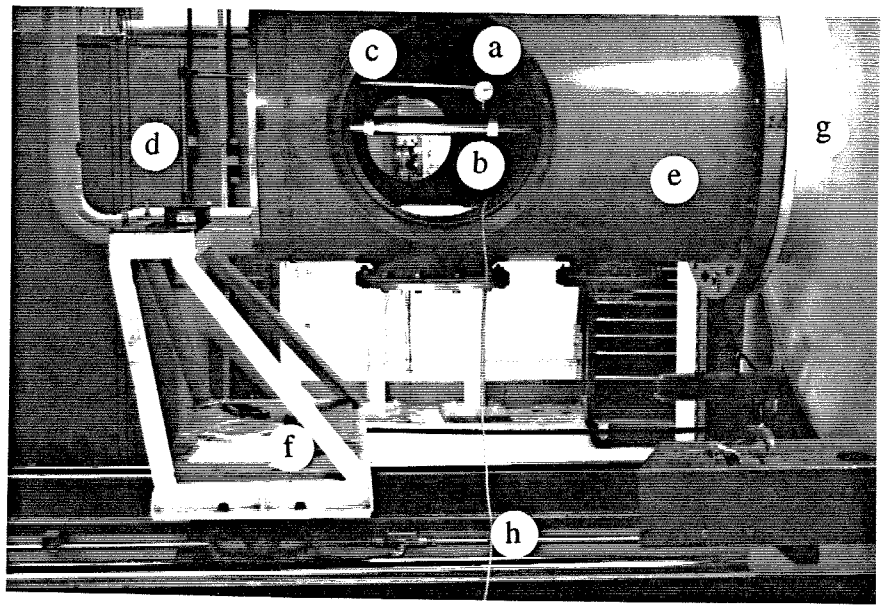

FIG. 3.7. Side view of the test section during the longitudinal alignment of the sting mount (not seen). The dial-indicator (a) is set to determine the pitch angle and is held above the bar (b) by a rod (c) attached to a post (d) outside the test section (e). This post is clamped on the top of the nozzle-support trolley (f). The test section is bolted to the dump tank (g). These and the trolley have one degree of freedom along the centerline of the nozzle (not shown). They are sliding on a pair of carefully aligned rails (h).

to reduce the temperature traces to heat transfer rate traces. This gives

$$\dot{q}(t) = \sqrt{\frac{\rho c k}{\pi}} \int_0^t \frac{dT(\tau)}{d\tau} \frac{d\tau}{\sqrt{t-\tau}}. \tag{3.1}$$

Since a digitized signal is processed, it is necessary to express this integral as

$$\dot{q}(t_n) = 2\sqrt{\frac{\rho c k}{\pi}} \sum_{i=1}^{n} \frac{T(t_i) - T(t_{i-1})}{\sqrt{t_n - t_i} + \sqrt{t_n - t_{i-1}}}. \tag{3.2}$$

Computing $\dot{q}(t)$ with this expression is called the direct method. An alternative method is to integrate first

$$Q(t) = \sqrt{\frac{\rho c k}{\pi}} \int_0^t \frac{T(\tau)}{\sqrt{t-\tau}}, \tag{3.3}$$

where the finite-difference representation is

$$Q(t_n) = \sqrt{\frac{\rho c k}{\pi}} \sum_{i=1}^{n} \frac{T(t_i) - T(t_{i-1})}{\sqrt{t_n - t_i} + \sqrt{t_n - t_{i-1}}} (t_n - t_{n-1}), \tag{3.4}$$

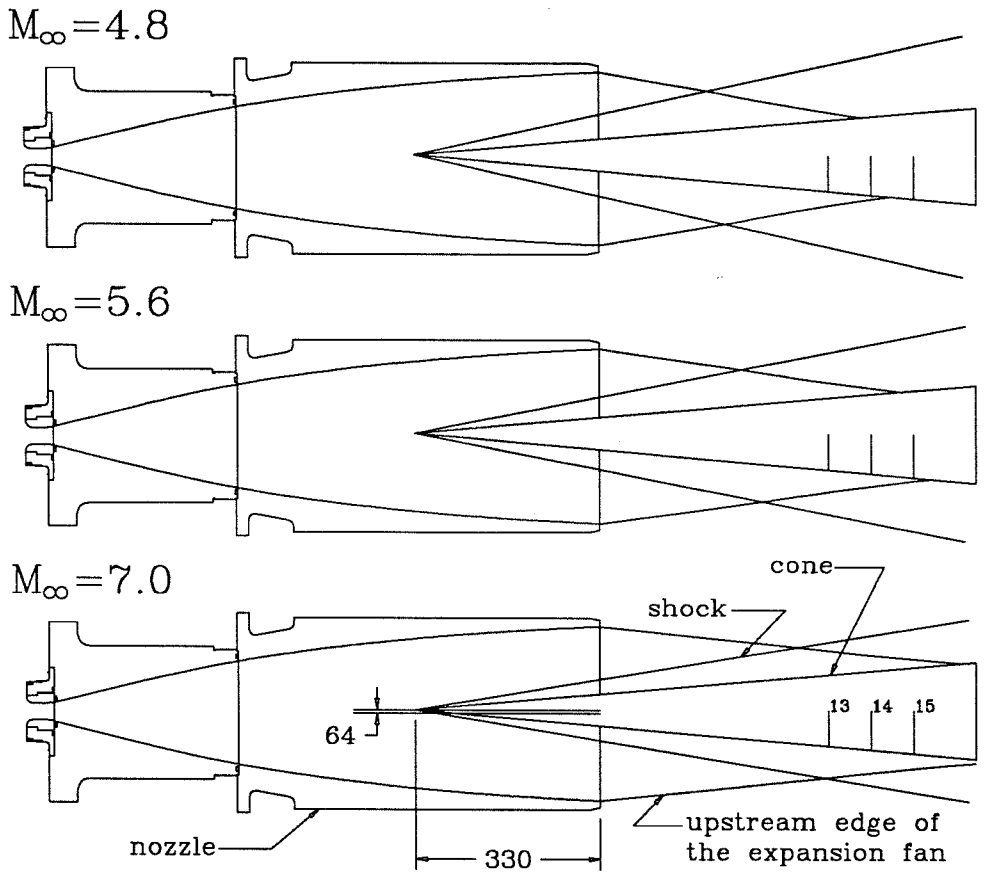

FIG. 3.8. Scale drawings showing the impingement of the expansion fan on the cone surface, at different Mach numbers. The dimensions are in millimeters.

and then to differentiate

$$\dot{q}(t_n) = \frac{\mathrm{d}Q(t_n)}{\mathrm{d}t} = \frac{1}{40\,(t_n - t_{n-1})}\,(-2Q_{n-8} - Q_{n-4} + Q_{n+4} + 2Q_{n+8})\,. \qquad (3.5)$$

This is called the indirect method and the only advantage it has over the former is the resulting smoother data because of the intermediate step of computing the integral. In both cases, the computation is slow due to the nature of the integral.

The value of $\sqrt{\rho c k}$ for the gauge material was determined to be 8919 $\mathrm{Ws^{1/2}/(m^2 \cdot K)}$ as follows. The thermal diffusivity α_{diff} ($\equiv k/(\rho c)$) of chromel and constantan are 4.90×10^{-6} and 5.94×10^{-6} $\mathrm{m^2/s}$, respectively. The value of α_{diff} for the thermoelectric junction is taken as the average of these two values giving $\alpha_{diff} = 5.42 \times 10^{-6}$ $\mathrm{m^2/s}$. Similarly, the thermal conductivities k are 19.0 and 22.5 $\mathrm{W/(m \cdot K)}$, respectively. The average is therefore 20.8 $\mathrm{W/(m \cdot K)}$. Substituting, we find an average value of $\sqrt{\rho c k}$ for the junction

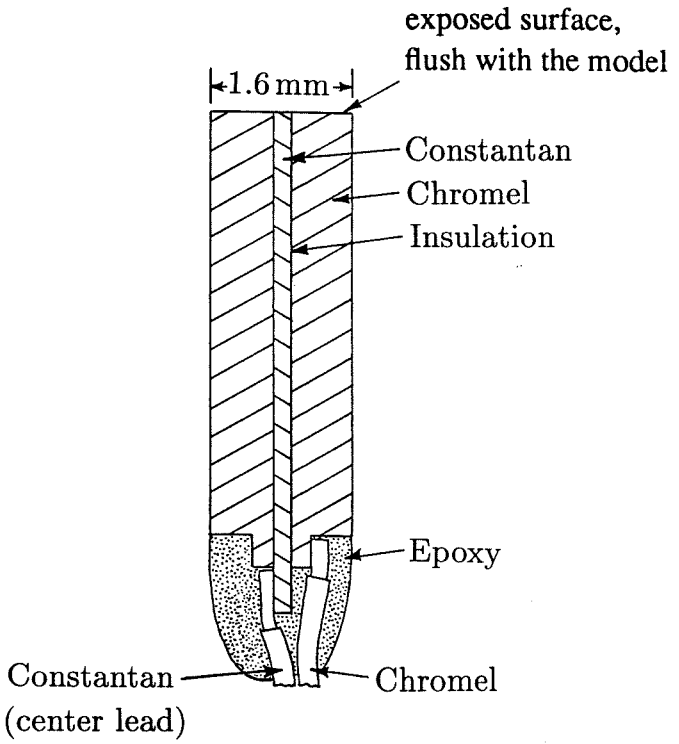

FIG. 3.9. Schematic diagram of a coaxial thermocouple.

gauge no.	x, mm	θ, deg.
1	241	90
2	260	80
3	279	100
4	298	70
5	318	110
6	343	60
7	381	120
8	445	50
9	483	130
10	533	40
11	584	140
12	660	30
13	737	150
14	813	20
15	889	160

Table 3. Location of the heat transfer gauges on the cone.

based on the bulk properties of each metal. This leads to an additional error of $\pm 4\%$ in the final value of the heat transfer rate. Despite the fluctuations of the traces, the variability from shot to shot is low after normalization (of order $\pm 3\%$). For example, results of two identical shots are shown in Fig. 3.10.

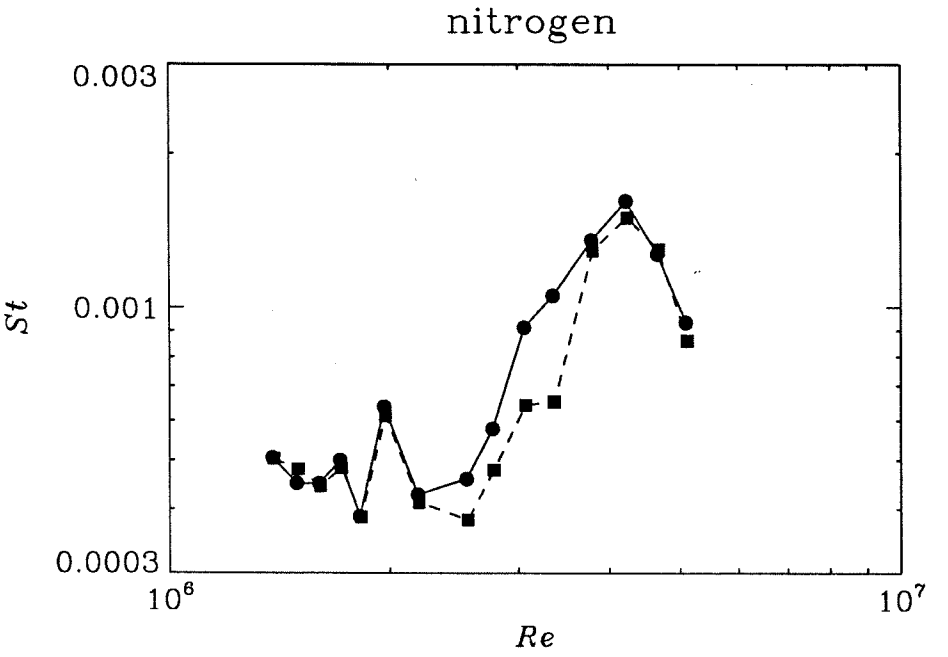

FIG. 3.10. Normalized heat transfer distributions of two consecutive shots with nominally the same conditions (squares: run 145, circles: run 146), h_0 = 12 MJ/kg, p_0 = 60 MPa, pure nitrogen.

From the error values given above, the accuracy in $\dot{q}$ is of order $\pm 10\%$. The time response is approximately 1 μs according to the manufacturer, Medtherm Corporation. In all the plots shown in this thesis, the error bars represent an accuracy of 15%. For the cases where $h_0 > 16$ MJ/kg, the error bars represent an accuracy of 25%. This increase is due to electrical noise present when $h_0 > 16$ MJ/kg as explained in Chapter 7. Performing an experiment in the T3 shock tunnel with a blunt cone and using similar gauges, Gai and Joe (1992) assessed the accuracy to be on the order of 15% and the corner frequency response of the order of 100 kHz. This response frequency is quite adequate for our tests since the test time is typically 1.5-2 ms. The value of the heat transfer rate was averaged for a period of typically 1 ms (long enough to reduce the scattering without affecting the level), the center of which was chosen at a certain time after the flow start (in general 1.5 ms) depending on the reservoir conditions. In general, the useful test time starts 0.5 ms after the beginning of the starting process and ends either when the conditions are no longer constant, or when the driver gas contaminates it. Only indirect information is available about the onset of contamination, see Hornung (1992), Skinner (1992), and Slade *et al.* (1993).

3.4 Flow visualization

Different techniques were tried to visualize the boundary layer. The Schlieren method could not work due to the floor vibrations produced by the facility during its recoil. Mirror vibrations caused the focus point of the source light to move with respect to the knife edge. Shadowgraphy barely allowed the detection of the conical shock. Laser differential interferometry, described by Smeets and George (1973), is more sensitive and, at low enthalpy, gives insight into whether the boundary layer is turbulent or not, see Fig. 3.11 and Fig. 3.12. But no information can be obtained on the boundary layer structure or on the transition process. All the images were recorded on Kodak film Tmax 400 (4 inches $\times$ 5 inches).

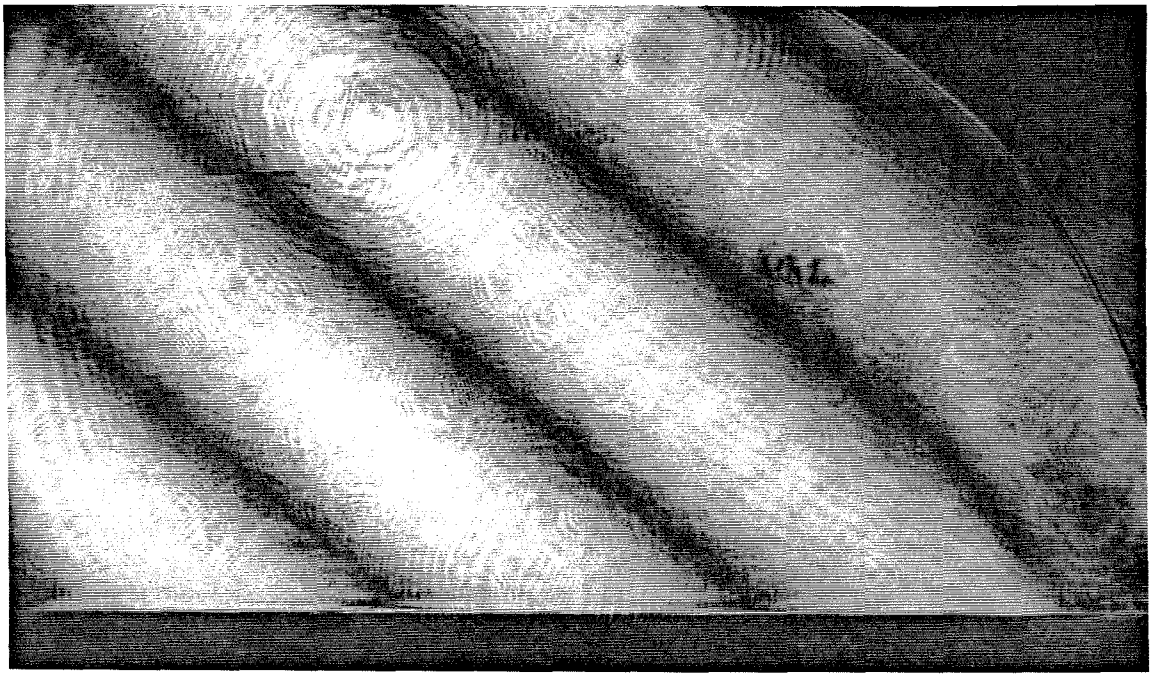

FIG. 3.11. Interferogram of a boundary layer either in a laminar or transitional regime. The run conditions were h_0 = 11 MJ/kg, p_0 = 60 MPa, pure nitrogen (run 146, refer to 534 in Table 2). The picture shows the boundary layer on the top of the 5 deg. half-angle cone, starting on the left from x = 225 mm (corresponding to Re = 9.29 million) to x = 345 mm (Re = 12.8 million).This picture was taken 1.5 ms after the nozzle reservoir pressure rise.

With the exception of the lowest enthalpy conditions of the present tests, the sensitivity of flow visualization techniques that rely on optical path length changes of the gas across

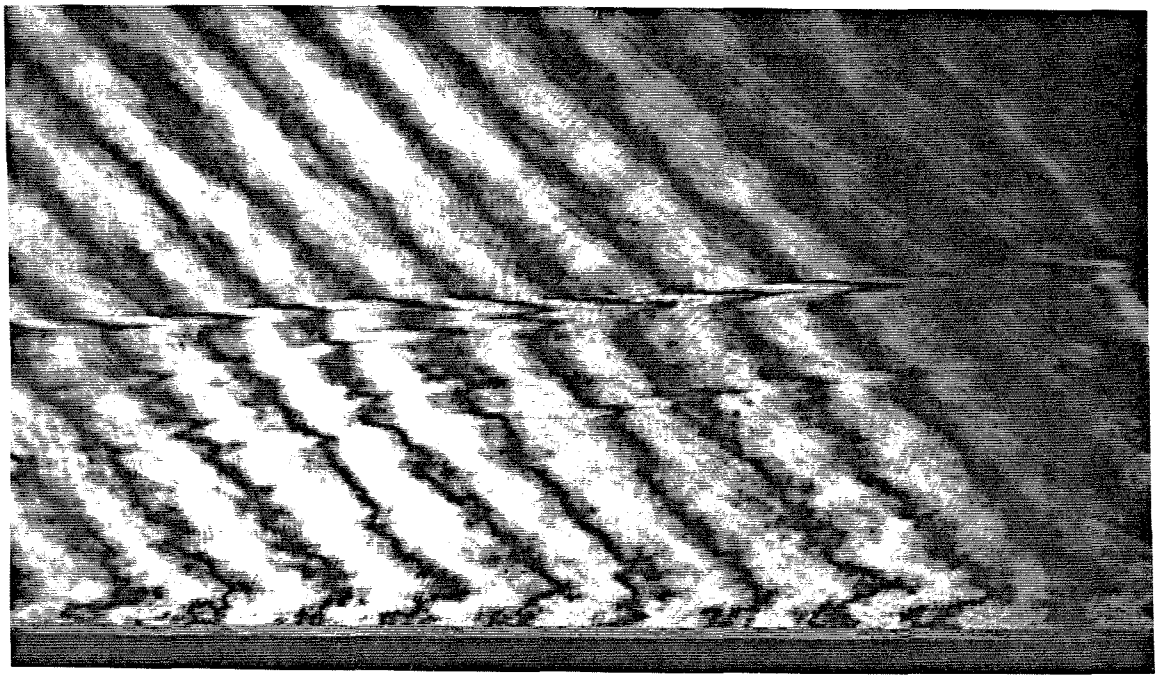

FIG. 3.12. Interferogram of a boundary layer in a turbulent regime. The run conditions were h_0 = 3.4 MJ/kg, p_0 = 55 MPa, pure nitrogen (run 147, refer to 349 in Table 2). The picture shows the boundary layer on the top of the 5 deg. half-angle cone, starting on the left from x = 314 mm (corresponding to Re = million) to x = 434 mm (Re = million).This picture was taken 1.5 ms after the nozzle reservoir pressure rise.

the flow field is insufficient. The sensitivity is insufficient because the cone is slender, so that the geometrical path length through the boundary layer is necessarily small. Thus, Schlieren photography or shadowgraphy or interferometry in the conventional form are just not sensitive enough.

To solve this problem, the idea of resonant enhancement of the refractive index of the medium was used, *e.g.*, see Blenstrup *et al.* (1979). This technique relies on the fact that the refractive index of a gas is singular at a spectral line of the medium. The value of the refractive index at this maximum is very considerably above the broad-band value. For example, the benefit of this phenomenon may be obtained in the visible range by seeding the flow with sodium and using a light source with a wavelength just off the center of one of the D-lines. Even if the light source wavelength is not perfectly tuned, such that it is in the

center of the D-line, for example, where the refractive index contribution of the line is zero, the absorption of the light by the resonance is very high. The technique functions differently and becomes analogous to dye injection in water. The 'salt deposition technique' will still work satisfactorily for qualitative flow visualization with good repeatability.

In our experiment, a preferential enhancement of the sensitivity of the boundary-layer fluid was desirable, so we seeded the flow only within the boundary layer by depositing a very small drop of a saturated saline solution on the portion of the cone surface of interest. This was then left to dry, so that a thin film of salt was left to be ablated during the test. When examined with a microscope, this film would actually consist of a few cubic crystals 100 μm high spaced 2 or 3 mm apart.

The light source used was a tunable dye-laser built for this purpose. It is pumped by a Neodymium:YAG laser. Only one picture is taken during each run. The laser is triggered by an adjustable delay circuit which in turn is triggered by the arrival of the shock at the end of the shock tube. The technique was first used to enhance the sensitivity of the differential interferometry, set to be sensitive to density gradients parallel to the flow direction. The resulting images are called 'resonantly enhanced interferograms'. When the differential interferometer was removed , *i.e.*, the Wollaston prism and the two polarizers, it was found that the technique worked better. This removal also avoided the annoying double image associated with differential interferometry. Thus, the optical setup was redesigned to be a shadowgraph apparatus. The resulting images are called 'resonantly enhanced shadowgraphs'. The resonant enhancement of refractive index turned out to be particularly successful at high enthalpies where it was most needed due to the lower density, partially because of the relatively higher temperature in the boundary layer which causes the salt to be ablated more effectively. For cases where salt crystals were not hot enough to dissociate, the resulting images became effectively either interferograms or shadowgraphs, depending on the optical configuration. Fig. 3.13 shows the arrangement of the optical components used. The salt deposited on the wall may, of course, cause a perturbation to the boundary layer flow. We will address this question in Chapter 7. Fig. 3.14 shows a schematic diagram of the model, the optical window (actually one on each side of the model), and the limits of

a typical picture shown in this thesis. This view is always oriented parallel to the surface of the cone and always shows the flow going from left to right.

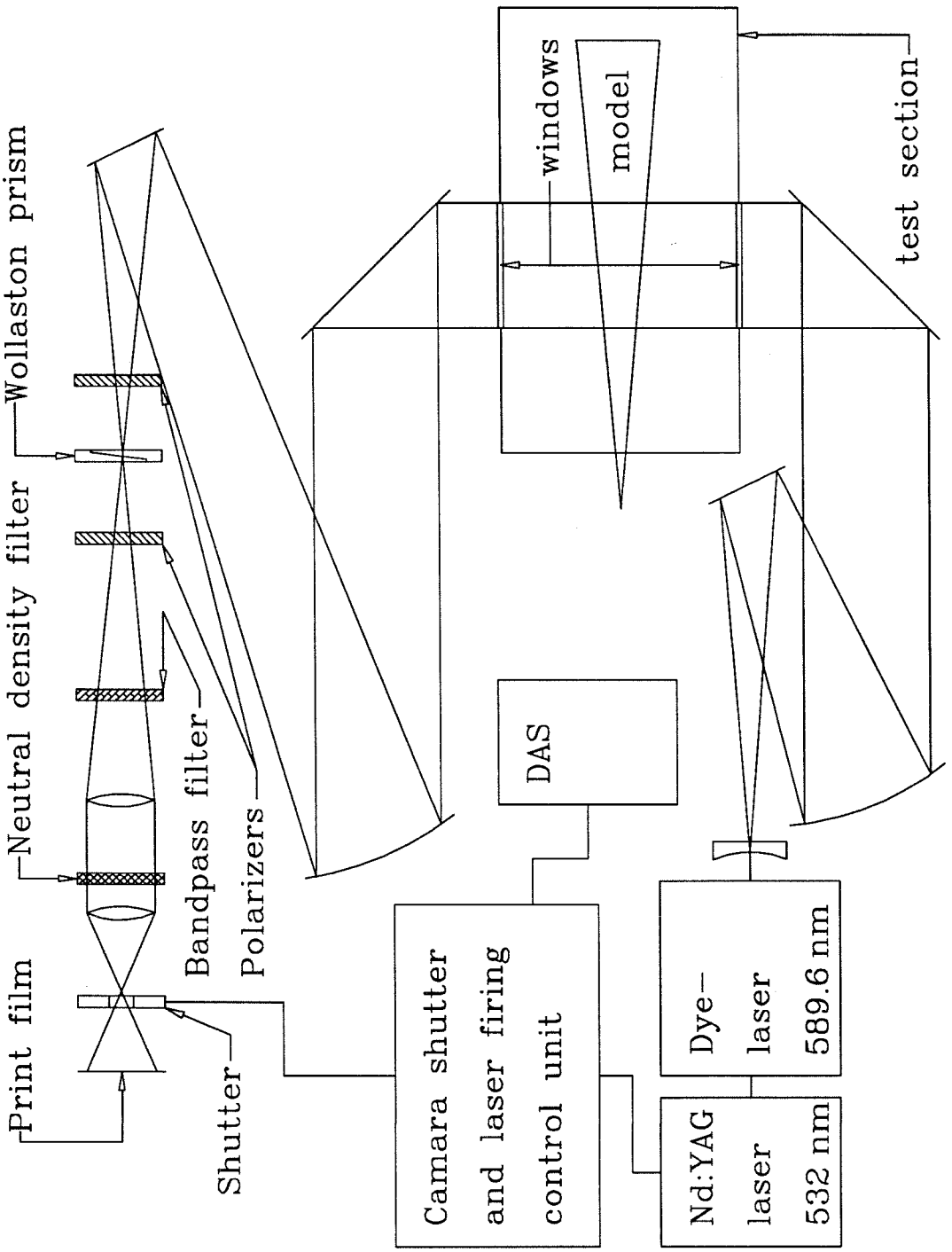

FIG. 3.13. Schematic diagram of the optical arrangement. The neutral density filter is used to get rid of the luminosity emitted from the test gas. The bandwidth of the bandpass filter is 10 nm centered at 590 nm. The dye solution used in the dye-laser is Rhodamine 6G (610 nm) diluted in methanol.

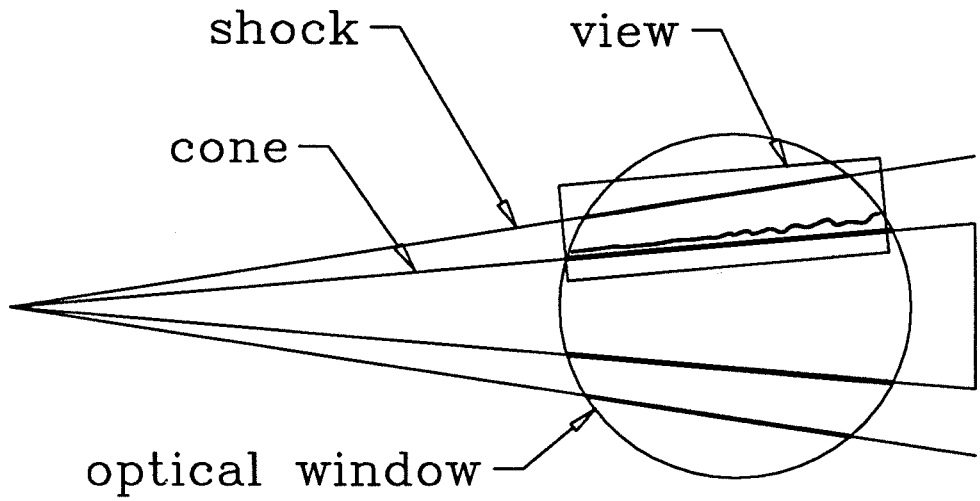

FIG. 3.14. Schematic diagram explaining the the photographs shown in the following chapters. A picture is either from the top (as shown here) or from the bottom of the cone. The flow is always seen going from left to right and the shock is rarely visible.

3.5 Image processing

This section is a description of the image processing which consists of several steps. First, 8"×10" prints were made from all the negatives using a development process for the highest possible contrast[5]. Second, except for Fig. 3.11 and Fig. 3.12, the prints were digitized and enhanced numerically. Some images were very dark or had some flow features that were difficult to see. The image scanner was digitizing the prints either at 600 dots per inch (DPI) or at 300 DPI for the larger images. For each dot, a value varying between 0 (black) and 255 (white) was read depending on the local intensity of the image. All the pixels and their intensity values were read by a computer which could then reassign a new intensity value (generally higher). This is shown schematically in Fig. 3.15. The computer images were then recorded on film. Prints were finally made using a normal development process.

[5] Each image was printed on Polycontrast III grade M paper with a Kodak filter number 5 (the number ranges from 1 to 5: number 2 is for normal prints and numbers 3 through 5 are for high contrast).

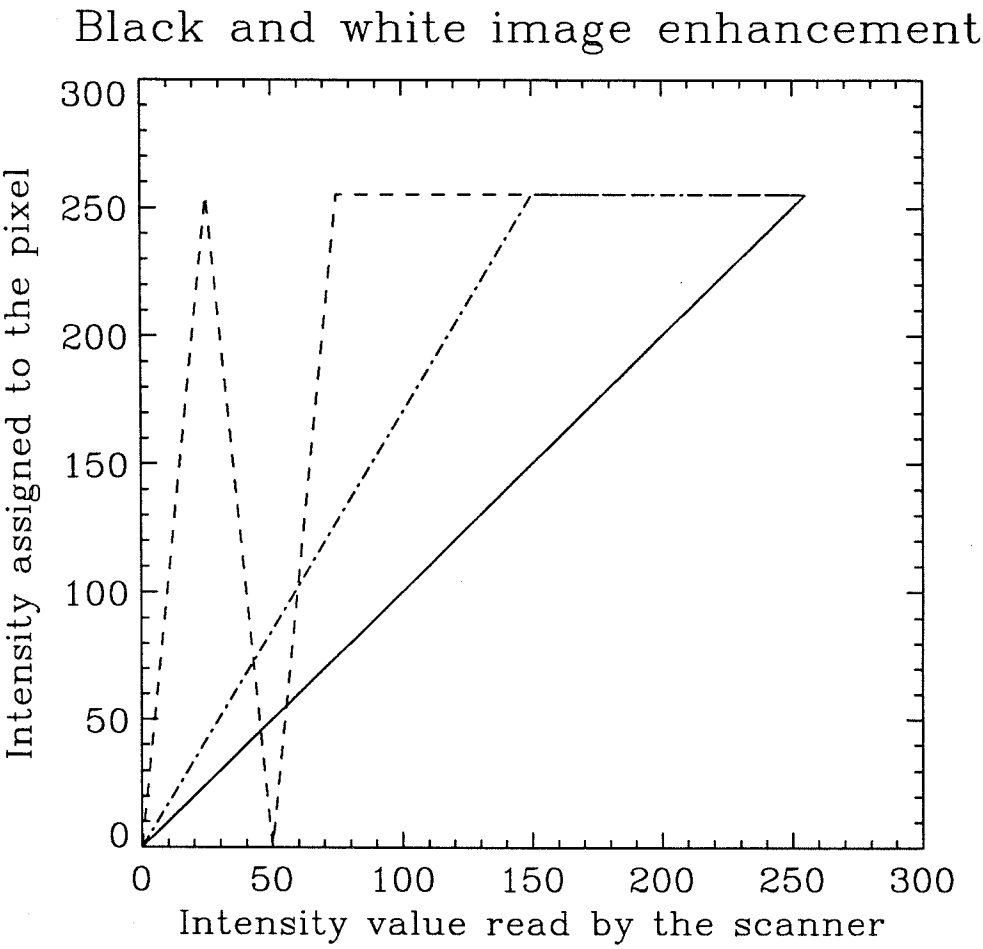

FIG. 3.15. Sketch of the intensity value assigned to a pixel versus the intensity value as read by the image scanner. Shown here as the continuous line is the intensity distribution before digital enhancement. –·–·–·–·–: scheme A which corresponds to the majority of the images presented in this document. – – – – – – – –: scheme B which corresponds to some of the small images (these will be indicated as 'scheme B').

3.6 Chapter summary

In this chapter, the flow facility was presented together with the method used to compute the free-stream parameters from measurements of the pressure upstream of the nozzle throat. The thermocouple instrumentation was also presented as well as a method to reduce the voltage signals to heat transfer signals. The qualitative flow visualization method was also described along with a method to enhance the resulting pictures. In the next three chapters, a series of results is presented corresponding to the three different regimes of the boundary layer.

CHAPTER 4

Experimental results - Laminar regime

In this chapter, results of the heat transfer rate measurements are compared with theoretical predictions for the laminar regime. Runs with either air or nitrogen were performed as well as runs with different stagnation enthalpies or pressures given in Table 1. These conditions were chosen such that comparisons can be made between runs for which the flow was expected to be frozen and runs for which real-gas effects were expected to be present. Runs with either air or nitrogen were also performed to bring out differences which were expected to be due to real-gas effects.

4.1 Theoretical predictions

To show an example of behavior differences between a frozen flow and a chemical equilibrium flow, we focus on the flow condition corresponding to a specific enthalpy, h_0, of 22 MJ/kg and stagnation pressure, p_0, of 55 MPa. Going through the calculation procedure outlined in Chapter 2, we find for a frozen flow

$$St_{air} = \frac{0.533}{Pr^{2/3}Re^{1/2}} \quad \text{and} \quad St_{nitrogen} = \frac{0.536}{Pr^{2/3}Re^{1/2}}. \tag{4.1}$$

If we include the correction factor for real-gas effects (chemical equilibrium), we find

$$St_{air} = \frac{0.739}{Pr^{2/3}Re^{1/2}} \quad \text{and} \quad St_{nitrogen} = \frac{0.669}{Pr^{2/3}Re^{1/2}}. \tag{4.2}$$

Using the $h = h(u)$ relation developed in Chapter 2, we would obtain $T_m = 5,800$ K for a frozen flow (of either air or nitrogen with $\alpha = 0$). At chemical equilibrium, T_m would decrease to 5,500 K for nitrogen and to 4,180 K for air. This difference is certainly attributable to more dissociation in the case of air. We can also compare these predictions with that of low specific enthalpy (same for air and nitrogen) corresponding to $h_0 = 5.8$ MJ/kg and to $p_0 = 15$ MPa

$$St = \frac{0.487}{Pr^{2/3}Re^{1/2}}. \tag{4.3}$$

Thus, frozen flow predictions are all in the same range regardless of the stagnation conditions. For each data set presented in Chapters 4 through 6, the laminar and turbulent predictions are calculated at the corresponding run conditions.

4.2 Time traces of the experimental data

Before proceeding to the normalization of the data, it is important to check how steady the heat transfer rate distribution is. Fig. 4.1 shows typical time traces corresponding to one of the conditions mentioned above for nitrogen. Clearly, the signals become steady after around 0.5 millisecond after they start to rise. The flow takes roughly this time period to get established. This period corresponds also to the nozzle starting process during which the signal is noisiest especially at high specific enthalpy and density. Chapter 7 presents a discussion of the possible cause of this phenomenon. Despite these fluctuations, less severe in the steady part of the signals, it is still possible to obtain a value for the local heat transfer rate. However, because of the time integration process of the signal (described in Chapter 3), the severe fluctuations encountered during the nozzle starting process still persist to some degree in the period where the signal is averaged. As shown on Fig. 7.9 and as discussed in Chapter 7, the additional uncertainty on the heat flux value is of order $\pm 15\%$. This problem is not encountered in runs where $h_0 < 16$ MJ/kg (at any reservoir pressures).

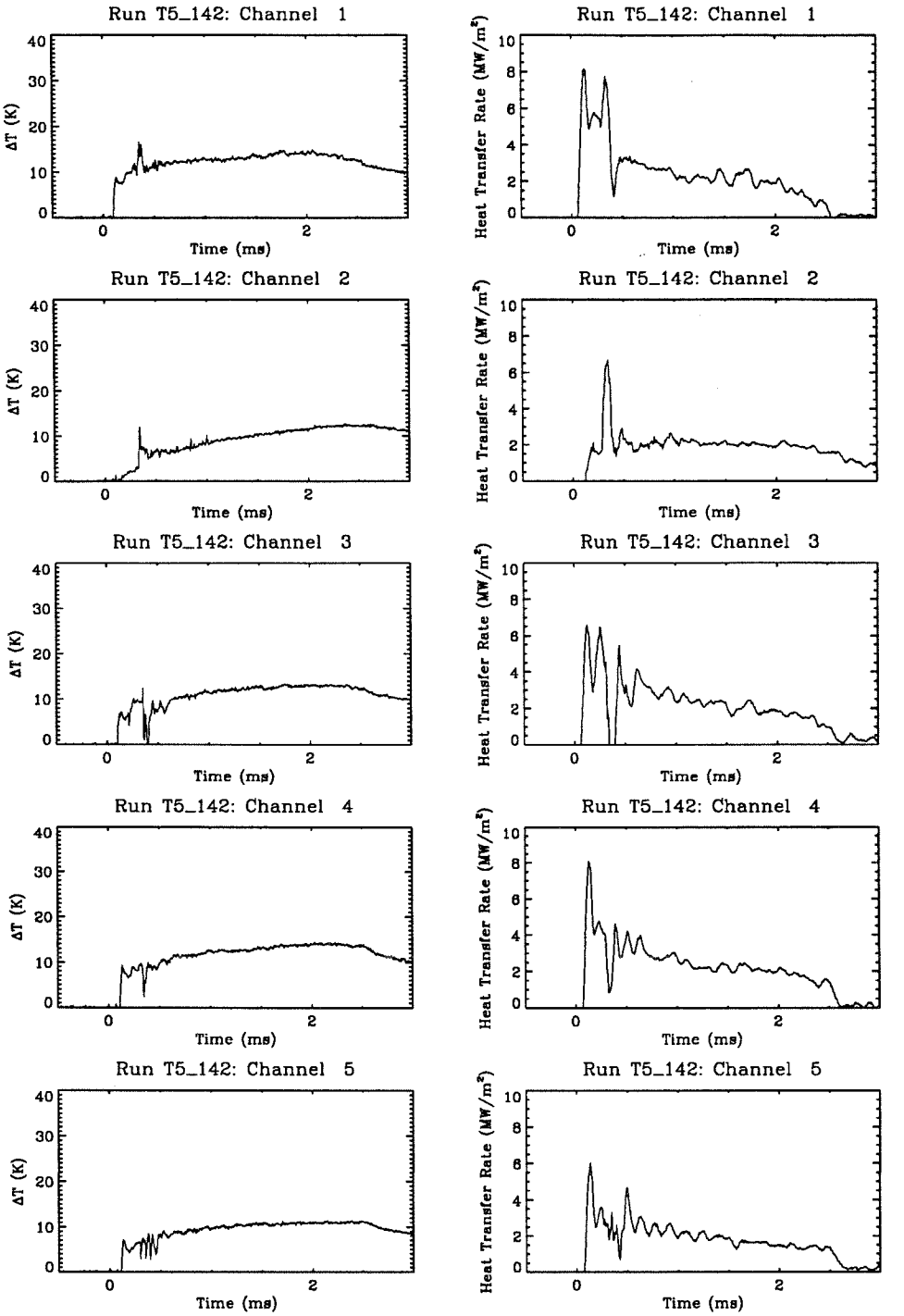

FIG. 4.1a. Typical time traces of the thermocouples. On the left are the voltage signals after conversion to temperature units and on the right are the result of the process converting them to heat tranfer rate time signals. The conditions for this particular shot were h_0 = 22 MJ/kg and p_0 = 60 MPa, pure nitrogen (refer to run 140, Table 2).

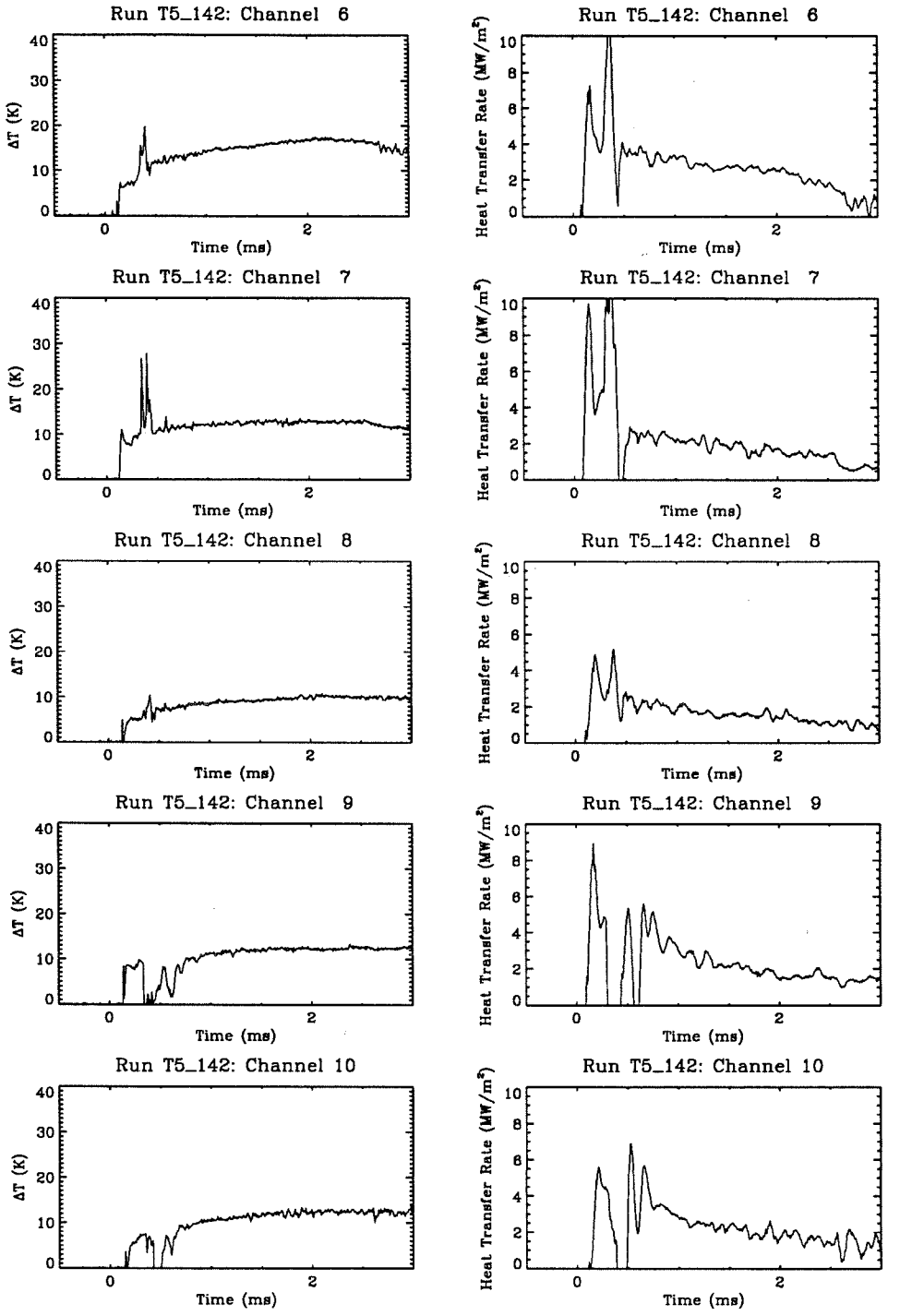

FIG. 4.1b. Continued. Typical time traces of the thermocouples. On the left are the voltage signals after conversion to temperature units and on the right are the result of the process converting them to heat tranfer rate time signals. The conditions for this particular shot were h_0 = 22 MJ/kg and p_0 = 60 MPa, pure nitrogen (refer to run 140, Table 2).

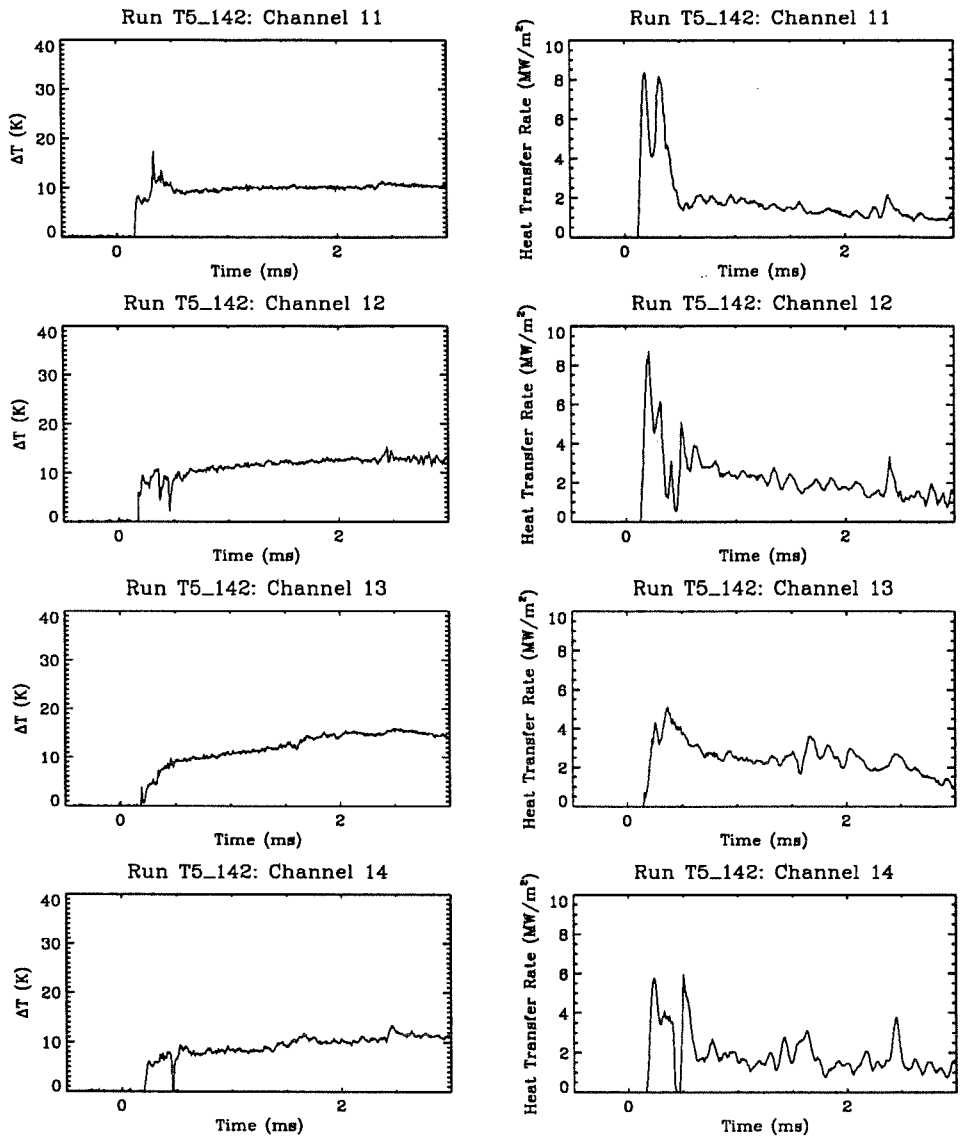

FIG. 4.1c. Continued. Typical time traces of the thermocouples. On the left are the voltage signals after conversion to temperature units and on the right are the result of the process converting them to heat tranfer rate time signals. The conditions for this particular shot were h_0 = 22 MJ/kg and p_0 = 60 MPa, pure nitrogen (refer to run 140, Table 2). The last thermocouple was not working properly and was disconnected from the recorder at the time this run was conducted.

4.3 Comparison with experimental data

The normalized experimental results corresponding to each of the reservoir conditions mentioned above are shown in Fig. 4.2 and Fig. 4.3 for nitrogen and air respectively. The experimental data agree relatively well with the similarity theory extended to compressible axisymmetric frozen flow. The data shown as squares (p_0 = 24 MPa and $h_0 \approx$ 12 MJ/kg) indicate a frozen flow behavior as observed by East *et al.* (1980) on a flat plate. The rms error as defined in Chapter 2 is of order 10%. At high specific enthalpy (h_0 = 22 MJ/kg), the data are more scattered (the rms error is of order 16%) but fall clearly above the prediction of a frozen flow, indicating a nonequilibrium effect as recombining atomic species cause a higher heat release to the wall. The presence of these atomic species is due to the combined effect of free-stream dissociation and frictional heating in the boundary layer (see Table 1, p. 32). The data for air reach a higher level than the data for nitrogen because of a higher concentration of atomic species including oxygen atoms. The exothermic reactions are the cause of this difference which is also evident when the specific enthalpy is lowered to 15 MJ/kg for nitrogen and to 14 MJ/kg for air (p_0 = 55 MPa). The level of atomic mass fraction α is difficult to estimate because of the scatter of the data.

In Fig. 4.4 showing the data for air at h_0 = 14 MJ/kg, we compare data for two runs at p_0 = 55 MPa (ρ_e = 0.05 kg/m^3) and at p_0 = 85 MPa (ρ_e = 0.08 kg/m^3). The evidently higher heat release at the higher pressure indicates a more extensive real-gas effect. In Fig. 4.4, the data are above the theoretical predictions for a laminar boundary layer in chemical equilibrium. This could indicate that there are more atomic species recombining at the wall and therefore could indicate a nonequilibrium effect as there might be overdissociation in the boundary layer due to the combined effect of free-stream dissociation and frictional heating.

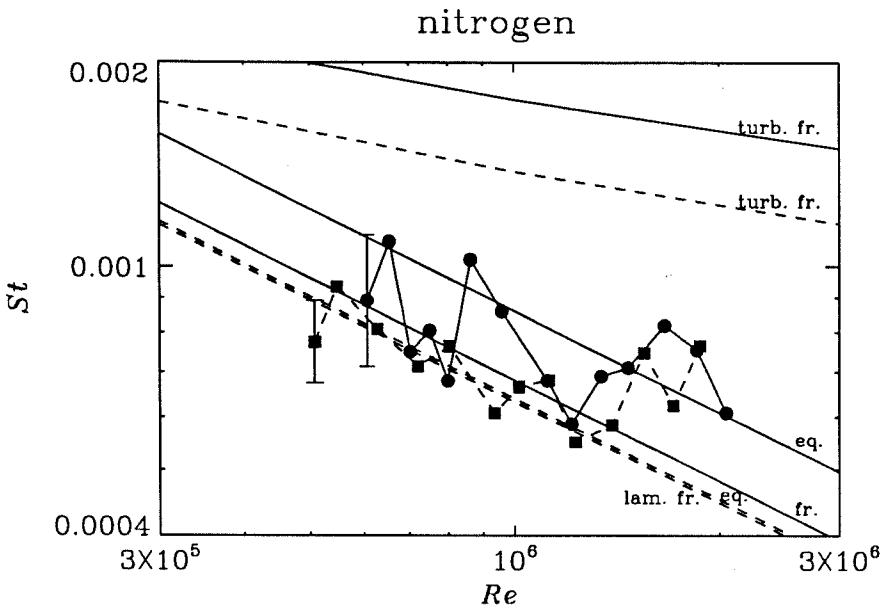

FIG. 4.2. Normalized heat transfer measurements of two different shots in T5. Squares (run 544): h_0 = 12 MJ/kg and p_0 = 24 MPa; circles (run 140): h_0 = 22 MJ/kg and p_0 = 60 MPa. The theoretical predictions for these nitrogen runs are also plotted.

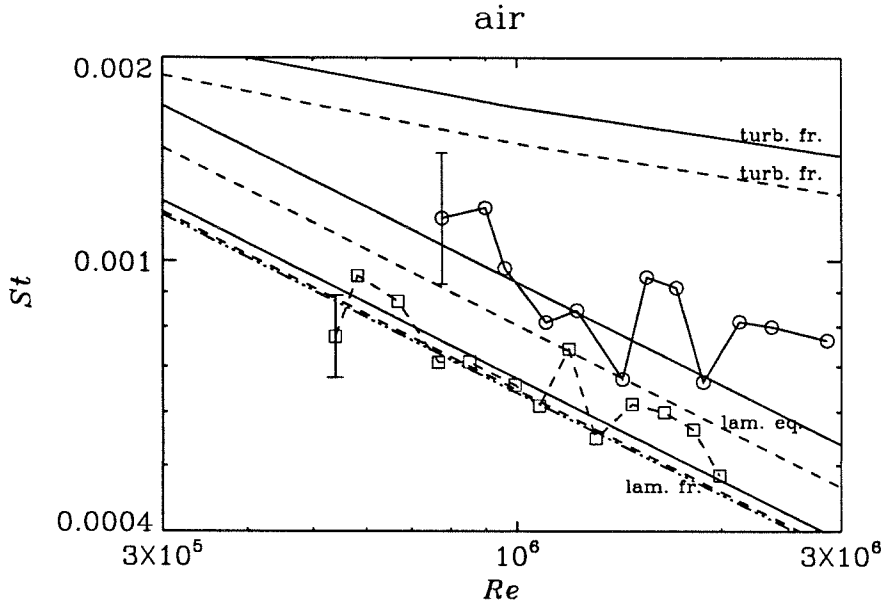

FIG. 4.3. Normalized heat transfer measurements of two different shots in T5. Squares (run 545): h_0 = 11.3 MJ/kg and p_0 = 24 MPa; circles (run 157): h_0 = 18.5 MJ/kg and p_0 = 60 MPa. The theoretical predictions for these air runs are also plotted. ——·····——: linear curve fit of experimental data obtained from DiCristina (1970) and from Owen *et al.* (1975). The conditions of their experiments were h_0 < 1 MJ/kg and M_∞ = 10 and 7, respectively.

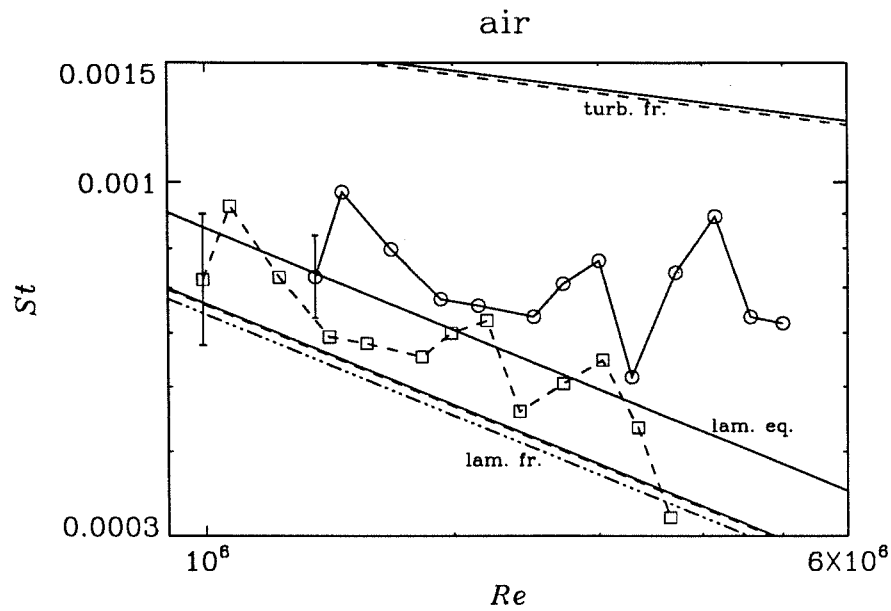

FIG. 4.4. Normalized heat transfer measurements of two different shots in T5. Squares (run 537): h_0 = 14.5 MJ/kg and p_0 = 60 MPa; circles (run 566): h_0 = 14.2 MJ/kg and p_0 = 85 MPa. The theoretical predictions for these air runs are also plotted. ——···——: linear curve fit of experimental data obtained from DiCristina (1970) and from Owen *et al.* (1975). The conditions of their experiments were $h_0 <$ 1 MJ/kg and M_∞ = 10 and 7, respectively.

4.4 Flow visualization

Fig. 4.5 shows a picture taken with the resonant enhancement of the refractive index technique described in the previous chapter. No turbulent patterns can be distinguished. This absence indicates therefore a laminar boundary layer. This observation is confirmed by the heat transfer rate distribution presented earlier. The dark edge of the body appears discontinuous from the point where a small drop of saline solution was deposited (on the left in the picture). Salt crystals are lifted from the surface and dissociate in the boundary layer. Their wake contains sodium atoms which cause the source light to be highly deflected or absorbed. The picture at the bottom shows that no flow patterns can be distinguished without the presence of sodium atoms. The surface of the model appears unbroken and only diffraction patterns due to dust on the optical components can be distinguished. The effect of the salt crystals on the stability of the boundary layer is discussed in Chapter 7.

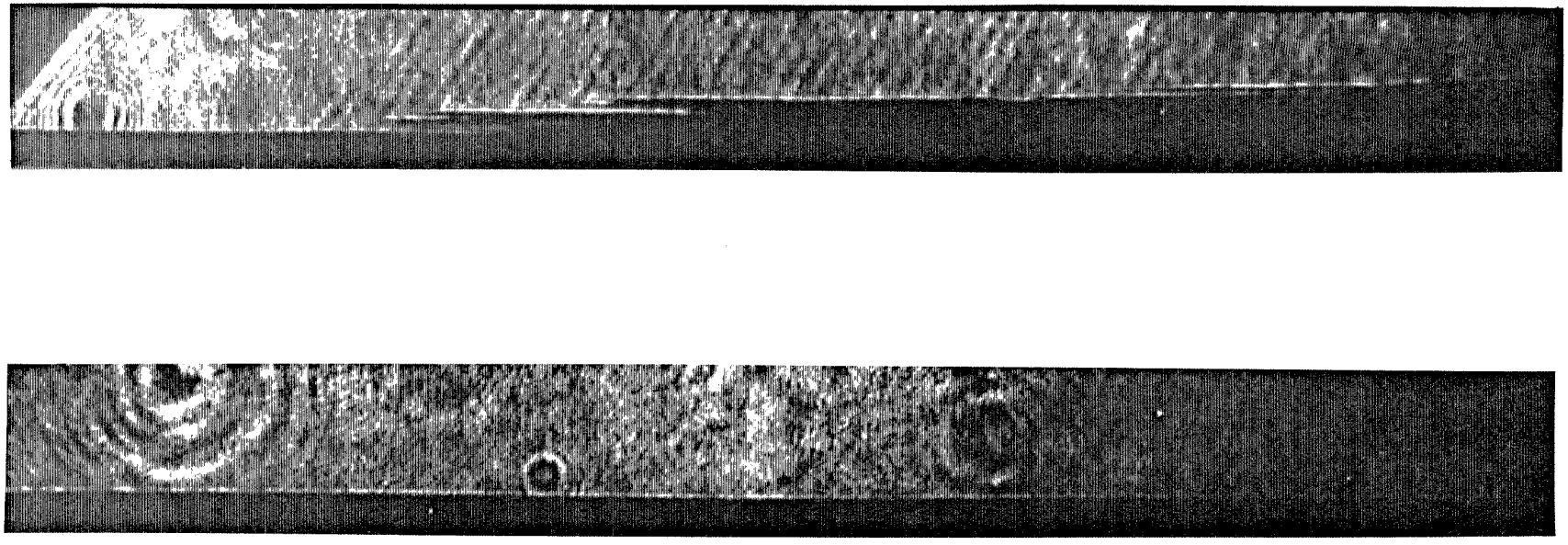

FIG. 4.5. Resonantly enhanced interferogram of a laminar boundary layer taken using the resonant enhancement of the refractive index technique described in the previous chapter. A drop of saline solution was deposited on the top left (at x = 450 mm). On the top picture (top of the model), no flow pattern can be distinguished therefore suggesting a boundary layer in a laminar regime. The bottom picture (bottom of the model) shows no feature at all since there was no salt deposited on this side. The conditions were h_0 = 20.1 MJ/kg and p_0 = 57 MPa, pure nitrogen (run 347, refer to 140). The picture shows the boundary layer on the 5 deg. half-angle cone, starting on the left from x = 420 mm (corresponding to Re = 1.15 million) to x = 590 mm (Re = 1.62 million). This picture was taken 0.75 ms after the nozzle reservoir pressure rise.

4.5 Chapter summary

In this chapter, a series of results corresponding to the laminar regime has been presented. It has been shown that real-gas effects are present and show as an increase in the heat transfer rate at the wall with respect to a perfect or frozen gas flow. This increase is due to recombining reactions of atomic species that have diffused toward the cold wall. The presence of these species is due to free-stream dissociation and frictional heating in the boundary layer (in similar experiments with the same reservoir conditions but with $\alpha_e = 0$, it is presumed that the real-gas effects already observed would be qualitatively the same). Real-gas effects are particularly evident when runs of air and nitrogen at the same nominal conditions are compared. There is a higher heat release in the case of an air flow. An increase of the pressure (and therefore of the density) has the same effect because the recombination rates increase rapidly with density. Flow visualization pictures confirm qualitatively that the boundary layer at these conditions is laminar.

CHAPTER 5

Experimental results - Transitional regime

In this chapter, as in the previous one, comparisons of heat transfer rate measurements are made between runs of different test gases and reservoir conditions. It will be shown that real-gas effects stabilize the boundary layer. Flow visualization is presented giving, in some cases, a qualitative idea of the transition process. A discussion of the steadiness of the time traces is also included.

5.1 Transition Reynolds number and temperature effect

In the example shown in Fig. 5.1 and Fig. 5.2, the normalized experimental data show that the beginning of the transition Re_{tr} corresponds to a Reynolds number of 2.5-3 million whereas its end corresponds to Re = 4 – 5 million. For each run, Re_{tr} is obtained by the intersection of two lines: the first line is a linear fit (of slope -0.5) of the first four data and the second line is a linear least-squares fit of the data points in between this 'laminar line' and the maximum point. The same Re_{tr} are also obtained when p_0 = 55 MPa and $h_0 < 10$ MJ/kg whether the test gas is air or pure nitrogen at M_∞ = 6. For much lower h_0 and p_0, Martellucci and Laganelli (1974) have obtained a transition Reynolds number of 2.6 million for the same model geometry but for a free-stream Mach number of 8, using a continuous hypersonic wind tunnel. This Re_{tr} being on the same order as the ones above indicates that the boundary layer in this transient facility (the T5 shock tunnel) might have reached a steady-state. This does not mean that the transition process is the same in both wind tunnels as will be discussed later.

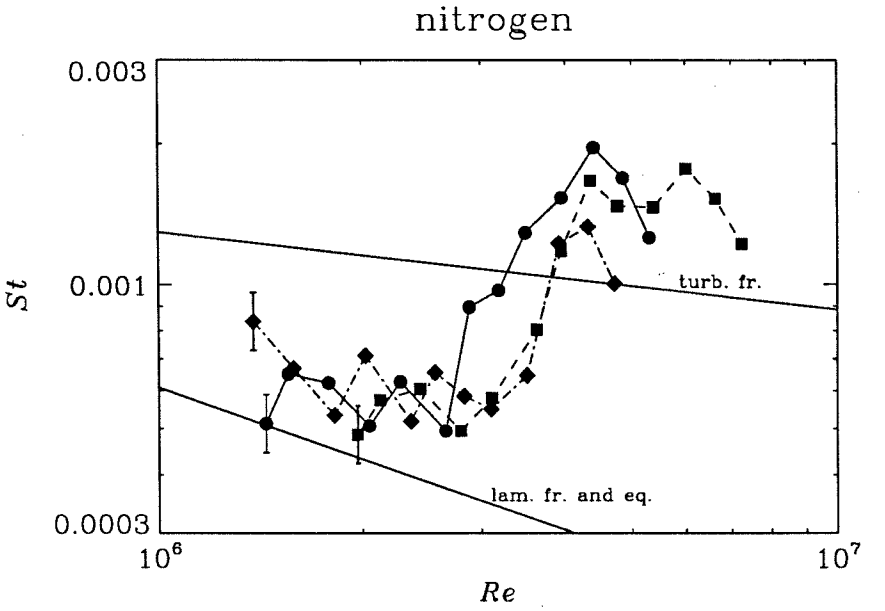

FIG. 5.1. Normalized heat transfer measurements of three different shots in T5. Squares (run 540): h_0 = 7.7 MJ/kg and p_0 = 57 MPa; circles (run 548): h_0 = 9.7 MJ/kg and p_0 = 55 MPa; diamonds (run 534): h_0 = 10.6 MJ/kg and p_0 = 55 MPa. The theoretical predictions for run 548 are also plotted.

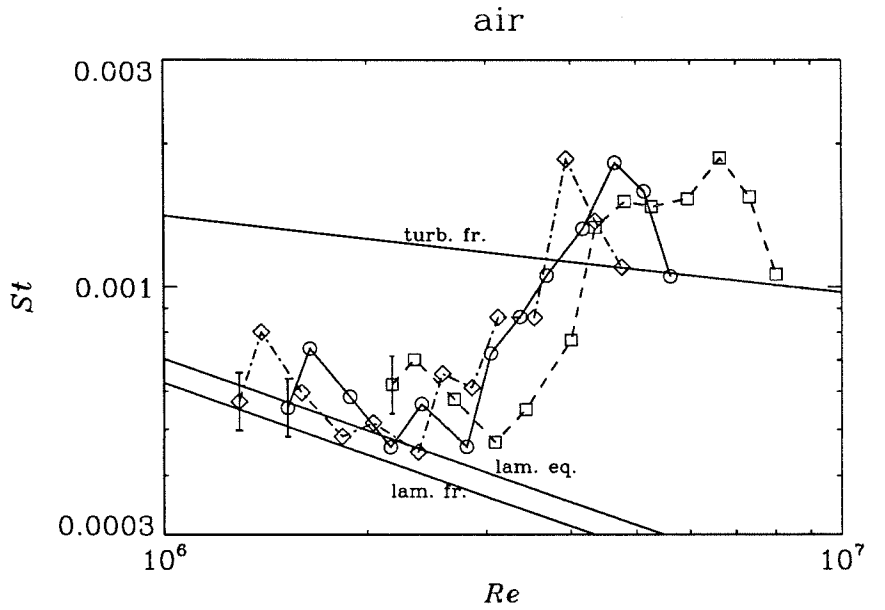

FIG. 5.2. Normalized heat transfer measurements of three different shots in T5. Squares (run 541): h_0 = 7.3 MJ/kg and p_0 = 55 MPa; circles (run 549): h_0 = 9.0 MJ/kg and p_0 = 52 MPa; diamonds (run 556, refer to run 537 in Table 2): h_0 = 10.4 MJ/kg and p_0 = 55 MPa. The theoretical predictions for run 549 are also plotted.

Fig. 5.3 and Fig. 5.4 show the results for conditions where $h_0 \leq 6$ MJ/kg and $p_0 <$ 55 MPa (where $M_\infty = 7$ and $\alpha_e = 0$). The beginning of transition corresponds to the same Reynolds number of 3 million, at $M_\infty = 7$. Figs. 5.9 through 5.12 show that Re_{tr} is slightly lower, between 2 and 3 million at $M_\infty \approx 5$ (where $h_0 > 11\ MJ/kg$ and $\alpha_e \neq 0$). This difference seems *a priori* due to a Mach number effect. A compilation of Re_{tr} vs. h_0 is shown in Fig. 5.5. Fig. 5.6 taken from DiCristina (1970) shows the trend of Re_{tr} vs. M_e. Re_{tr} increases with M_e.

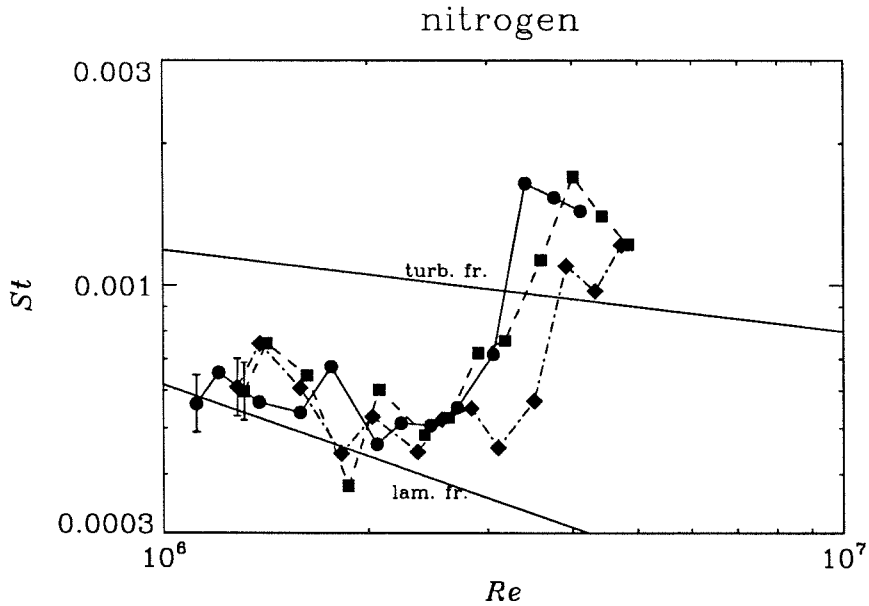

FIG. 5.3. Normalized heat transfer measurements of three different shots in T5. Squares (run 542): h_0 = 3.5 MJ/kg and p_0 = 10.5 MPa; circles (run 546): h_0 = 5.8 MJ/kg and p_0 = 16 MPa; diamonds (run 361): h_0 = 6.0 MJ/kg and p_0 = 19 MPa. The theoretical predictions for run 546 are also plotted.

This 'Mach number effect' is further evidenced by helium runs for which no real-gas effects are expected. Because of its higher ratio of specific heats γ (=1.67), the nozzle produces $M_\infty = 11.9$. Thus Re_{tr} can be as high as at least 8 million as seen in Fig. 5.7. It was observed that in these runs the location of the transition x_{tr} was approximately the same at $x = 50$ cm. This phenomenon is the result of a strong compression wave focusing on that location and is not a 'unit-Reynolds-number effect'. This problem results from using the contoured-wall nozzle far from its design conditions. The cone was not moved forward

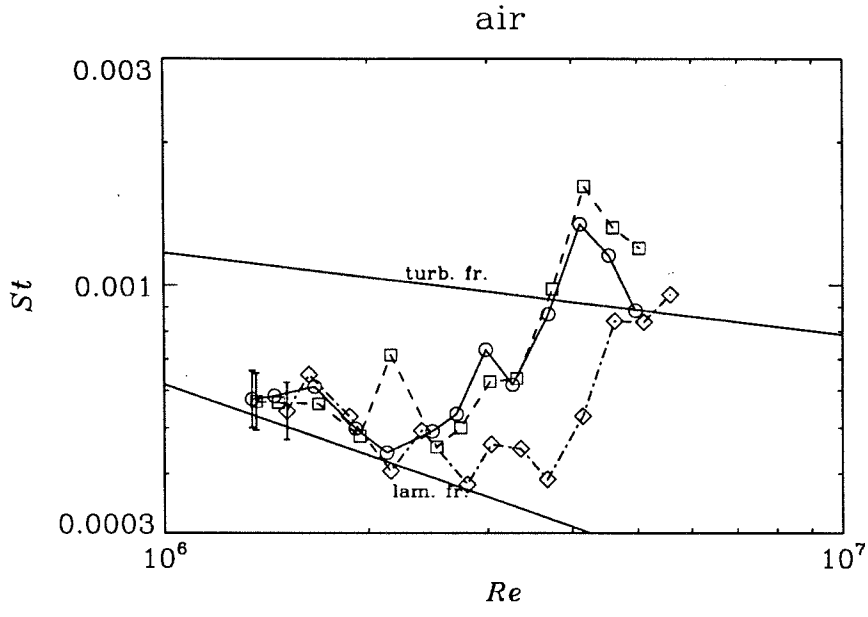

FIG. 5.4. Normalized heat transfer measurements of three different shots in T5. Squares (run 543): h_0 = 3.6 MJ/kg and p_0 = 11 MPa; circles (run 547): h_0 = 5.6 MJ/kg and p_0 = 16 MPa; diamonds (run 362): h_0 = 6.0 MJ/kg and p_0 = 19 MPa. The theoretical predictions for run 547 are also plotted.

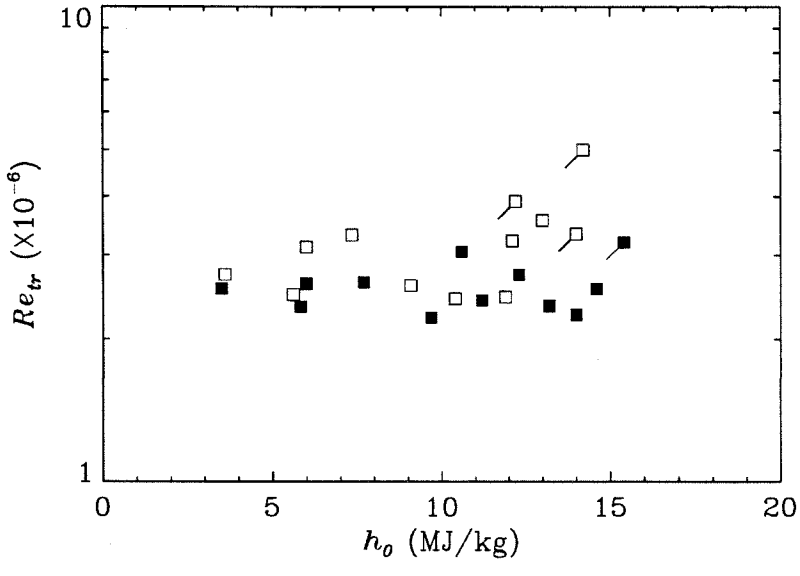

FIG. 5.5. Compilation of Re_{tr} versus h_0 for all the cases presented in this chapter for air (open symbols) and nitrogen (solid symbols). In some cases, the symbol is flagged because the corresponding boundary layer has not yet reached detectable transition. This symbol corresponds, therefore, to the last datum of the set. Nevertheless, it can be seen that the data are generally higher in the case of air.

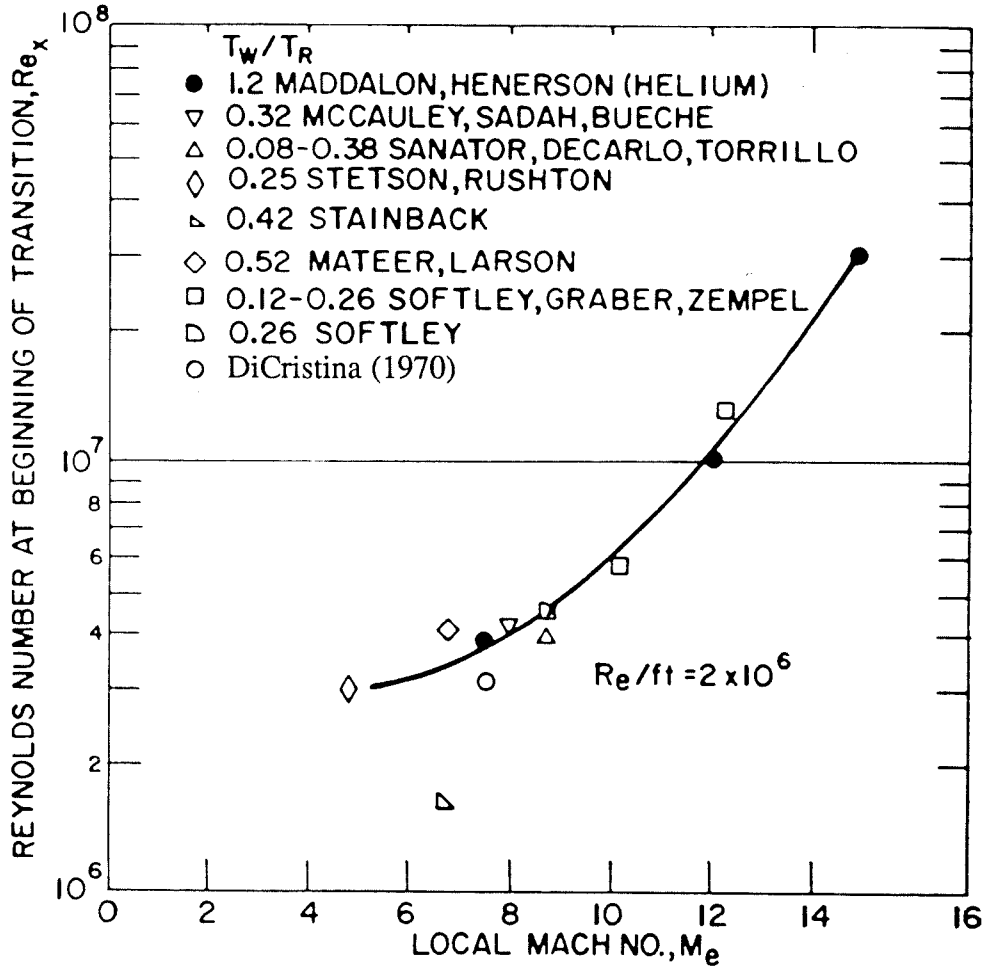

FIG. 5.6. Compilation of data showing Re_{tr} versus M_e obtained in some other facilities where the corresponding $h_0 < 1$ MJ/kg. The data fall approximately on the same curve regardless of T_W/T_R ($\equiv T_w/T_r$). Taken from DiCristina (1970).

or backward with respect to the nozzle to test this hypothesis. However, the presence of the compression wave at the nozzle exit has been comfirmed in experiments with argon by Rousset and Adam (1993).

In a given facility and at given ambient noise conditions, the transition Reynolds number may be expected to be related to the following dimensionless variables.

$$Re_{tr} = Re_{tr}(M, \gamma, Pr, \frac{T_w}{T_{aw}}, \frac{h_0}{D}, \Omega), \tag{5.1}$$

where Ω is a dimensionless reaction rate parameter (which could be the dimensionless form of $\mathcal{K}$, defined in Chapter 2), assuming there is only one D and only one Ω. For example, Demetriades (1977), having studied the wall cooling effect obtains, for $T_w/T_e = 4.2$ and

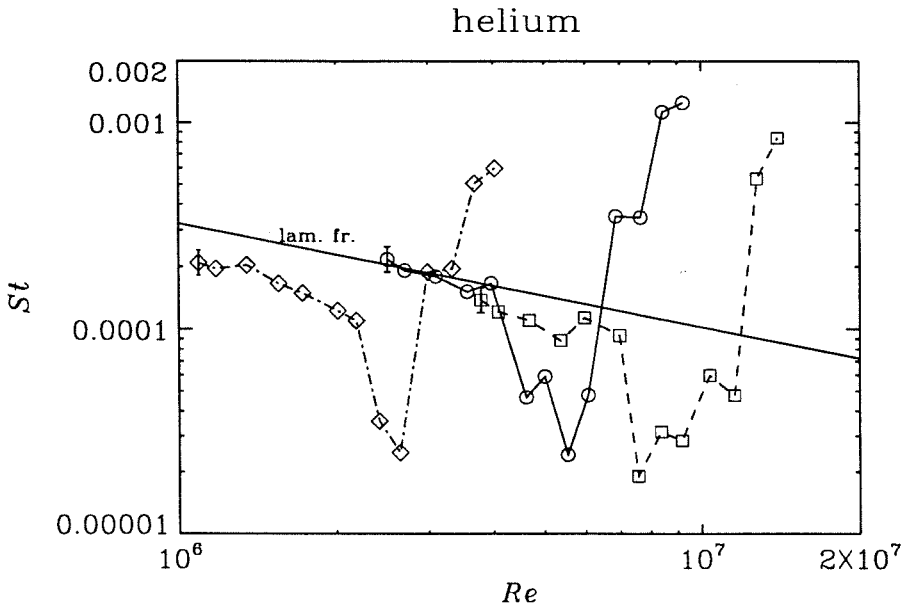

FIG. 5.7. Normalized heat transfer measurements of three different shots in T5. Squares (run 550): h_0 = 26 MJ/kg and p_0 = 55 MPa; circles (run 551): h_0 = 34 MJ/kg and p_0 = 50 MPa; diamonds (run 552): h_0 = 58 MJ/kg and p_0 = 40 MPa. The solid line is the theoretical prediction for a helium flow at h_0 = 26 MJ/kg and p_0 = 55 MPa (run 550). The three distributions have a feature indicative of a shock/boundary layer interaction.

8.4, Re_{tr} = 3.3 × 10^6 and 5.0 × 10^6, respectively. These data and those in Fig. 5.6 will be used for comparison purposes[1].

In laminar boundary layers of perfect gases, it is well known that the separate dependence of dimensionless quantities on M, γ, Pr and T_w/T_{aw} disappears if the physical parameters are evaluated at conditions corresponding to the reference temperature T^* introduced by Eckert (1955)[2]. This concept worked very well for the laminar regime on which a dimensionless correction factor, to account for compressibility, was based (Re_{tr} corresponds to the end of the laminar regime). Recall that T^* is a reference temperature obtained

---

[1] Not enough information is provided by Martellucci and Laganelli (1974) to deduce T_w/T_e. But Demetriades (1977) used the same wind tunnel and the same model.

[2] These conditions should correspond rather to a reference enthalpy h^*. For simplicity, we assume that the physical parameters ρ and μ based on T^* are good approximations.

from

$$\frac{T^*}{T_e} = 0.5 + 0.039M_e^2 + 0.5\frac{T_w}{T_e}. \tag{2.8}$$

In an attempt to separate out the real-gas effects, *i.e.*, the influence of h_0/D and of Ω, we renormalized the results for the transition Reynolds number by evaluating it at T^* to give Re^*_{tr}.

$$Re^* = \frac{\rho^* u_e x}{\mu^*}. \tag{5.2}$$

This procedure led to values that are plotted in Fig. 5.8. They are plotted against h_0 instead of, say, h_0/D because it is difficult to find a dimensionless parameter (involving h_0) for a gas mixture such as air. Fig. 5.8 also shows the data displayed in Fig. 5.5 and in Fig. 5.6 based on this new renormalization. As may be seen, the data collapse on two lines: one for air and one for nitrogen. The difference between these two lines is considered next.

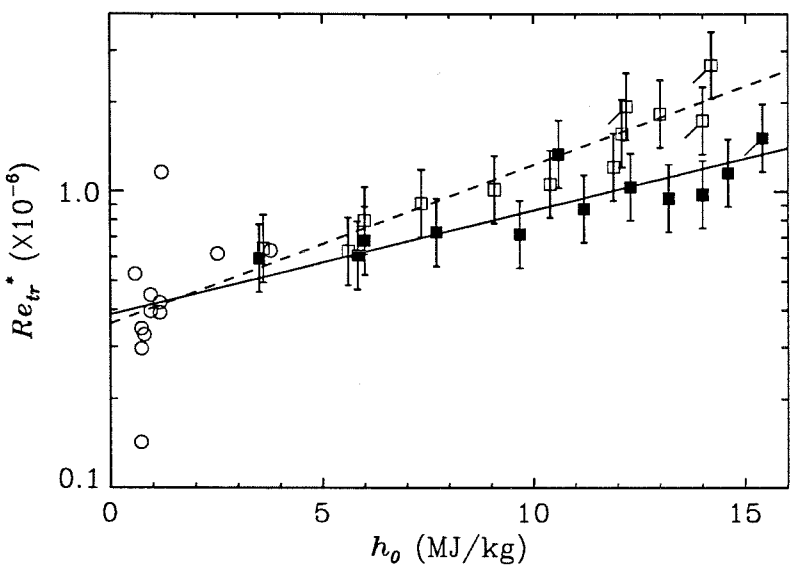

FIG. 5.8. Renormalized data showing Re^*_{tr} versus h_0. The data from Fig. 5.5 are shown as square symbols (open for air and solid for nitrogen). The error bar shown is an approximation of the accuracy in determining Re_{tr} from the previous plots. The data shown as open circles come from Fig. 5.6 (the helium data points are not included however). Demetriades' data are also included as open circles. The two lines are least-squares-fit approximations of either the open or the solid symbols.

5.2 Real-gas effects

As we increase the specific enthalpy while keeping the stagnation pressure constant, the boundary layer becomes turbulent at a higher Reynolds number. This is evidenced in Fig. 5.9 and Fig. 5.10 for p_0 = 55 MPa and in Fig. 5.12 for p_0 = 85 MPa. Since oxygen dissociates at a lower temperature than nitrogen, real-gas effects are expected to occur at lower h_0 in air, *cf.*, Table 1, p. 32. As may be seen by comparing Figs. 5.9, 5.10, 5.11 and 5.12, in this case, they stabilize the boundary layer, since the nitrogen flow is transitional while the air flow is laminar for the same specific enthalpy and Re. Note also that Re_{tr} is consistently lower in the case of nitrogen at around 2.5 million as shown in Fig. 5.5 and that there is no unit Reynolds number dependence as Re_{tr} is the same in both cases where Re/m is different depending on p_0.

The stabilizing influence of the real-gas effects are further evidenced by carbon dioxide runs. This gas absorbs a large amount of energy in vibration at relatively low temperature and is easier to dissociate than the others, so that real-gas effects become evident at even lower enthalpy. Fig. 5.13 shows that the Reynolds number at the beginning of transition is higher at 4.0 million, with M_∞ = 4.5 (slightly lower than that of air and nitrogen runs). This transition Reynolds number is not correlated with h_0, but its renormalized value seems to be correlated, as shown in Fig. 5.14. The data for helium and carbon dioxide are plotted in Fig. 5.14 repeating Fig. 5.8 on a larger scale. It can be observed that Re^*_{tr} is roughly 0.4 million for either gases with $h_0 < 1$ MJ/kg, whereas it increases with stagnation enthalpy for gases that exhibit dissociative real-gas effects. The slope of Re^*_{tr} vs. h_0 is steeper for gases whose activation energy is lower.

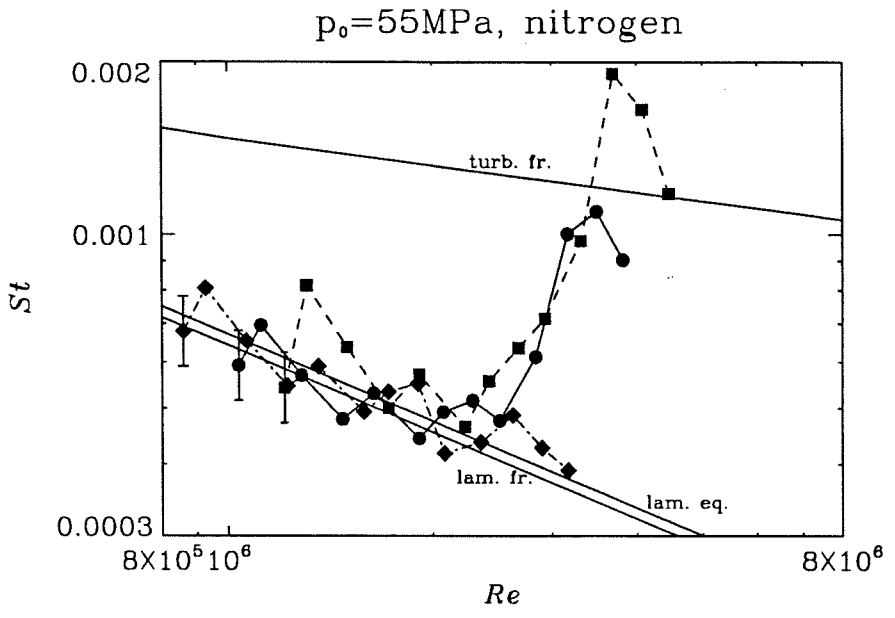

FIG. 5.9. Normalized heat transfer measurements of three different shots in T5 at p_0 = 55 MPa. Squares (run 533): h_0 = 11.2 MJ/kg; circles (run 536): h_0 = 14.0 MJ/kg; diamonds (run 535): h_0 = 15.4 MJ/kg. The theoretical predictions for run 536 are also plotted.

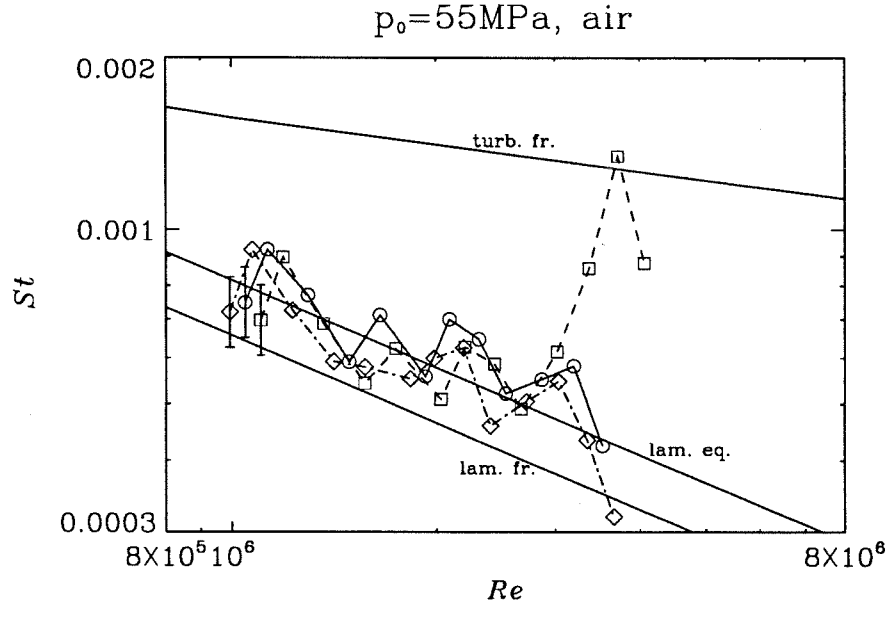

FIG. 5.10. Normalized heat transfer measurements of three different shots in T5 at p_0 = 55 MPa. Squares (run 554): h_0 = 11.9 MJ/kg; circles (run 553): h_0 = 12.2 MJ/kg; diamonds (run 537): h_0 = 14.0 MJ/kg. The theoretical predictions for run 553 are also plotted.

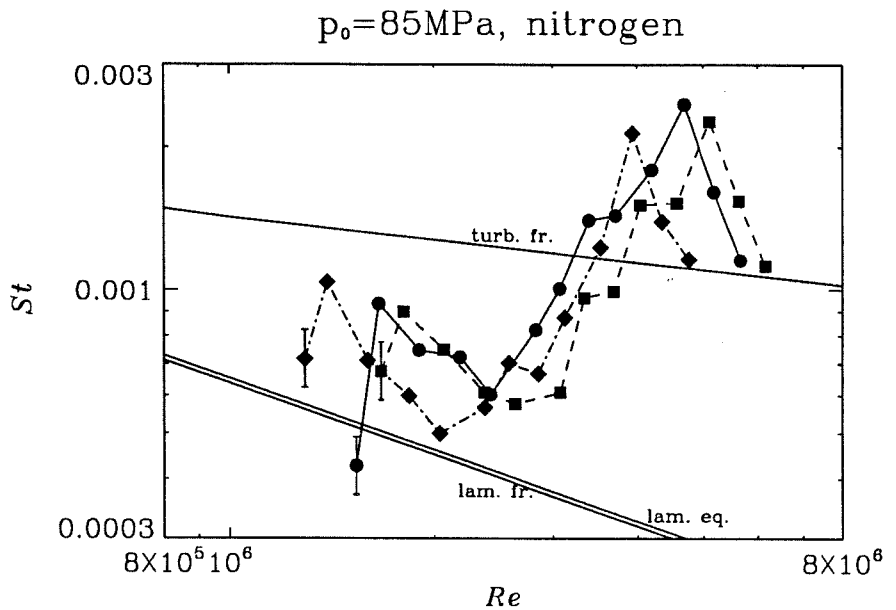

FIG. 5.11. Normalized heat transfer measurements of three different shots in T5 at p_0 = 85 MPa. Squares (run 561): h_0 = 12.3 MJ/kg; circles (run 563): h_0 = 13.2 MJ/kg; diamonds (run 565): h_0 = 14.6 MJ/kg. The theoretical predictions for run 563 are also plotted.

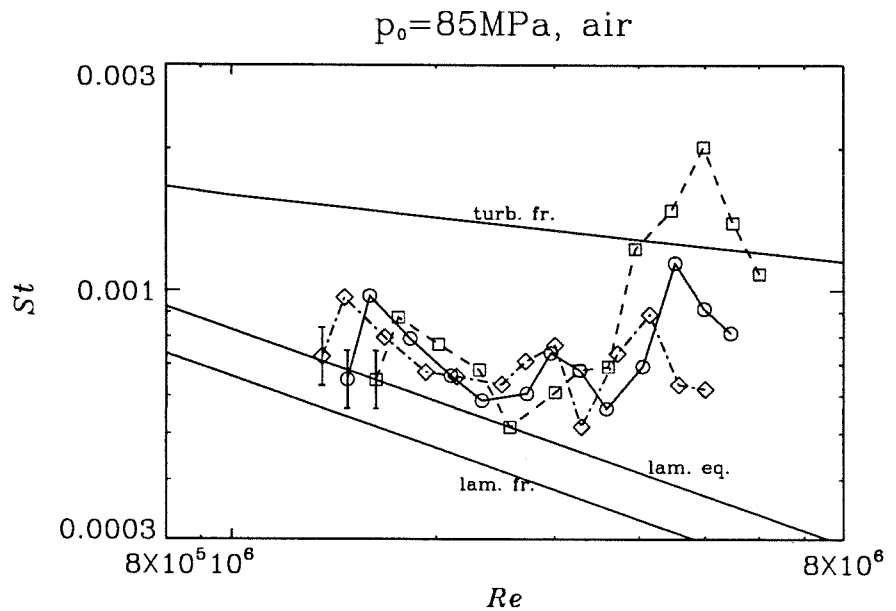

FIG. 5.12. Normalized heat transfer measurements of three different shots at p_0 = 85 MPa. Squares (run 562): h_0 = 12.1 MJ/kg; circles (run 564): h_0 = 13.0 MJ/kg; diamonds (run 566): h_0 = 14.2 MJ/kg. The theoretical predictions for run 564 are also plotted.

Conclusions made by comparing data from different facilities are only speculative in nature, as the transition process might not be the same according to Stetson (1993). An instability mode will characterize the transition process if its associated frequency is part of the frequency spectrum of the external perturbations. If it is, the instability associated with this mode will grow and dominate the transition process. However, regardless of the data obtained elsewhere, the conclusions obtained in this project concerning real-gas effects are still valid as behavior of different gases are being compared (obviously, in Fig. 5.14, more data are needed for the cases of helium and carbon dioxide).

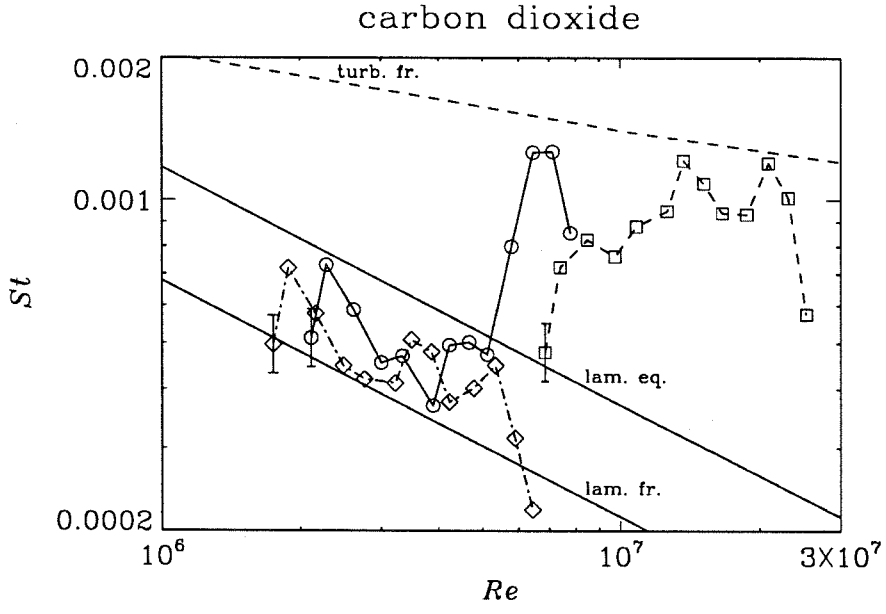

FIG. 5.13. Normalized heat transfer measurements of three different shots in T5. Squares (run 569): h_0 = 3.6 MJ/kg and p_0 = 55 MPa; circles (run 573): h_0 = 5.9 MJ/kg and p_0 = 55 MPa; diamonds (run 570): h_0 = 8.3 MJ/kg and p_0 = 55 MPa. The theoretical predictions for these carbon dioxide runs are also plotted. ——— : frozen flow, h_0 = 8.3 MJ/kg and p_0 = 55 MPa (run 570). - - - - - - - - : frozen flow, h_0 = 3.6 MJ/kg and p_0 = 55 MPa (run 569).

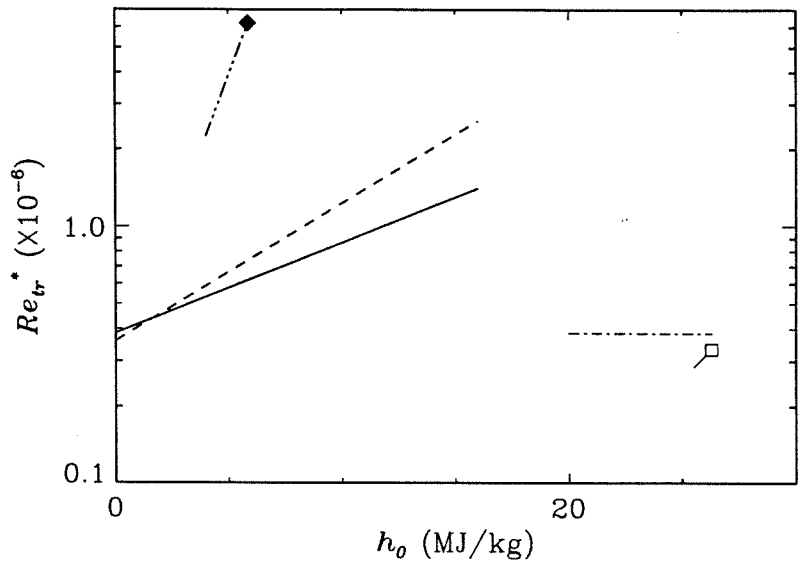

FIG. 5.14. Same plot as shown in Fig. 5.8 on a larger scale but without its symbols. The solid diamond symbol corresponds to the carbon dioxide run that is shown in Fig. 5.13 as open diamonds. The flagged open square symbol corresponds to Re_{tr} of the helium run represented by open squares in Fig. 5.7. This symbol is flagged to recall that this is not the actual Re_{tr} which could be higher if no shock wave were to impinge on the model surface.

5.3 Time evolution of the temperature traces

Fig. 5.15 presents the time evolution of the fifteen thermocouple signals for a run in which transition occurred[3]. The signal-to-noise ratio is not as high as in the laminar regime and the signal can be averaged over a period smaller than one millisecond. From two time traces, it is theoretically possible to obtain the speed of flow features convecting past the surface of the body (such as a shock wave, a turbulent burst or a travelling wave). However, no meaningful information can be extracted from the auto-correlations or cross-correlations of any of these signals. This problem may be due to one of the two following reasons: The size of the gauges is probably too large compared to the size of a typical eddy and/or the

[3] As seen in the results of this typical run, channel 3 and 5 were not working sometimes because the center lead of the gauges was eventually broken, thus creating an open circuit. Consequently, although their signals were processed like the other ones, no time-averaging was performed and only the values of the heat transfer rate of the remaining thirteen gauges are presented in the St vs. Re plots.

gauges are not positioned behind each other (this was done on purpose in case the first one would influence the others).

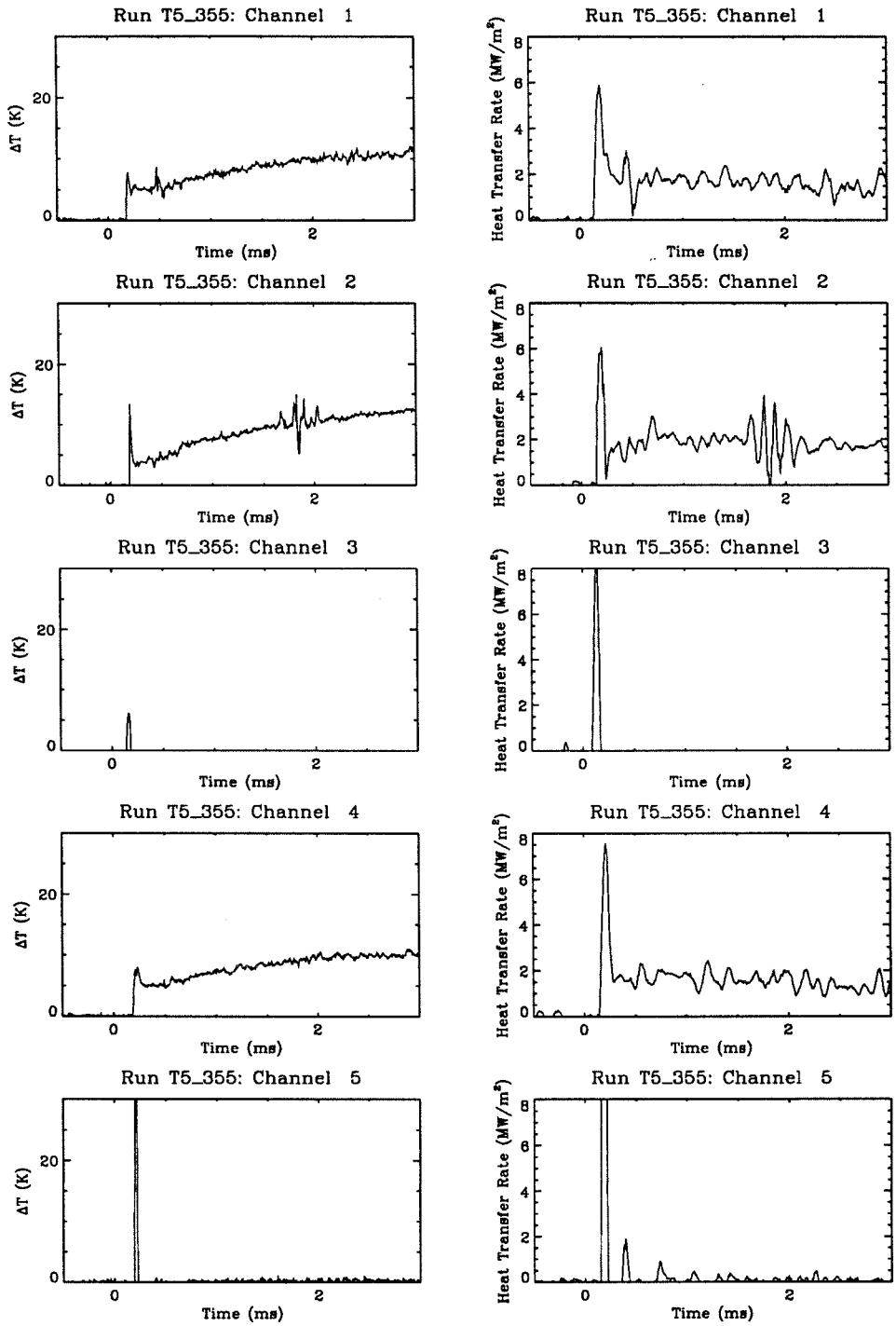

FIG. 5.15a. Typical time traces of the thermocouples. On the left are the voltage signals after conversion to temperature units and on the right are the results of the process converting them to heat tranfer rate time signals. The conditions for this particular shot were h_0 = 11 MJ/kg and p_0 = 60 MPa, pure nitrogen (refer to run 534, Table 2). Channel 3 and 5 were not working sometimes because the center lead of the gauges was eventually broken, thus creating an open circuit.

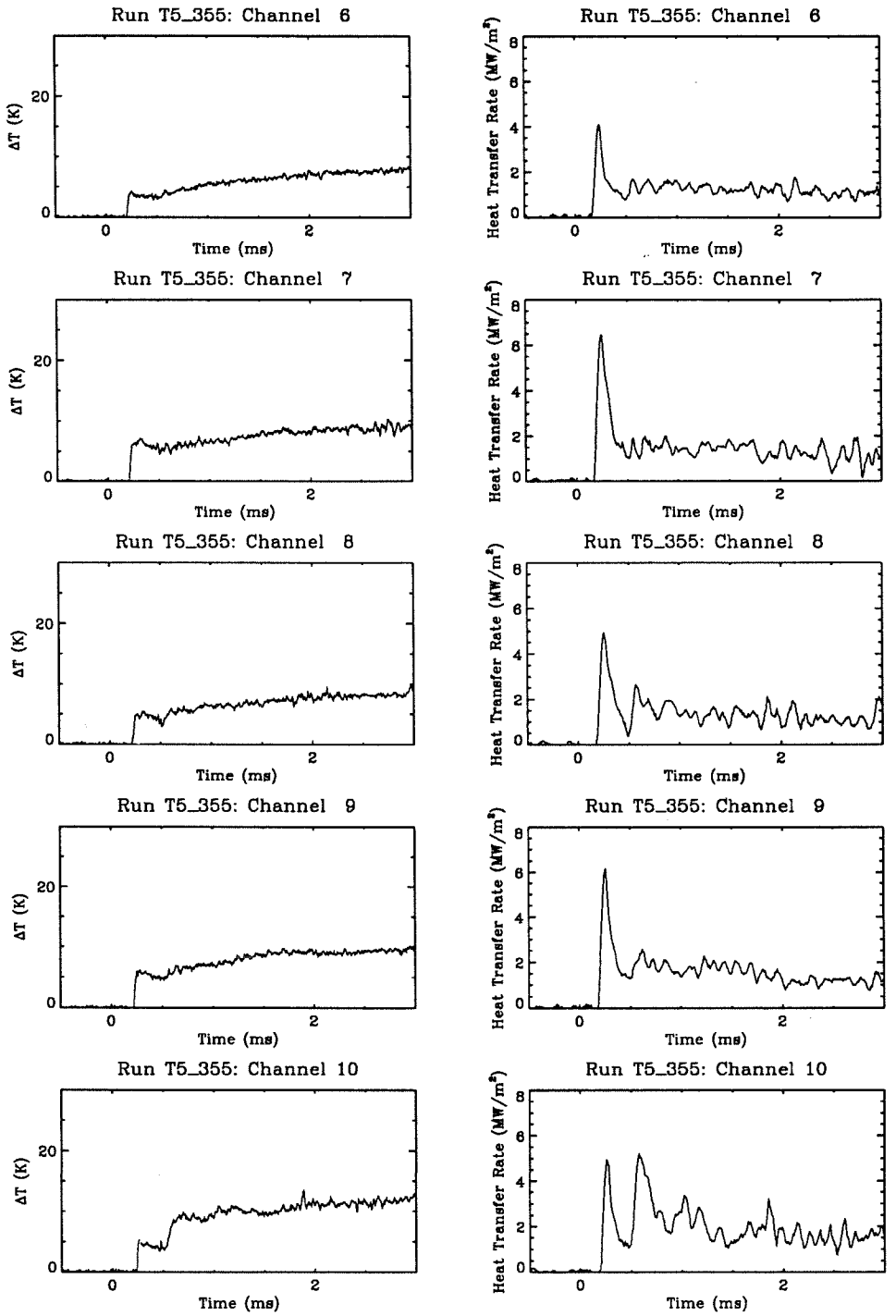

FIG. 5.15b. Continued. Typical time traces of the thermocouples. On the left are the voltage signals after conversion to temperature units and on the right are the results of the process converting them to heat tranfer rate time signals. The conditions for this particular shot were h_0 = 11 MJ/kg and p_0 = 60 MPa, pure nitrogen (refer to run 534, Table 2).

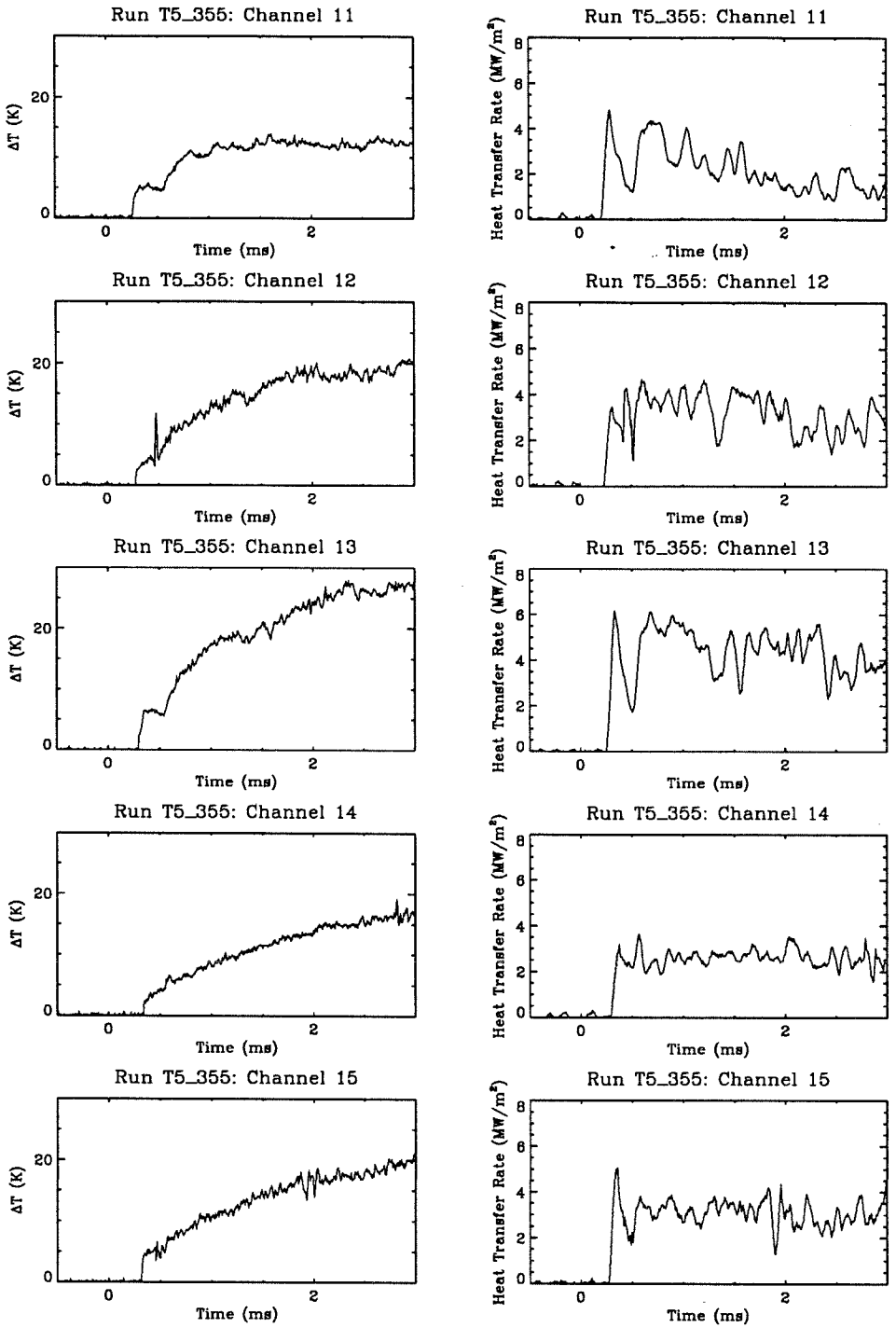

FIG. 5.15c. Continued. Typical time traces of the thermocouples. On the left are the voltage signals after conversion to temperature units and on the right are the results of the process converting them to heat tranfer rate time signals. The conditions for this particular shot were h_0 = 11 MJ/kg and p_0 = 60 MPa, pure nitrogen (refer to run 534, Table 2).

5.4 Flow visualization

In Figs. 5.17 through 5.23 photographs of transitional boundary layers are shown. They clearly show waves in the laminar part of the flow before it becomes turbulent. In Fig. 5.17, these waves appear most distinctly and their wavelength is on the order of 1.5 cm. If we use this value to divide half (say) of the value of the free stream velocity u_e (=4,300 m/s), we obtain a frequency of 150 kHz. This is the frequency a laboratory fixed observer measures. Extrapolating from the experimentally derived stability diagram published by Stetson (1988) and shown in Fig. 5.16, this frequency corresponds approximately to the Tollmien-Schlichting mode frequency. A comparison was also made with the calculation of Mack (1986). The frequency of the second mode would be of order 1 MHz or more for this particular flow condition. The second mode would be observed as periodic density fluctuations if it were present, *e.g.*, see Demetriades (1974). But as mentioned earlier, the differential interferometry technique (or the less sophisticated shadowgraphy technique) is not sensitive enough to detect it. Therefore it cannot be proven with certainty that the second mode is not present by flow visualization. However, looking from left to right, we observe initially the linear first mode of instability. The picture shows that after a few oscillations, the flow instability switches quickly to a nonlinear mode. In Fig. 5.17, the dark streak corresponds the location where the local temperature is high enough to cause the dissociation of the salt crystals. The source light is either highly absorbed or deflected, causing this dark streak on the film. Sodium atoms are presumed absent between the streak and the wall, thus having no effect on the source light.

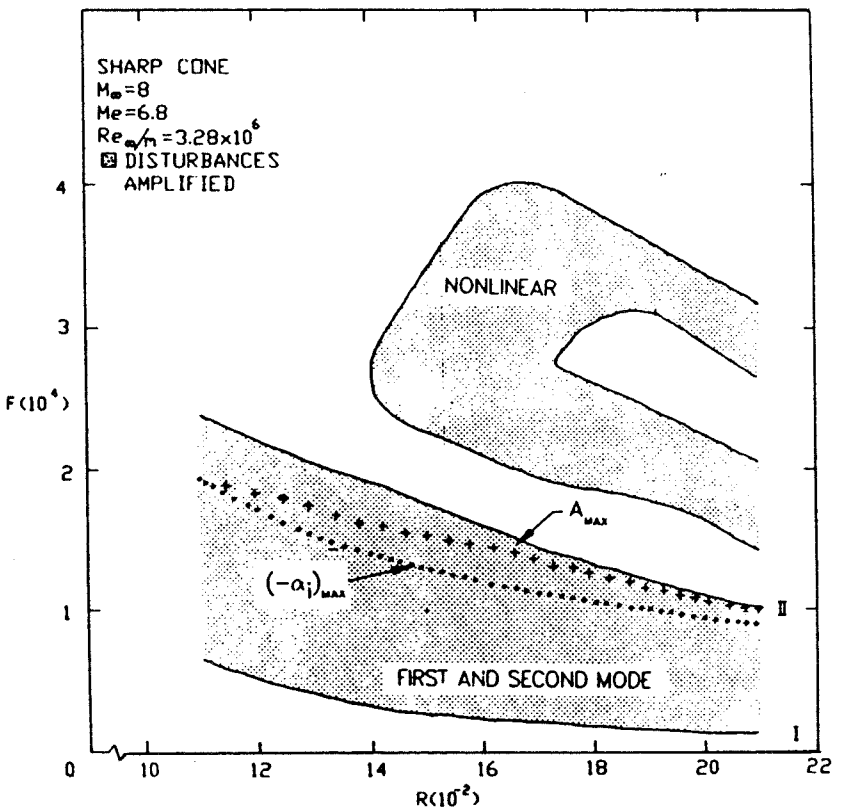

FIG. 5.16. Experimentally derived stability diagram obtained by Stetson (1988). F is a dimensionless frequency ($\equiv 2\pi f/(u_e^2\rho_e/\mu_e)$) and $R = \sqrt{Re}$.

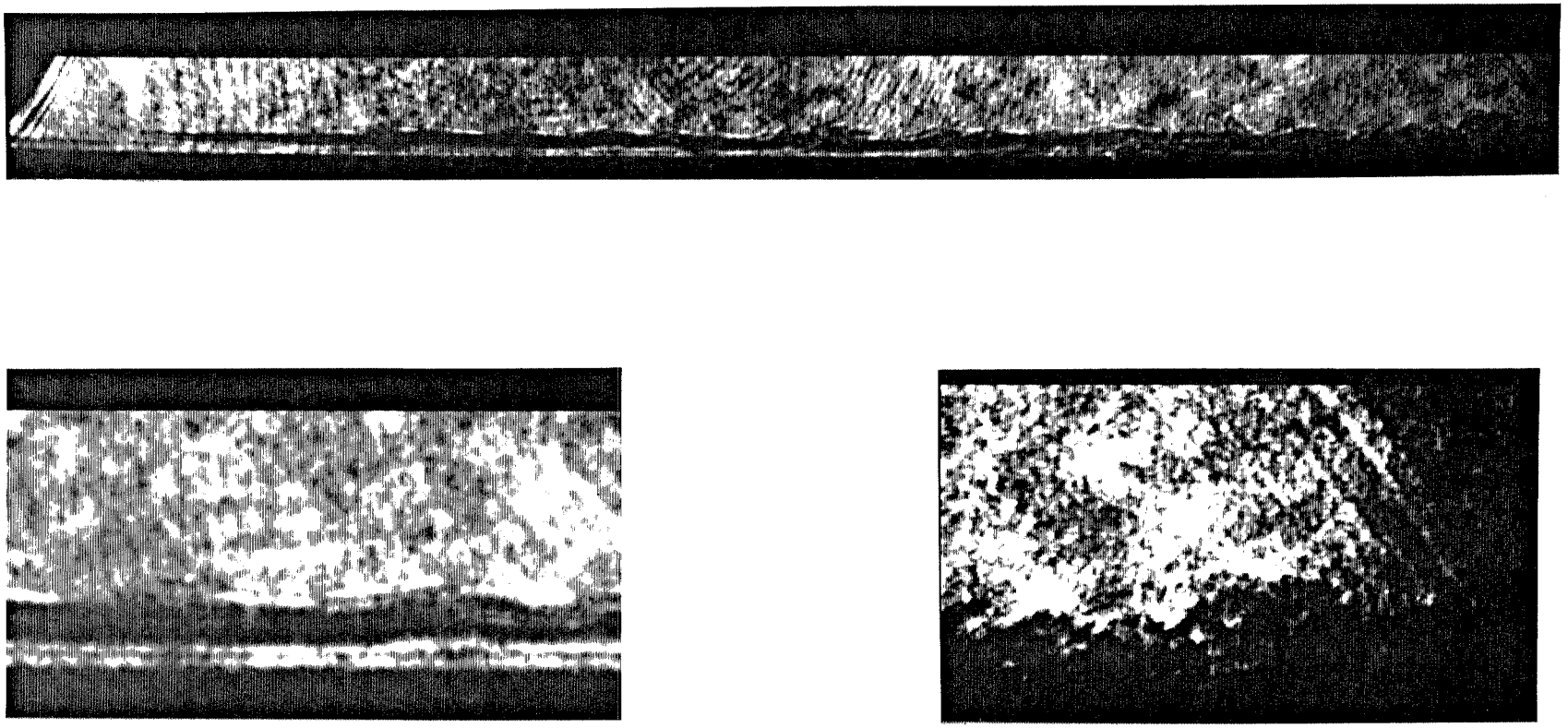

FIG. 5.17. Flow of nitrogen at h_0 = 11 MJ/kg and p_0 = 60 MPa (run 360, refer to 534 in Table 2). This resonantly enhanced interferogram was taken 1 ms after the nozzle reservoir pressure rise. The picture shows the boundary layer on the top of the 5 deg. half-angle cone, starting on the left from x = 510 mm (corresponding to Re = 2.75 million) to x = 680 mm (Re = 3.77 million). The pictures below magnify portions of the one above three times (3×). A wave in the laminar part of the flow appears distinctly and its wavelength is on the order of 1.5 cm.

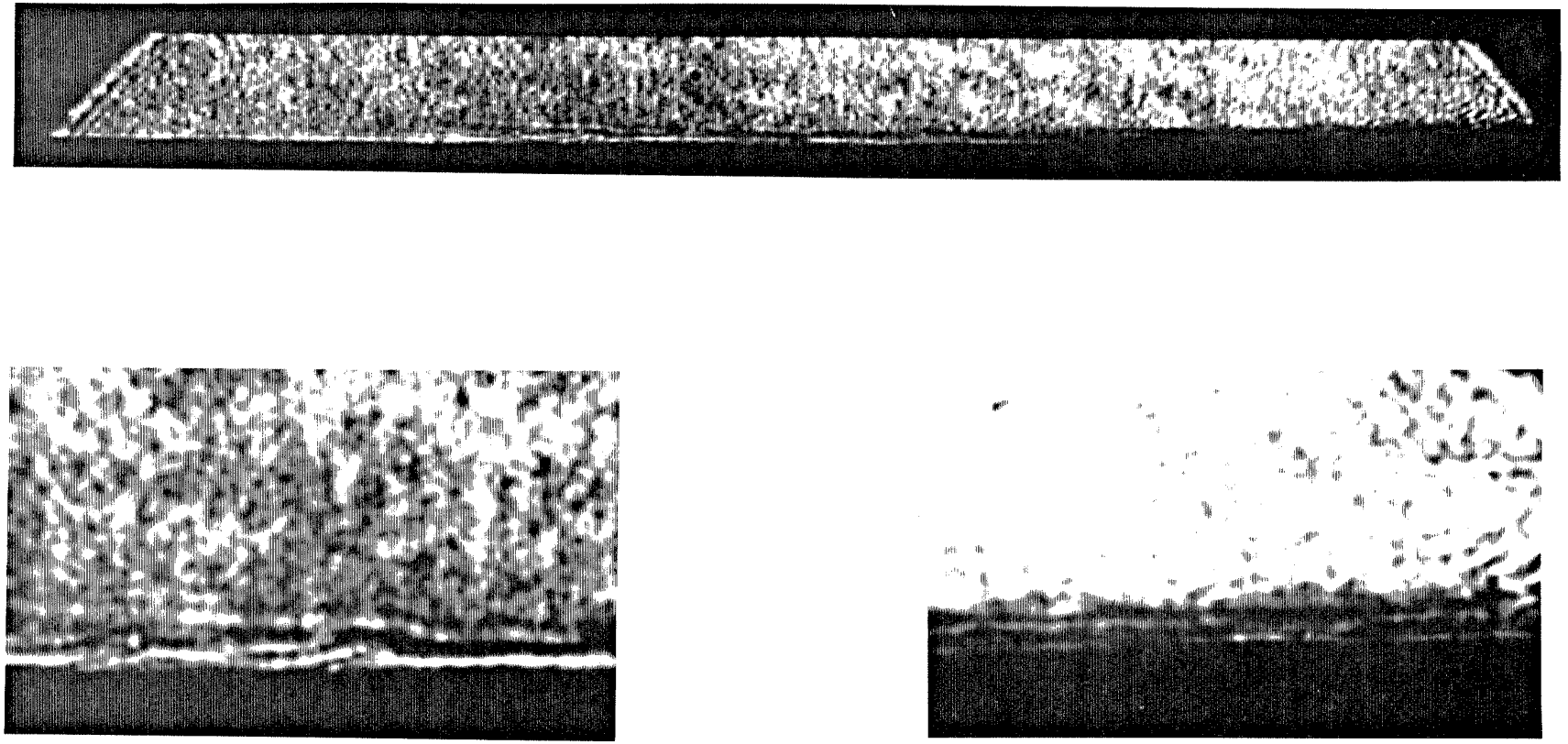

FIG. 5.18. Flow of nitrogen at h_0 = 14 MJ/kg and p_0 = 60 MPa (run 536). This resonantly enhanced shadowgraph was taken 1 ms after the nozzle reservoir pressure rise. The picture shows the boundary layer on the top of the 5 deg. half-angle cone, starting on the left from x = 539 mm (corresponding to Re = 2.31 million) to x = 710 mm (Re = 3.94 million). The pictures below magnify portions of the one above three times (3×). The laminar wave in this picture has a smaller amplitude than the one seen in Fig. 5.17, but its wavelength cannot be measured.

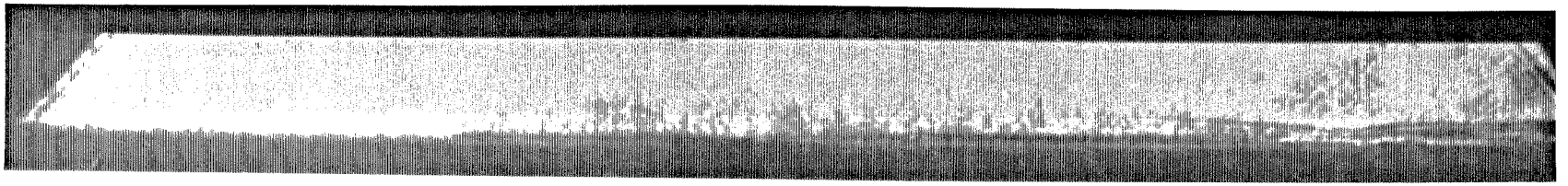

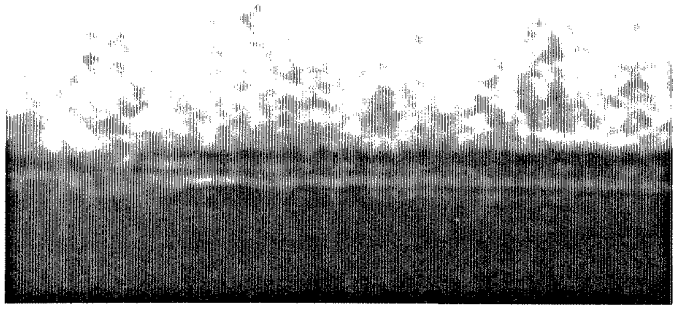

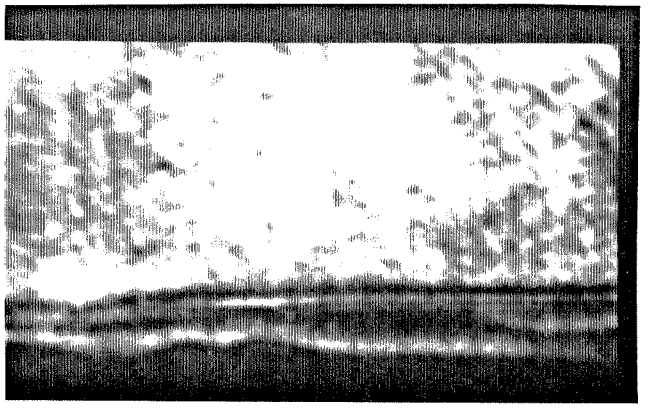

FIG. 5.19. Flow of nitrogen at h_0 = 14 MJ/kg and p_0 = 57 MPa (run 539, refer to 536 in Table 2). This resonantly enhanced shadowgraph was taken 1 ms after the nozzle reservoir pressure rise. The picture shows the boundary layer on the top of the 5 deg. half-angle cone, starting on the left from x = 539 mm (corresponding to Re = 2.14 million) to x = 710 mm (Re = 2.81 million). The pictures below magnify portions of the one above three times (3×). This picture corresponds to the transition onset of the boundary layer. A wave can be seen emerging on the far right.

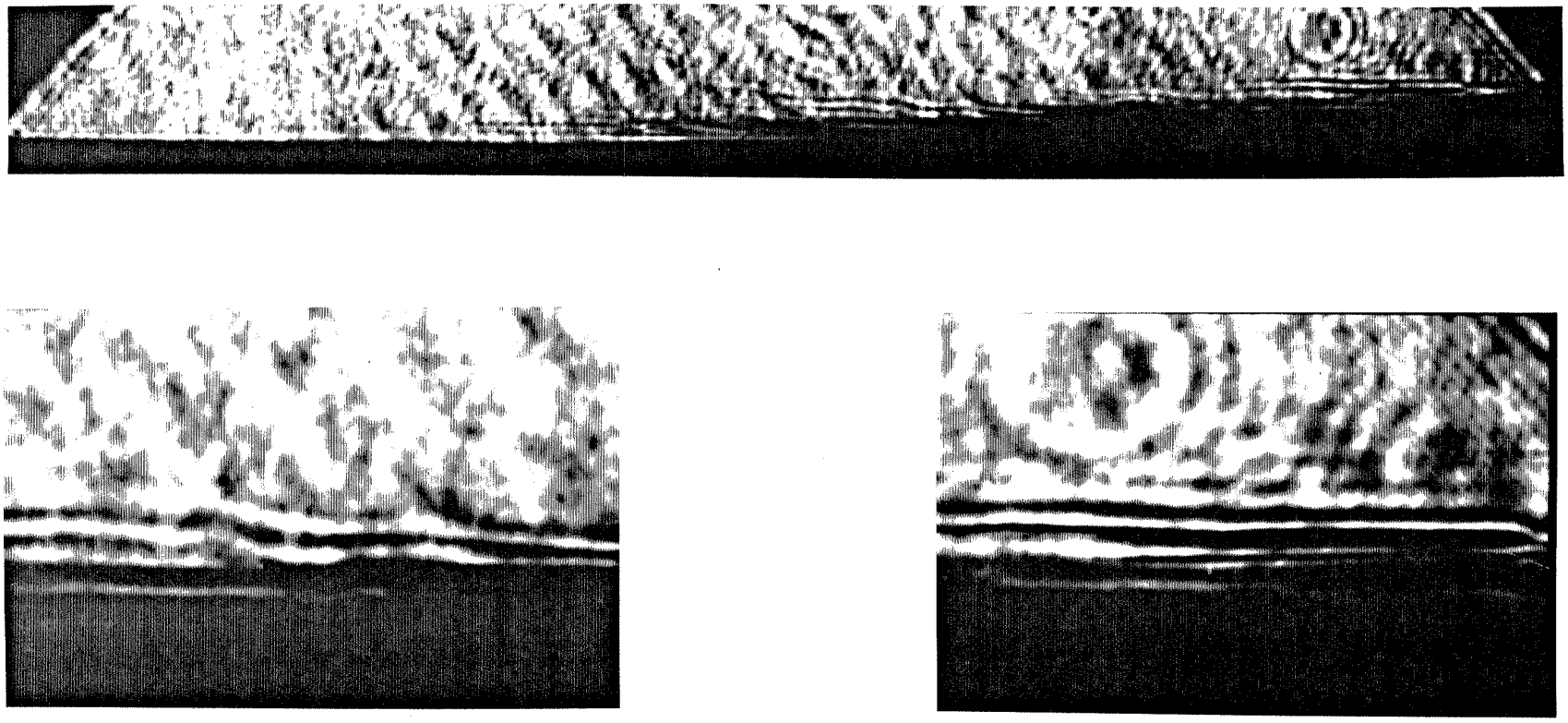

FIG. 5.20. Flow of nitrogen at h_0 = 12 MJ/kg and p_0 = 24 MPa (run 544). This resonantly enhanced shadowgraph was taken 1 ms after the nozzle reservoir pressure rise. The picture shows the boundary layer on the top of the 5 deg. half-angle cone, starting on the left from x = 539 mm (corresponding to Re = 1.14 million) to x = 710 mm (Re = 1.50 million). The pictures below magnify portions of the one above three times (3×). There is so much sodium in the lower part of the boundary layer that the source light is completely absorbed. The upper part appears to show interferences fringes due to the boundary layer containing sodium atoms. However, the waviness of these fringes is caused by laminar waves. The wavelength is difficult to determine probably because the waves are not axisymmetric.

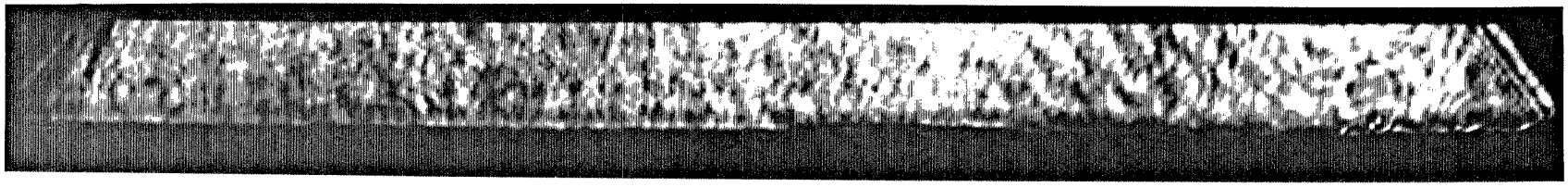

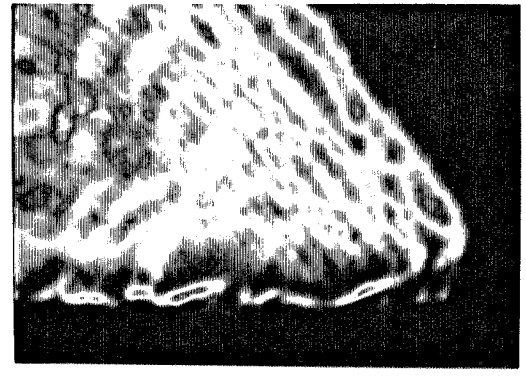

FIG. 5.21. Flow of air at h_0 = 12 MJ/kg and p_0 = 55 MPa (run 553). This resonantly enhanced shadowgraph was taken 1 ms after the nozzle reservoir pressure rise. The picture shows the boundary layer on the top of the 5 deg. half-angle cone, starting on the left from x = 539 mm (corresponding to Re = 2.34 million) to x = 710 mm (Re = 3.08 million). The pictures below magnify portions of the one above three times (3×) and they were enhanced according to 'scheme B', described in Fig. 3.15. A small turbulent burst can be seen on the far right. As there is probably no laminar wave preceding it, this suggests a high intensity bypass, *i.e.*, a transition process dominated only by nonlinear modes of instability.

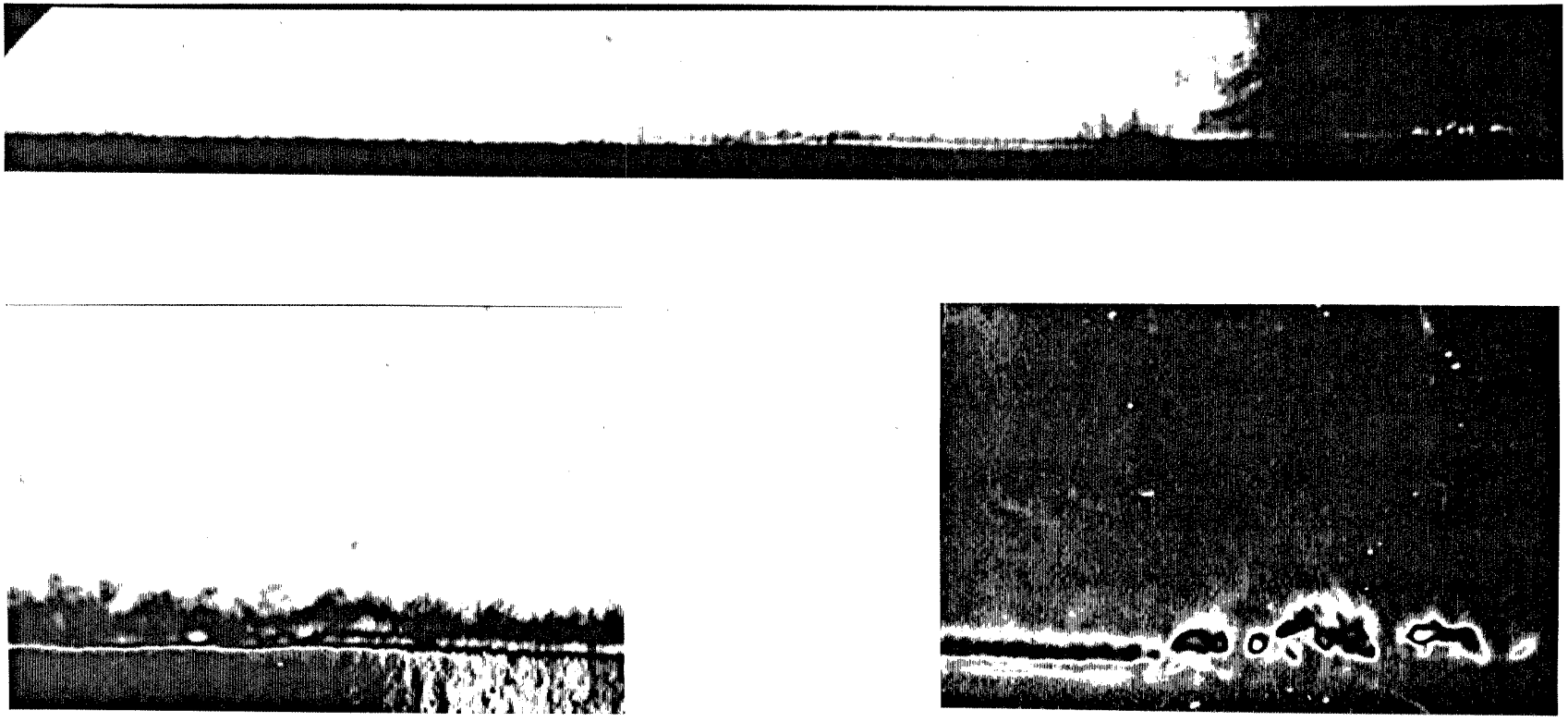

FIG. 5.22. Flow of air at h_0 = 10 MJ/kg and p_0 = 52 MPa (run 557, refer to 549 in Table 2). This resonantly enhanced shadowgraph was taken 1.13 ms after the nozzle reservoir pressure rise. The picture shows the boundary layer on the top of the 5 deg. half-angle cone, starting on the left from x = 539 mm (corresponding to Re = 2.83 million) to x = 710 mm (Re = 3.72 million). The pictures below magnify portions of the one above three times (3×) and they were enhanced according to 'scheme B', described in Fig. 3.15. This picture is very similar to the one in Fig. 5.21 except that it was taken slightly later.

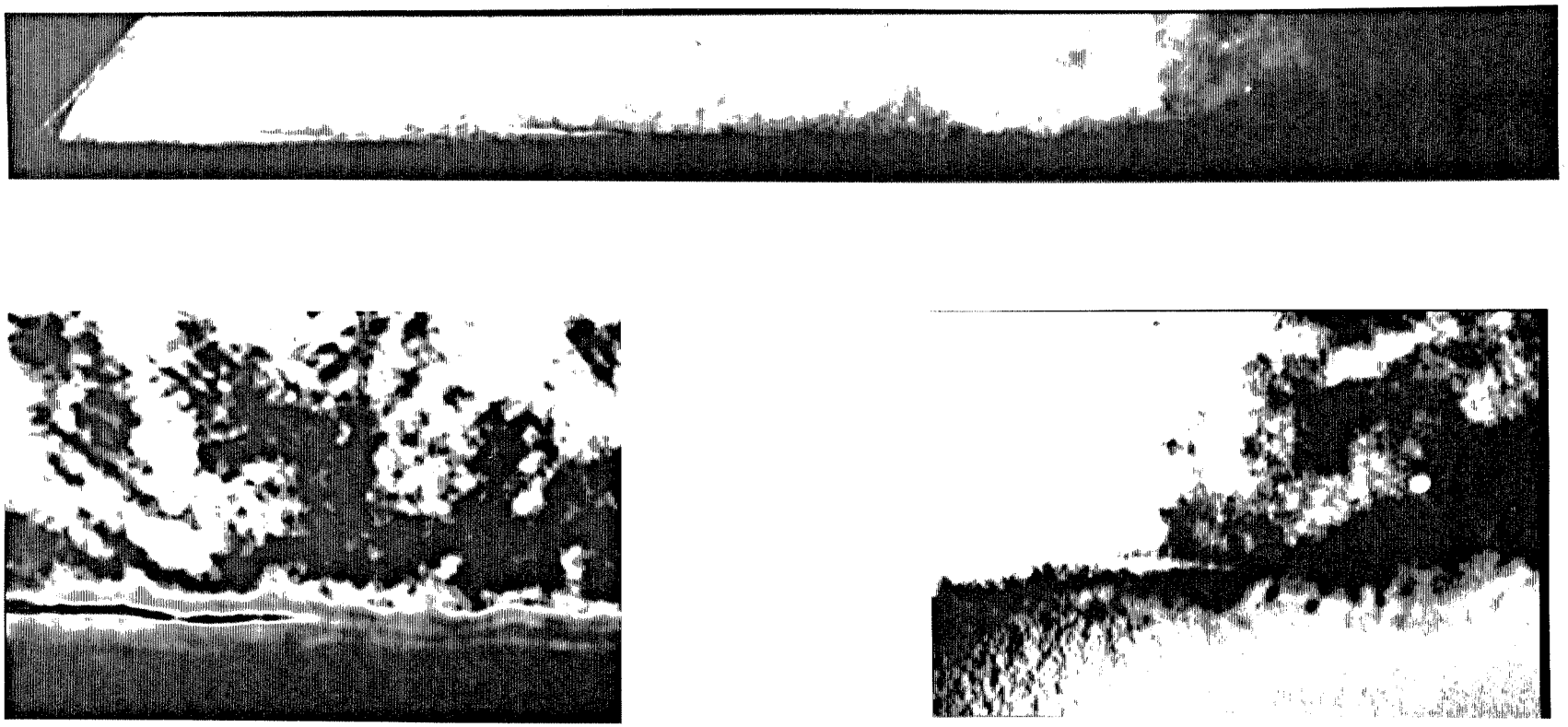

FIG. 5.23. Flow of air at h_0 = 11 MJ/kg and p_0 = 55 MPa (run 558, refer to 553 in Table 2). This resonantly enhanced shadowgraph was taken 0.88 ms after the nozzle reservoir pressure rise. The picture shows the boundary layer on the top of the 5 deg. half-angle cone, starting on the left from x = 539 mm (corresponding to Re = 2.79 million) to x = 710 mm (Re = 3.68 million). The pictures below magnify portions of the one above three times (3×) and they were enhanced according to 'scheme B', described in Fig. 3.15. A laminar wave can be seen in a short portion on the left of this picture. Nonlinear modes of instability quickly 'overrun' the TS wave.

5.5 Comparison with the linear stability theory results

As mentioned in the introduction, it was found numerically that the second mode is destabilized by real-gas effects whereas the TS mode was stabilized. The second mode would dominate the transition process if perturbations triggering it were strongly present in the incoming flow.

At such high frequency, it was not possible to detect the instabilities associated with the second mode with surface heat transfer rate measurements because the sampling frequency was set at only 200 kHz[4]. Incidentally, the data were also recorded at a higher sampling frequency at 500 kHz but the resulting data showed no new meaningful information (the time response of the thermocouple being of order 1 μs, it is not useful to sample the signal at a higher rate). The actual signal-to-noise ratio would probably prevent this information. As mentioned in the previous section, neither flow visualization method could provide information regarding the presence of a second-mode instability. The previous experimental results mentioned above indicate that the frequency of the most unstable mode (the second mode), at Mach number above 5, is of order 1 MHz at T5 conditions. No mechanical vibrations of such a high frequency are to be expected in the facility. The only source of important noise is likely to be the nozzle-wall boundary layer, and this also may not be in the right frequency range, since the nozzle-wall boundary layer is much thicker than the laminar boundary layer on the cone. Our observations indicate that if one linear mode of instability dominates the transition process at the conditions studied, it is the TS mode in the shock tunnel experiments. This observation is confirmed by the linear stability theory which also predicts that the TS mode is stabilized by real-gas effects as observed here.

According to Stetson's diagram (in Fig. 5.16), the nonlinear modes could be observed at Re starting at 2 million but a frequency as high as 1 MHz also. No observation, *i.e.*, nothing special such as a particular frequency, of these nonlinear modes was achieved in

[4] The second mode has never been detected by surface temperature measurement. It has been observed only by the Schlieren method of flow visualization and by hot-wire anemometry survey across the boundary layer, *e.g.*, Demetriades (1974).

this facility without the earlier presence of the TS mode.

5.6 Chapter summary

In this chapter, it was found by comparing runs with different test gases, that real-gas effects stabilize the boundary layer. The TS instability mode is present whereas the second mode cannot be proven to be active with the diagnostic techniques used. From a conclusion drawn from the linear stability theory, it can be argued that the second-mode instabilities are not present at all or are very weak in the present flow conditions.

In the continuous-flow facilities previous experimentalists used, there were sufficiently strong free-stream perturbations (acoustic in nature) to trigger and sustain the second linear mode instabilities. These researchers had to study these instabilities and could relate their hot-wire anemometry surveys to the existing linear stability theory. In a real flight situation, it is likely that these perturbations are not present. As noted by Stetson (1993), the transition process would therefore not be dominated by these higher order instability modes.

To summarize, it was found that Re_{tr} is sensitive to wall temperature, the free-stream Mach number, and especially the composition of the test gas. To isolate the chemical composition effect, x_{tr} was renormalized as Re^*_{tr}. The value of Re^*_{tr} is assumed approximately constant for perfect gases such as helium. As h_0 increases, Re^*_{tr} increases exponentially. This rate, given roughly by the slope of $log(Re^*_{tr})$ vs. h_0, is larger for air than for nitrogen and even more for carbon dioxide. This observation is interpreted as a real-gas effect because these test gases have a decreasing value of activation energy in this order. Flow visualization has revealed the presence in some cases of the Tollmien-Schlichting mode. This comes as no surprise as the anticipated value of the second-mode harmonic frequency is very high, of order 1 MHz. The first linear mode, when it is observable, is quickly 'overrun' by nonlinear modes and the boundary layer becomes turbulent. This regime is addressed in the next chapter.

CHAPTER 6

Experimental results - Turbulent regime

As in the laminar and transitional regime, the experimental results consisted of surface heat flux measurements and flow visualization pictures. At the turbulent regime, no real-gas effects are expected as the specific enthalpy is too low and as atomic species are absent from the free stream. First, comparison is made between heat transfer rate measurements and a semi-empirical prediction (incorporating a correction for compressibility by an approximation developed by Van Driest, 1956)). Second, pictures taken with the flow visualization technique described earlier show the turbulent boundary layer at typical conditions where either p_0 = 55 MPa or 85 MPa, and h_0 goes from 5 MJ/kg to 12 MJ/kg. In most of the pictures, structural patterns similar to those ordinarily found in incompressible turbulent boundary layers are evident.

6.1 Heat transfer measurements

Fig. 6.1 shows typical normalized heat flux data for air and nitrogen. The data are of the same order of magnitude as the prediction. An overprediction was obtained by He and Morgan (1989). The correlation obtained from White (1974) is $0.140\ ln^{-2}(0.031Re)$ (with Pr_t = 0.86) as plotted. Fig. 6.2 shows typical time traces. The signal-to-noise ratio is low because the specific enthalpy is also low. However, on a log-log plot, the scatter of the data ($St\ vs.Re$) does not appear too good. The rms error as defined in Chapter 2, p. 24, is of order 20%.

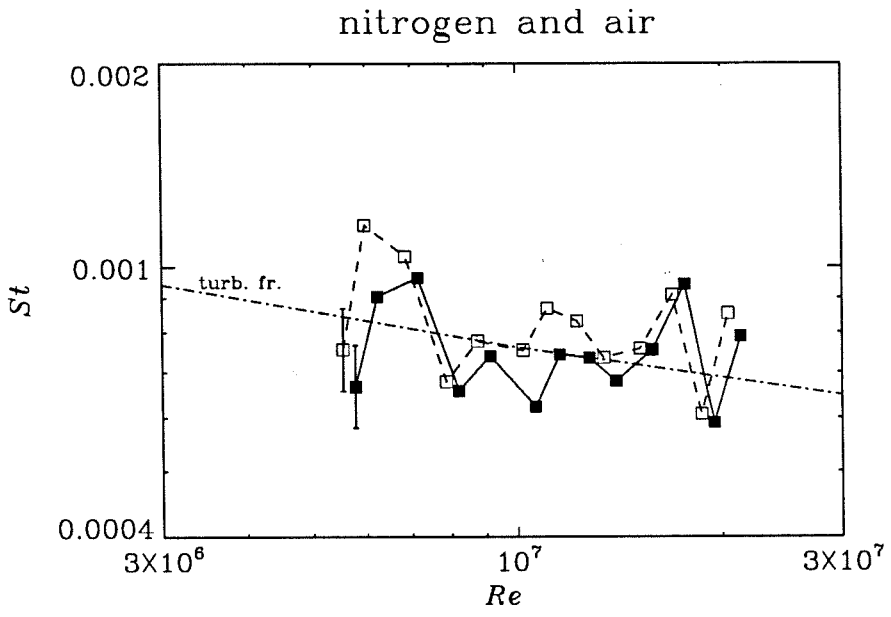

FIG. 6.1. Normalized heat transfer measurements of two different shots in T5. Solid symbols (run 349): h_0 = 3.5 MJ/kg and p_0 = 47 MPa; open symbols (run 336): h_0 = 3.4 MJ/kg and p_0 = 42 MPa. The theoretical prediction for these runs is also plotted for these conditions.

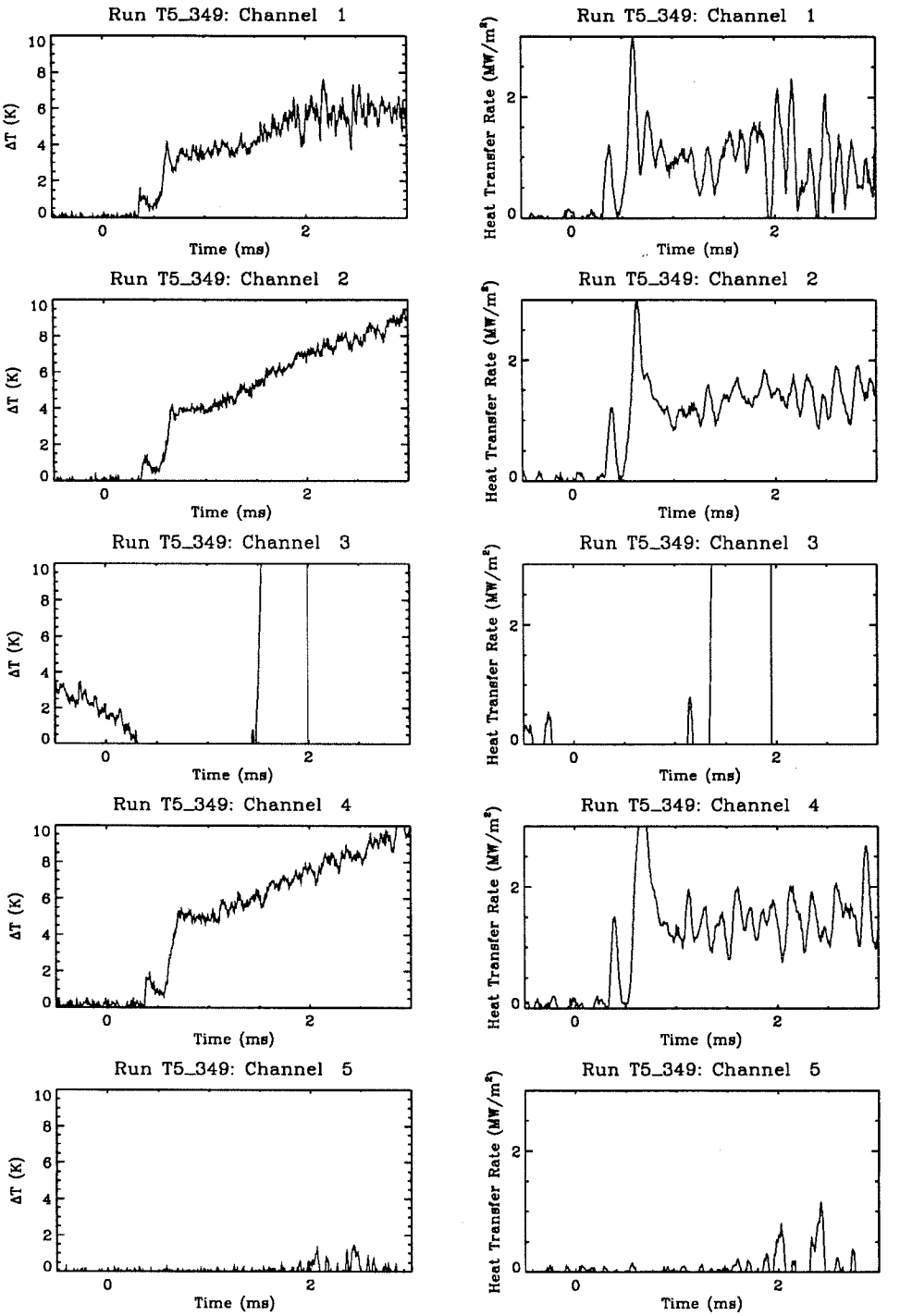

FIG. 6.2a. Typical time traces of the thermocouples. On the left are the voltage signals after conversion to temperature units and on the right are the results of the process converting them to heat tranfer rate time signals. The conditions for this particular shot were h_0 = 3.5 MJ/kg and p_0 = 47 MPa, pure nitrogen. Channel 3 and 5 were not working sometimes because the center lead of the gauges was eventually broken, thus creating an open circuit.

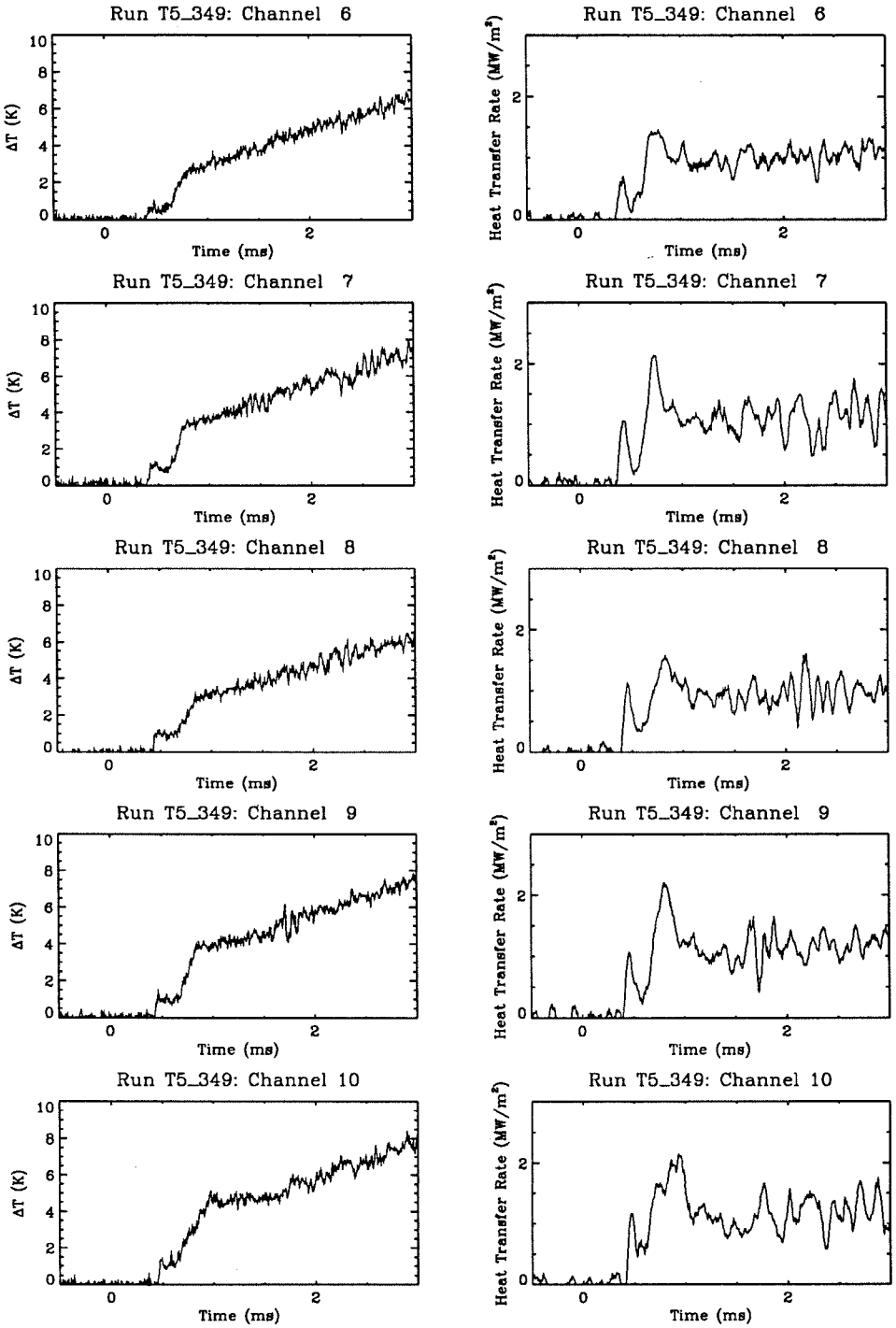

FIG. 6.2b. Continued. Typical time traces of the thermocouples. On the left are the voltage signals after conversion to temperature units and on the right are the results of the process converting them to heat tranfer rate time signals. The conditions for this particular shot were h_0 = 3.5 MJ/kg and p_0 = 47 MPa, pure nitrogen.

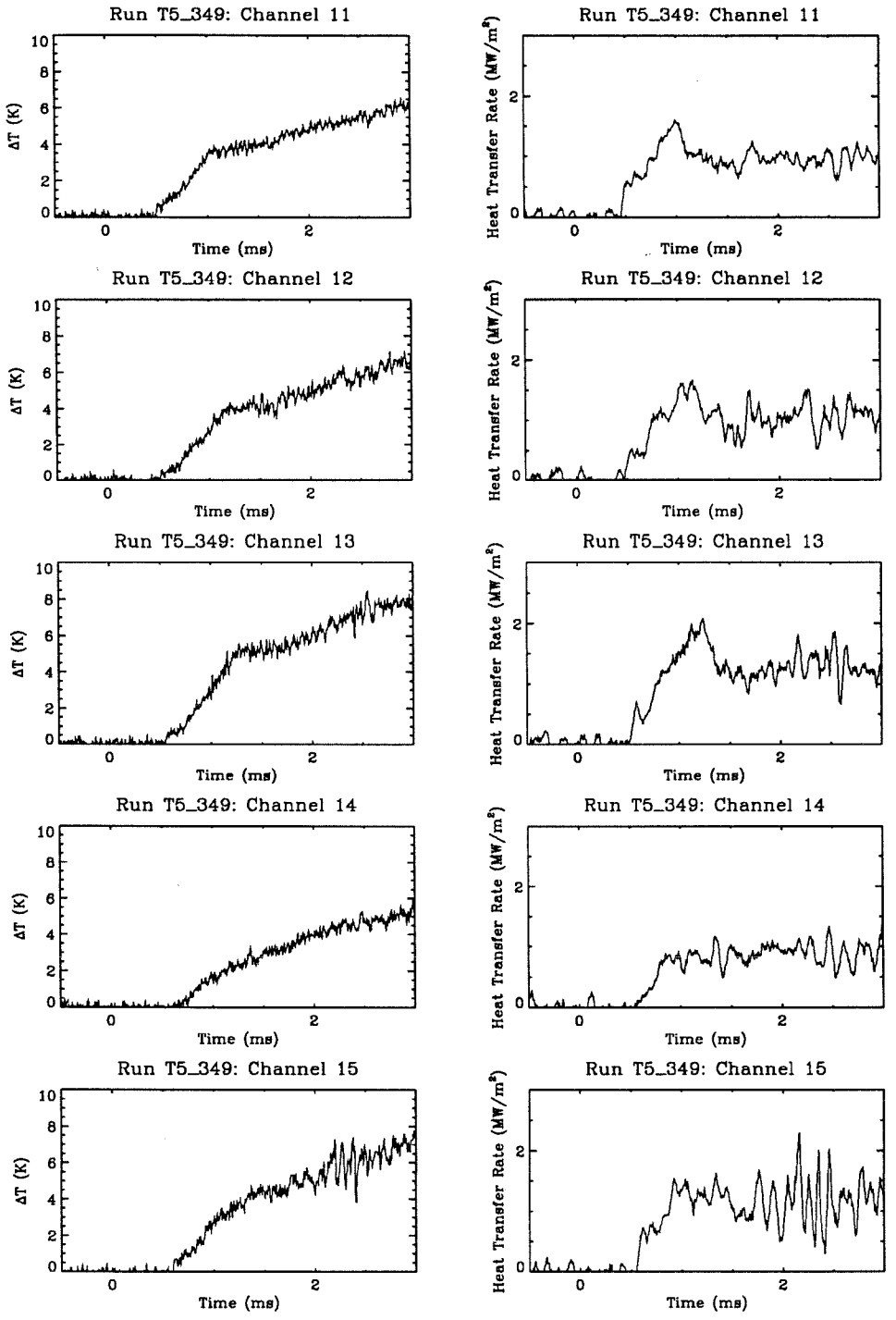

FIG. 6.2c. Continued. Typical time traces of the thermocouples. On the left are the voltage signals after conversion to temperature units and on the right are the results of the process converting them to heat tranfer rate time signals. The conditions for this particular shot were h_0 = 3.5 MJ/kg and p_0 = 47 MPa, pure nitrogen.

6.2 Flow visualization

Fig. 3.12 presented in Chapter 3, p. 51, shows a turbulent boundary layer in which flow patterns are not obvious. Figs. 6.3 through 6.14 are either resonantly enhanced interferograms or resonantly enhanced shadowgraphs showing the turbulent boundary layer. For all these test runs, only a very small amount of salt was deposited at a location corresponding to the left side of the pictures. For some of these runs, h_0 was probably so low that the salt crystals were not hot enough to dissociate into sodium and chlorine ions. The flow patterns are therefore made observable by the differential interferometer when $h_0 < 11$ MJ/kg and $p_0 > 45$ MPa. Thus, the resulting image is effectively an interferogram. The resolution is not as good as when the resonant enhancement of the refractive index technique was used, but sound waves radiating from the turbulent boundary layer can be seen. For the runs for which this technique was working, dark patterns indicate that traces of sodium convect to the upper limit, at $y = \delta$, further downstream at a distance of around a dozen times δ. The pictures clearly show some organized flow patterns which are reminiscent of those observed, for example, by Head and Bandyopadhyay (1981). Enlargement of some of the details indicates the presence of hairpin vortices viewed from the side and inclined at 40 to 50 deg. with respect to the flow direction (the boundary layer thickness is on the order of 5 to 10 mm). Head and Bandyopadhyay have observed that the distance between the hairpin legs decreases with increasing Reynolds number whereas each of the legs becomes thinner. This observation is consistent with ours. From this reference, it can also be observed that the edge of an incompressible boundary layer is much more jagged than the edge of the boundary layers presently investigated. These authors used a light sheet intersecting smoke in the flow while a line-of-sight technique was used in this work. The use of two visualization methods could explain the difference. A flow visualization setup (in the T5 laboratory) similar to Head and Bandyopadhyay's technique is needed to confirm their observations.

On Fig. 6.5 and the following ones, the corresponding Re has almost the same value as Re_{tr} measured with the surface thermocouples. On this picture, there is clearly an indication that there is some turbulent activity; this could be the observation of a turbulent spot. Most previous experimentalists have noted that the transition process starts before its detection

by the time-averaged heat flux instrumentation.

It does not appear possible to resolve precisely the viscous sublayer thickness because a line-of-sight method has been used for flow visualization. However, in Figs. 6.11, 6.12, 6.13, and 6.14, the hairpin vortices located exactly on the top of the model and viewed from the side can be distinguished. The ones on the side, should they contain traces of sodium, would definitely prevent the determination of the sublayer thickness. These hairpin vortices are transparent and it can be concluded that the sublayer thickness is certainly not 40% of the total thickness of the boundary layer as observed by Kemp and Owen (1972).

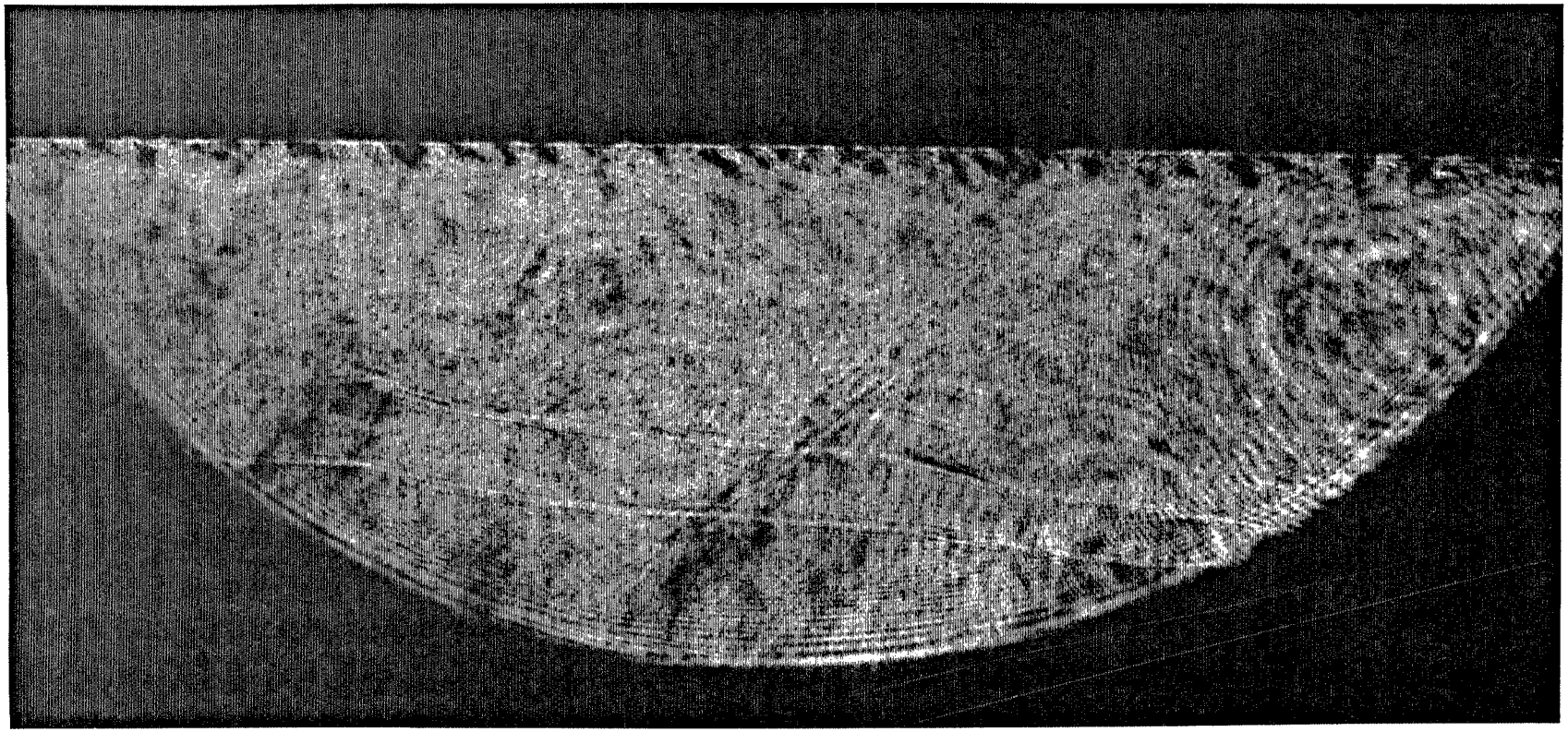

FIG. 6.3. Flow of air at h_0 = 3.4 MJ/kg and p_0 = 45 MPa (run 345, refer to 336 in Table 2). This resonantly enhanced interferogram was taken 1 ms after the nozzle reservoir pressure rise. The picture shows the boundary layer below the 5 deg. half-angle cone, starting on the left from x = 420 mm (corresponding to Re = 10.0 million) to x = 590 mm (Re = 14.2 million). As the specific enthalpy is low, the density is sufficiently high for interferometry to be sensitive enough. This picture is effectively an interferogram because the salt crystal are not hot enough to cause the dissociation of salt crystals.

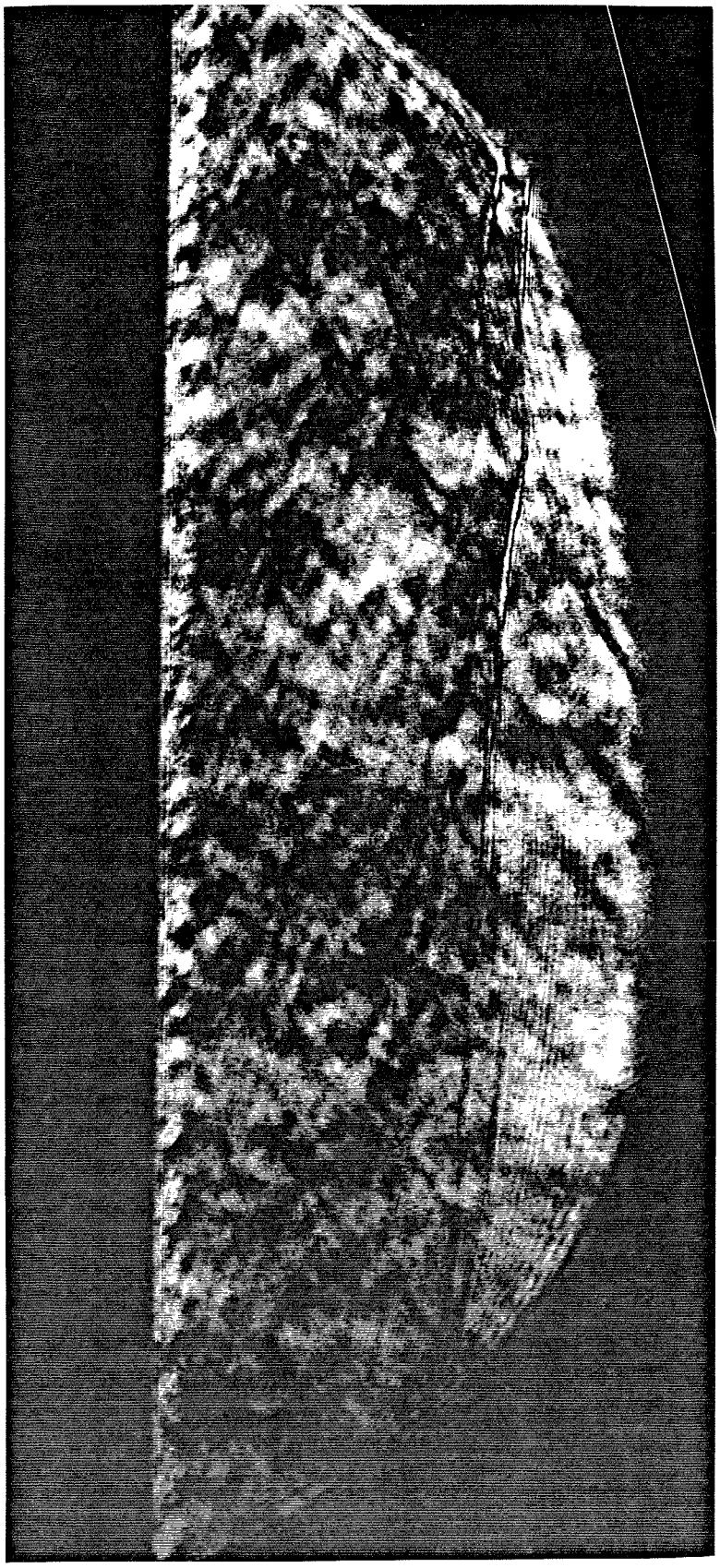

FIG. 6.4. Flow of nitrogen at h_0 = 3.4 MJ/kg and p_0 = 45 MPa (run 350, refer to 349 in Table 2). This resonantly enhanced interferogram was taken 1.3 ms after the nozzle reservoir pressure rise. The picture shows the boundary layer below the 5 deg. half-angle cone, starting on the left from x = 420 mm (corresponding to Re = 9.91 million) to x = 590 mm (Re = 13.9 million). As the specific enthalpy is low, this picture is effectively an interferogram. See also Fig. 6.3.

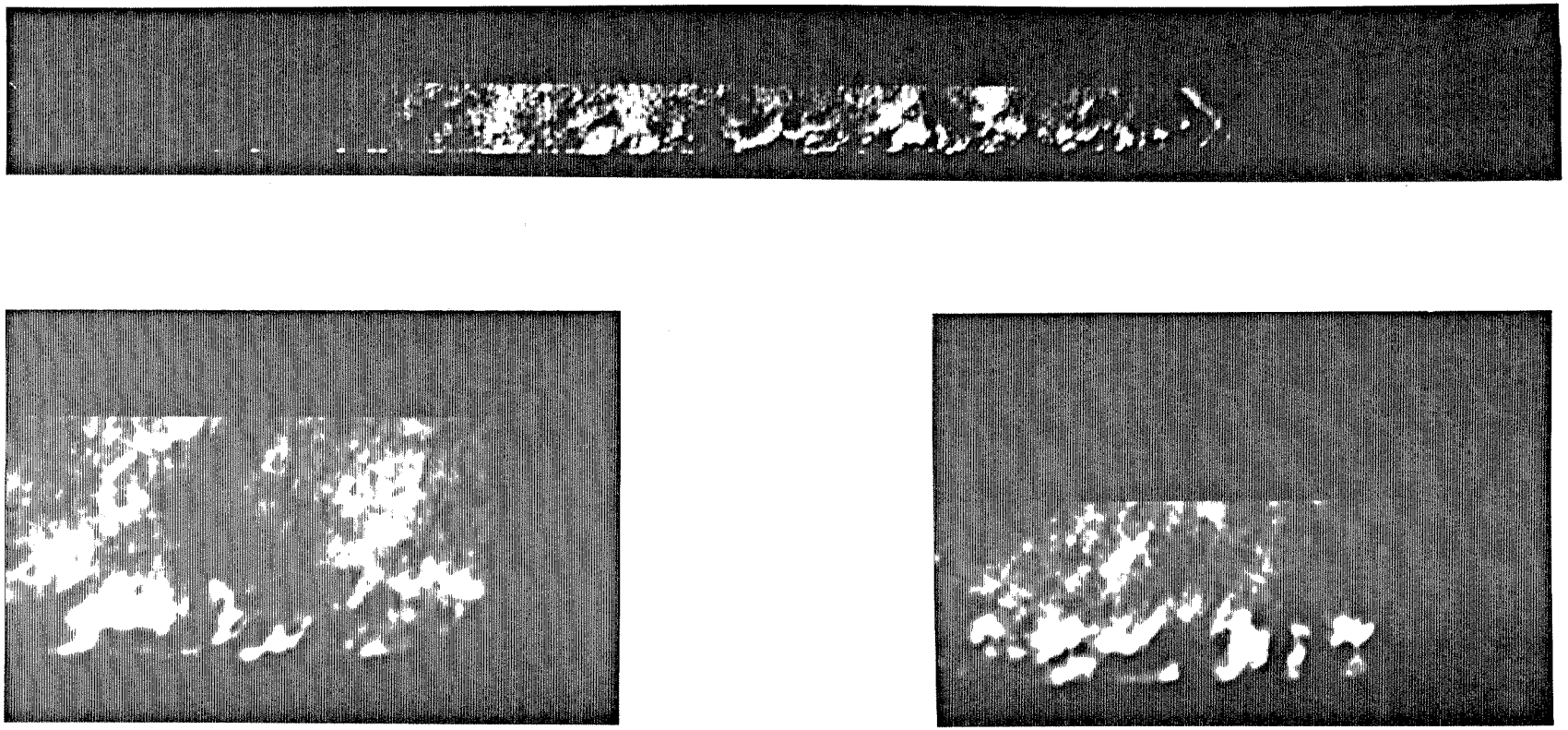

FIG. 6.5. Flow of nitrogen at h_0 = 11 MJ/kg and p_0 = 60 MPa (run 357, refer to 534 in Table 2). This resonantly enhanced interferogram was taken 1 ms after the nozzle reservoir pressure rise. The picture shows the boundary layer on the top of the 5 deg. half-angle cone, starting on the left from x = 510 mm (corresponding to Re = 2.88 million) to x = 680 mm (Re = 3.84 million). The pictures below magnify portions of the one above three times (3×). Both differential interferometry and the resonant enhancement of the refractive index technique were used for this run. The latter technique works better here than differential interferometry.

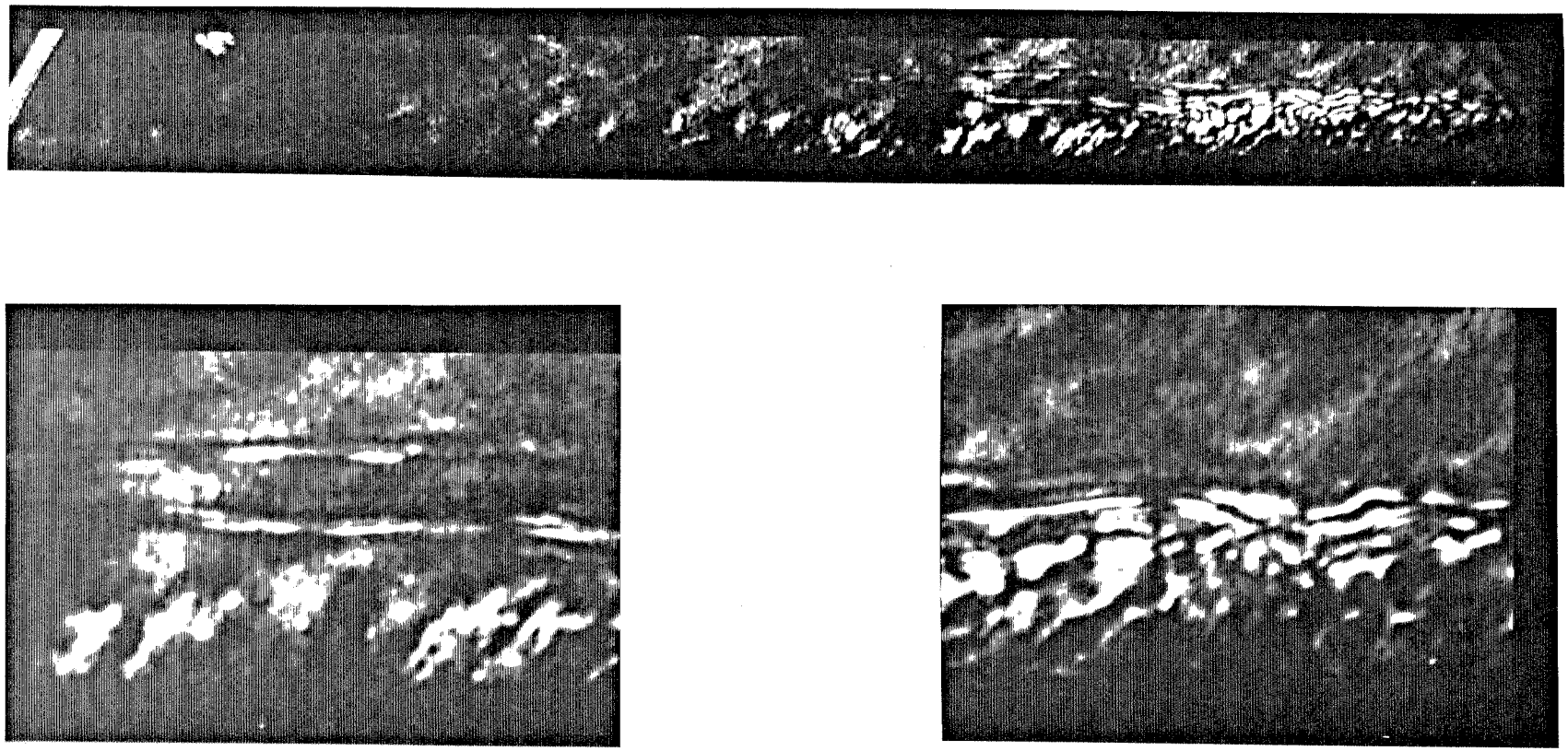

FIG. 6.6. Flow of nitrogen at h_0 = 11 MJ/kg and p_0 = 60 MPa (run 359, refer to 534 in Table 2). This resonantly enhanced interferogram was taken 1 ms after the nozzle reservoir pressure rise. The picture shows the boundary layer on the top of the 5 deg. half-angle cone, starting on the left from x = 510 mm (corresponding to Re = 2.91 million) to x = 680 mm (Re = 3.88 million). The pictures below magnify portions of the one above three times (3×). The left half of the top picture corresponds to the former and the right half corresponds to the latter giving a better resolution in the flow structure. The white streaks seen above the turbulent boundary layer on the right are interference fringes similar to those seen in Fig. 4.5.

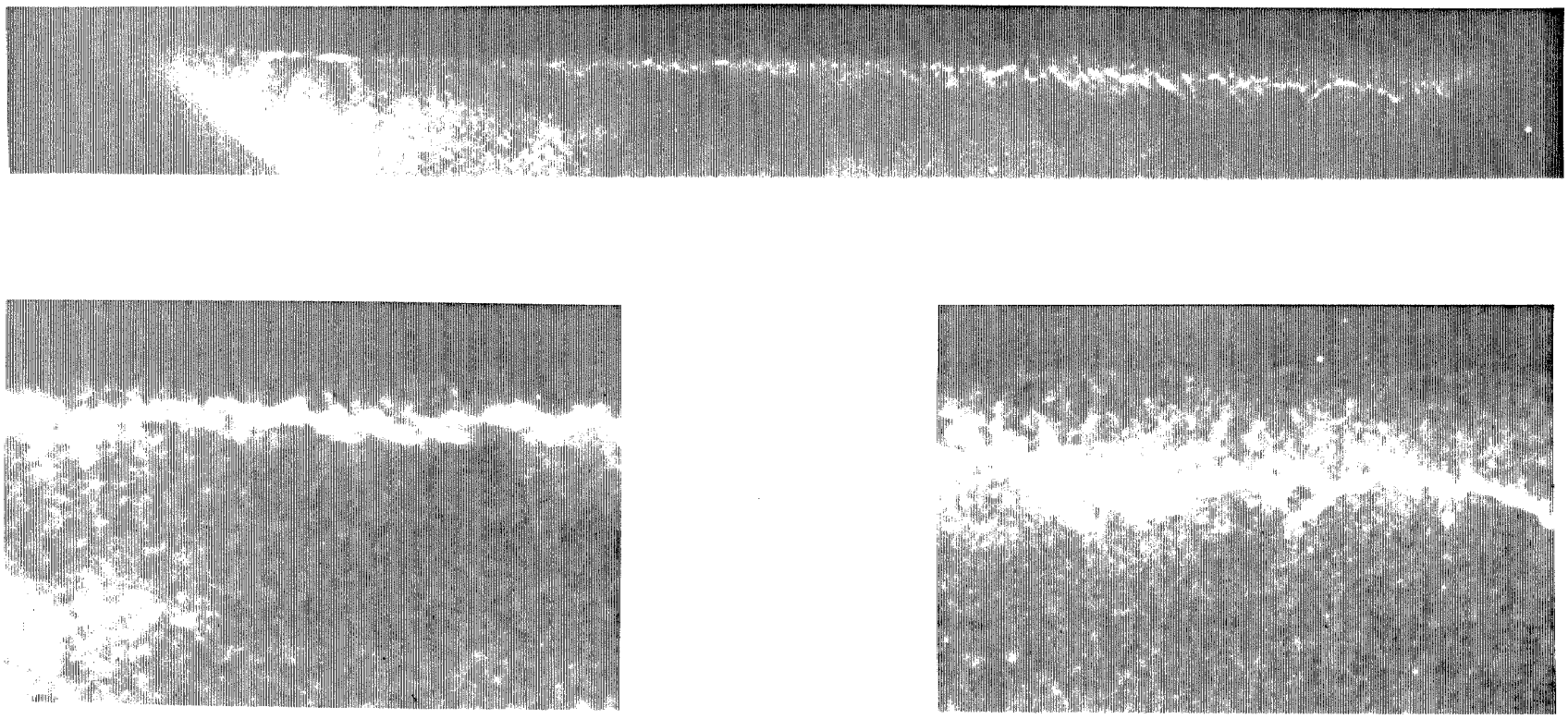

FIG. 6.7. Flow of air at h_0 = 14 MJ/kg and p_0 = 57 MPa (run 538, refer to 537 in Table 2). This resonantly enhanced shadowgraph was taken 1 ms after the nozzle reservoir pressure rise. The picture shows the boundary layer below the 5 deg. half-angle cone, starting on the left from x = 539 mm (corresponding to Re = 2.17 million) to x = 710 mm (Re = 2.86 million). The pictures below magnify portions of the one above three times (3×). This is clearly a turbulent boundary layer. Traces of sodium are entrained by the turbulence eddies toward the upper portion of the boundary layer. They reach it at some distance downstream from the location where salt was deposited.

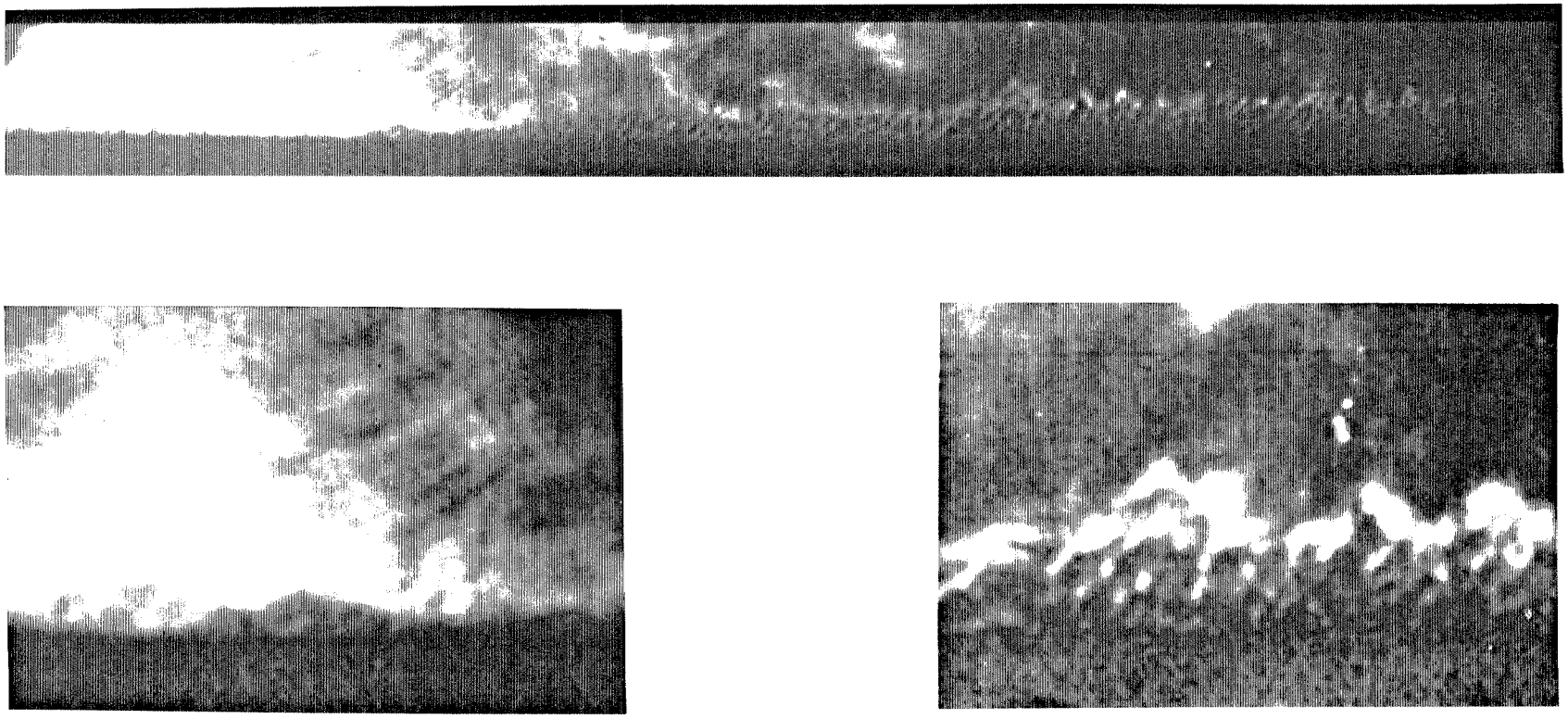

FIG. 6.8. Flow of nitrogen at h_0 = 9.7 MJ/kg and p_0 = 55 MPa (run 548, refer to 549 in Table 2). This resonantly enhanced shadowgraph was taken 1 ms after the nozzle reservoir pressure rise. The picture shows the boundary layer on the top of the 5 deg. half-angle cone, starting on the left from x = 539 mm (corresponding to Re = 3.22 million) to x = 710 mm (Re = 4.24 million). The pictures below magnify portions of the one above three times (3×). See also Fig. 6.7.

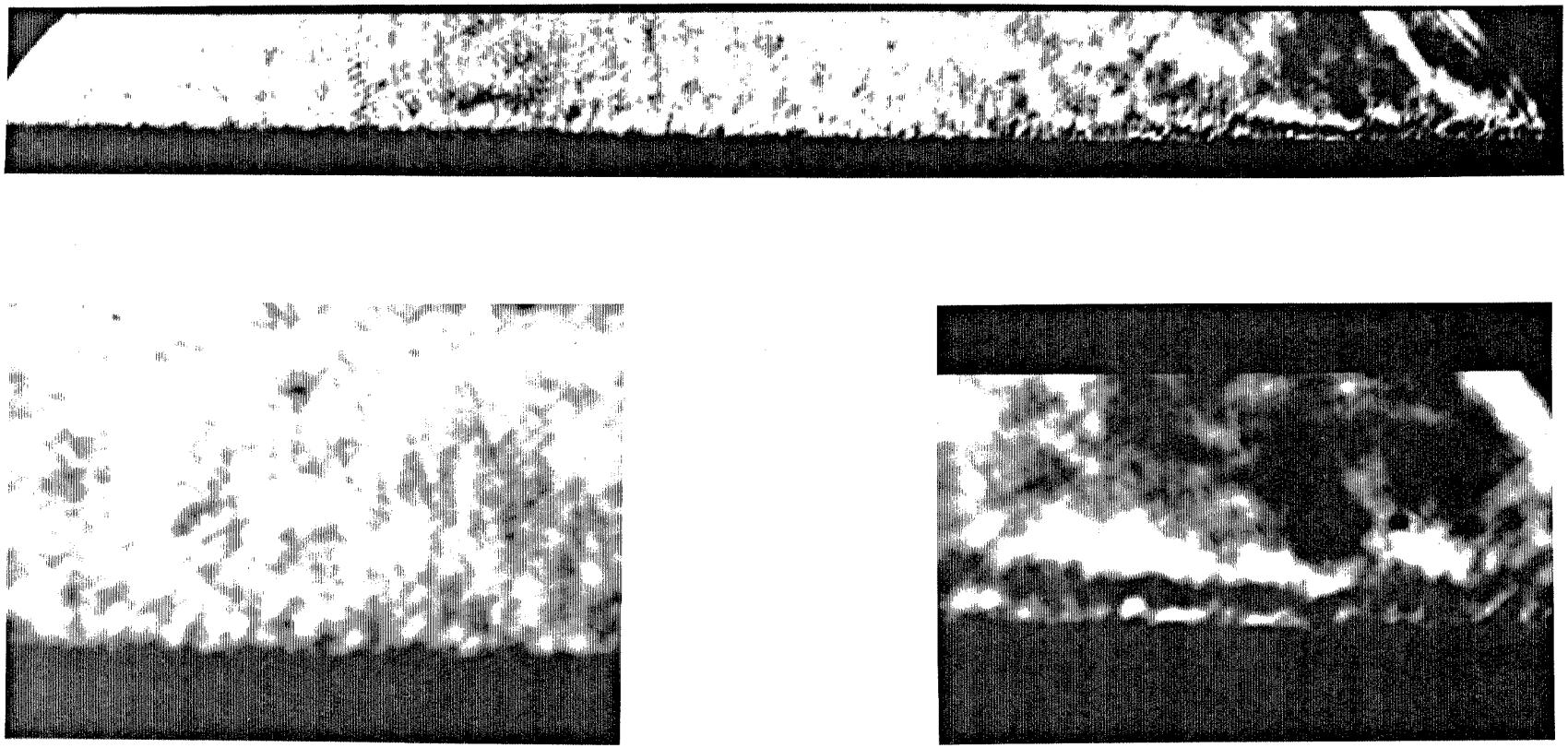

FIG. 6.9. Flow of air at h_0 = 9.1 MJ/kg and p_0 = 52 MPa (run 549). This resonantly enhanced shadowgraph was taken 1 ms after the nozzle reservoir pressure rise. The picture shows the boundary layer on the top of the 5 deg. half-angle cone, starting on the left from x = 539 mm (corresponding to Re = 3.20 million) to x = 710 mm (Re = 4.21 million). The pictures below magnify portions of the one above three times (3×). See also Fig. 6.7.

FIG. 6.10. Flow of air at h_0 = 12 MJ/kg and p_0 = 55 MPa (run 554, refer to 553 in Table 2). This resonantly enhanced shadowgraph was taken 1 ms after the nozzle reservoir pressure rise. The picture shows the boundary layer below the 5 deg. half-angle cone, starting on the left from x = 539 mm (corresponding to Re = 2.46 million) to x = 710 mm (Re = 3.24 million). The pictures below magnify portions of the one above three times (3×) and they were enhanced according to 'scheme B', described in Fig. 3.15. See also Fig. 6.7.

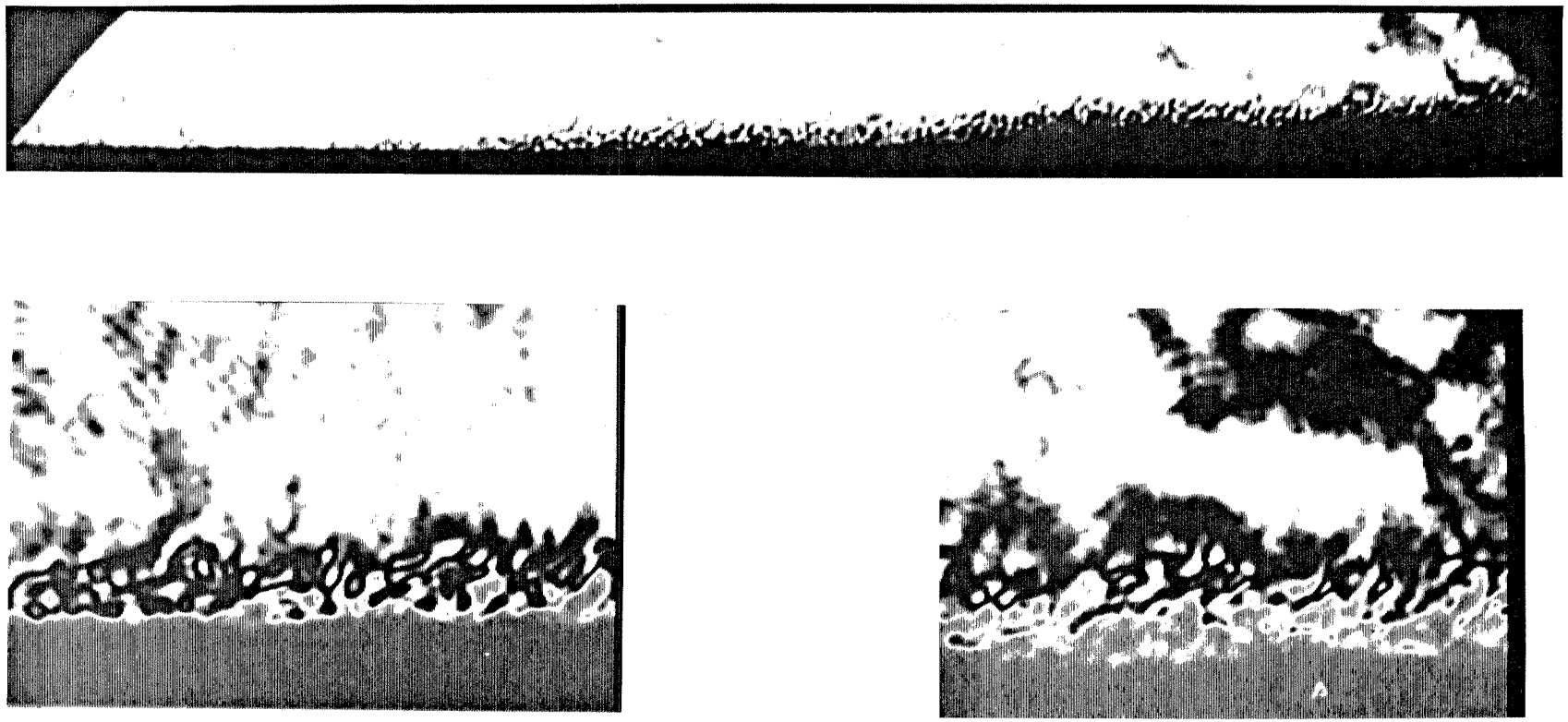

FIG. 6.11. Flow of air at h_0 = 10 MJ/kg and p_0 = 55 MPa (run 559, refer to 549 in Table 2). This resonantly enhanced shadowgraph was taken 0.75 ms after the nozzle reservoir pressure rise. The picture shows the boundary layer on the top of the 5 deg. half-angle cone, starting on the left from x = 539 mm (corresponding to Re = 2.89 million) to x = 710 mm (Re = 3.80 million). The pictures below magnify portions of the one above three times (3×) and they were enhanced according to 'scheme B', described in Fig. 3.15.

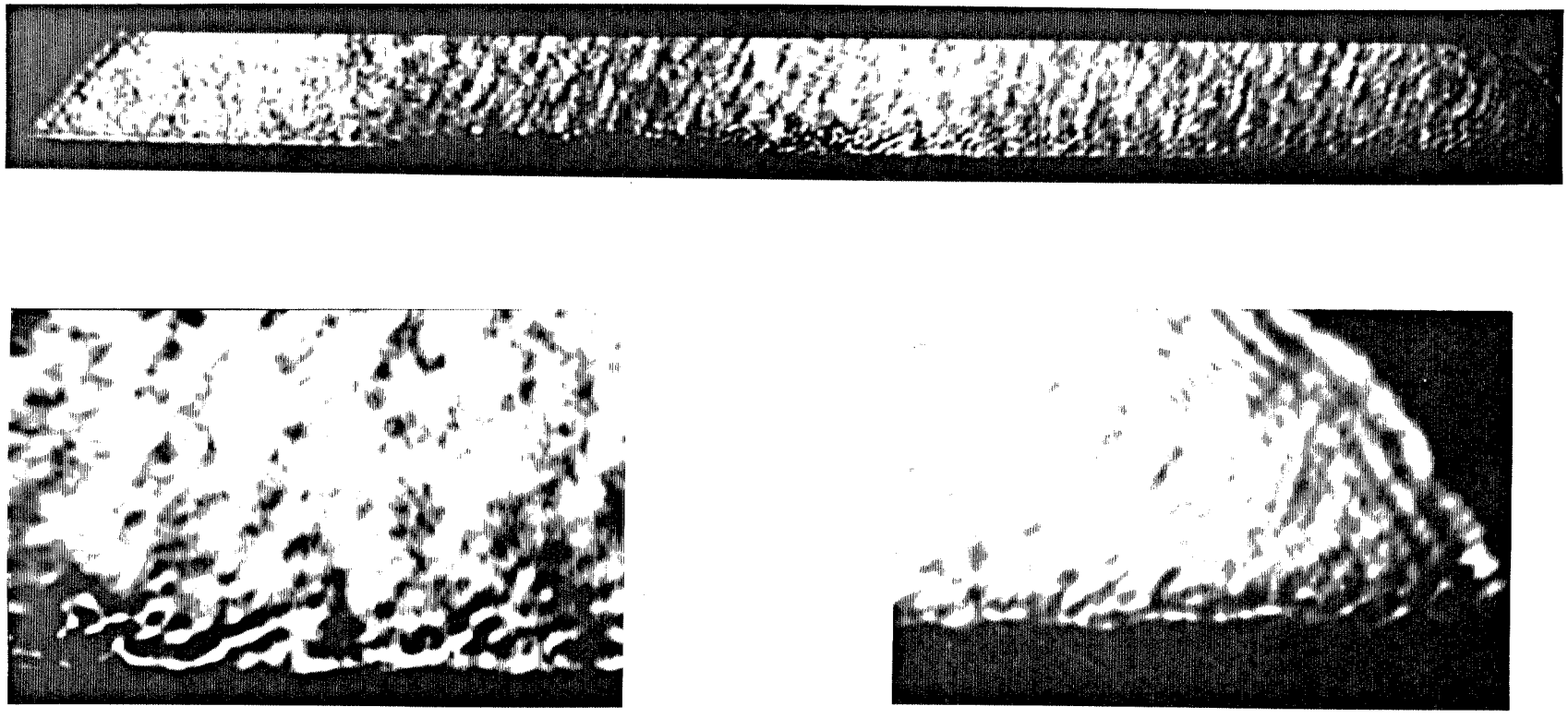

FIG. 6.12. Flow of nitrogen at h_0 = 13 MJ/kg and p_0 = 85 MPa (run 563). This resonantly enhanced shadowgraph was taken 1 ms after the nozzle reservoir pressure rise. The picture shows the boundary layer on the top of the 5 deg. half-angle cone, starting on the left from x = 539 mm (corresponding to Re = 3.43 million) to x = 710 mm (Re = 4.52 million). The pictures below magnify portions of the one above three times (3×).

FIG. 6.13. Flow of air at h_0 = 11 MJ/kg and p_0 = 55 MPa (run 576, refer to 553 in Table 2). This resonantly enhanced shadowgraph was taken 1 ms after the nozzle reservoir pressure rise. The picture shows the boundary layer on the top of the 5 deg. half-angle cone, starting on the left from x = 539 mm (corresponding to Re = 2.86 million) to x = 710 mm (Re = 3.77 million). The pictures below magnify portions of the one above three times (3×) and they were enhanced according to 'scheme B', described in Fig. 3.15.

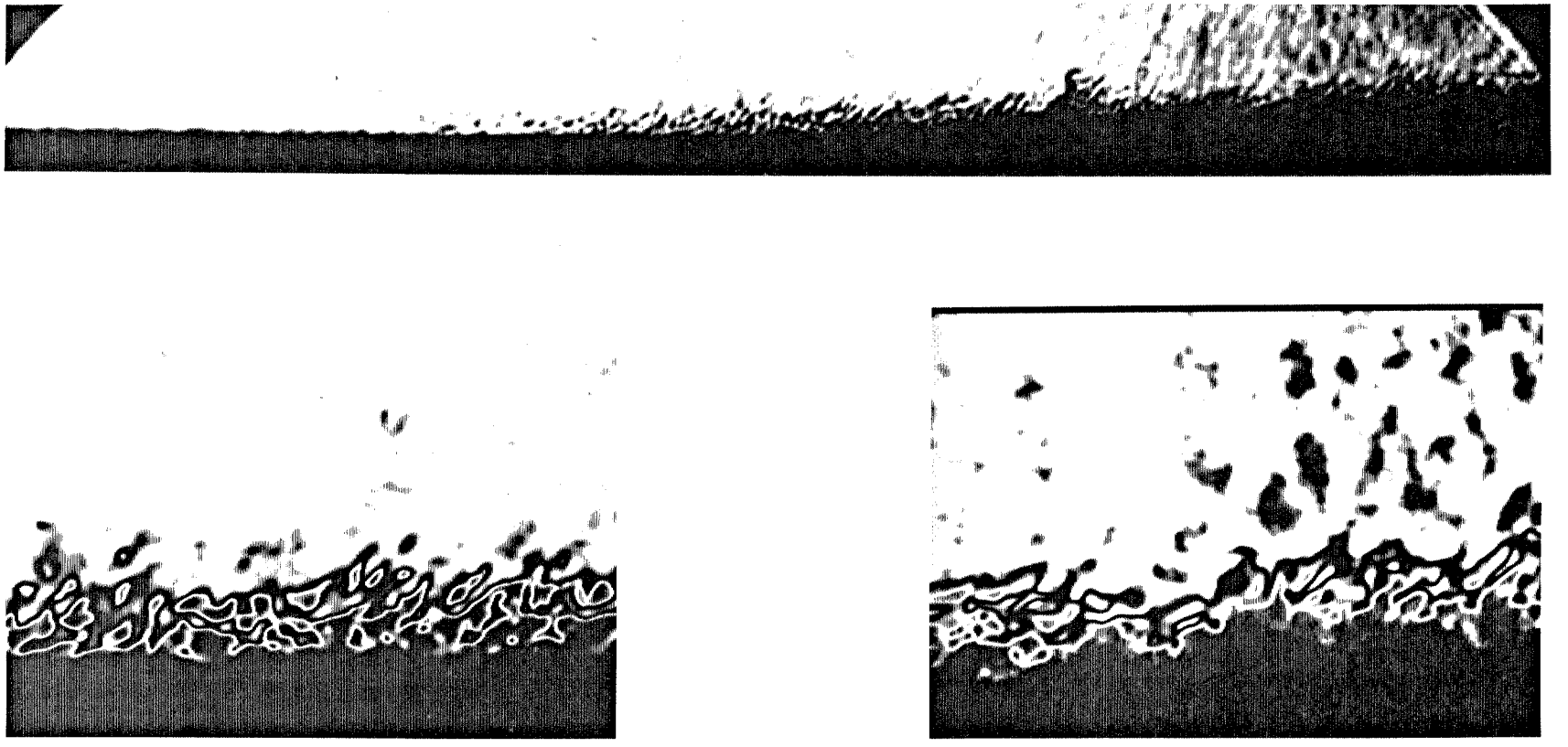

FIG. 6.14. Flow of air at h_0 = 11 MJ/kg and p_0 = 57 MPa (run 579, refer to 553 in Table 2). This resonantly enhanced shadowgraph was taken 1 ms after the nozzle reservoir pressure rise. The picture shows the boundary layer on the top of the 5 deg. half-angle cone, starting on the left from x = 539 mm (corresponding to Re = 1.63 million) to x = 710 mm (Re = 2.15 million). The pictures below magnify portions of the one above three times (3×) and they were enhanced according to 'scheme B', described in Fig. 3.15.

6.3 Chapter summary

In this chapter, a series of results corresponding to the turbulent regime has been presented. The experimental data fall on the prediction curve based on an incompressible flow correlation corrected to account for compressibility effects using Van Driest's approximation method. No real-gas effect seems present and the structure of the boundary is not qualitatively different from an incompressible turbulent boundary layer. This conclusion is reached after observations of a preferred alignment angle (40-50 deg.) of the turbulent patterns with respect to the flow direction.

CHAPTER 7

Miscellaneous topics

This chapter addresses specific potential problems encountered during the experimental campaign. If the longitudinal alignment procedure was not appropriate, what are the effects of a slight angle of incidence? If the bluntness of the tip increases, what is its effect on the transition Reynolds number? What is the effect of too large a deposition of salt on the stability of the boundary layer? Is it possible to trip the boundary layer, allowing further study of its turbulent regime? Finally, the last topic which is addressed is the signal quality of the heat transfer rate mesurements.

7.1 Angle of incidence

Chapter 3 described the procedure used for longitudinal alignment. It was mentioned that both the pitch and yaw angle were less than 0.02 deg. To check how critical this was, two identical tests were run with the cone at two different roll angles and with the same tip. In the first test, the separation plane between the two half-cones was horizontal. The cone was then rolled through 90 deg. in the second test. Both runs, at the same flow conditions, show transition starting at around 40 cm from the tip along the centerline (for all the runs presented in this chapter, refer to run 534, Table 2, Chapter 3). No large difference can be detected as shown in Fig. 7.1.

7.2 Bluntness

The possibility of a nose radius effect was also investigated. In a similar fashion as the case of the angle of incidence, two identical runs were conducted with two different tips: an old one (with a nose radius of 0.15 mm) and an new one (with a nose radius less than 0.06 mm). Fig. 7.2 presents a superposition of the results which shows no perceptible difference. If there is a bluntness effect, it is expected that as the nose radius increases so does Re_{tr} according to Stetson and Rushton (1967).

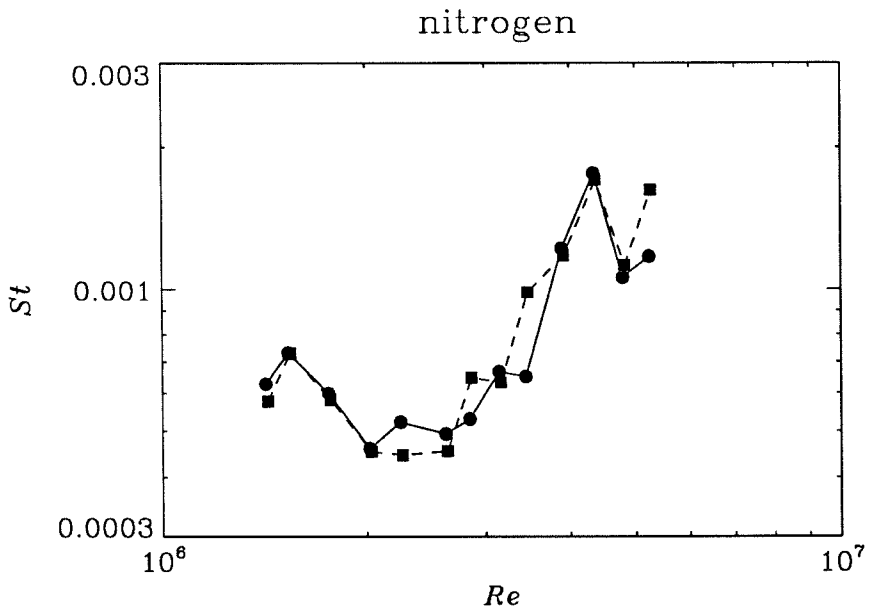

FIG. 7.1. Two heat transfer rate distributions for nitrogen flow with the cone at two different roll angles (squares, run 353: before 90 deg. rotation, circles, run 355: after), with nominally the same conditions, h_0 = 11 MJ/kg, p_0 = 60 MPa.

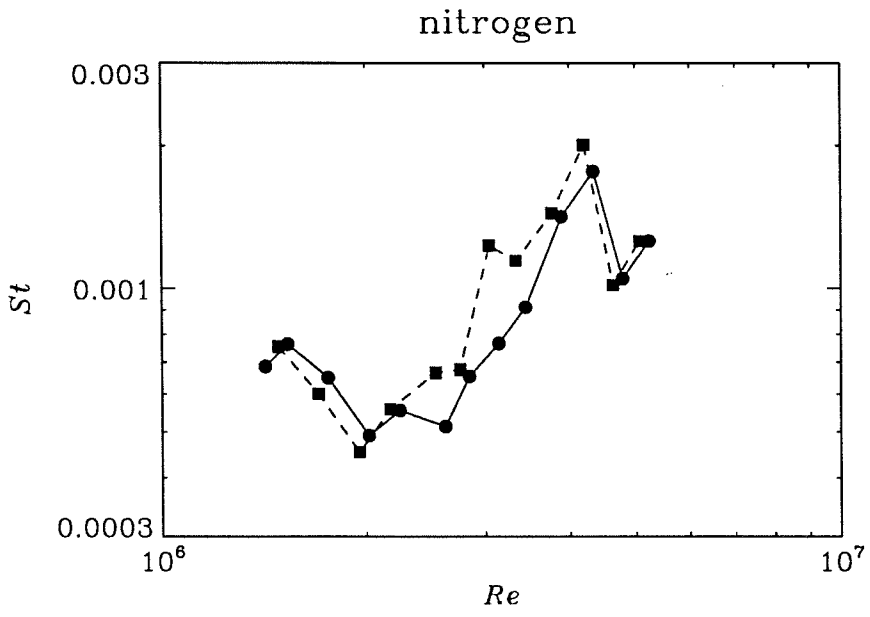

FIG. 7.2. Two heat transfer rate distributions for nitrogen flow with two different tips with nominally the same conditions, (squares, run 359: new tip, circles, run 355: old tip), h_0 = 11 MJ/kg, p_0 = 60 MPa.

7.3 Salt deposition

Whenever salt is deposited on the model surface, only a very small drop of saline solution is used with no effect on the heat transfer rate measurements. Earlier in the experimental campaign, it was neither known how much salt was needed nor what the effects of the salt crystals were on the flow behavior. So the first two sections of the model (thus a length of 203 mm) were circumferentially coated with salt crystals of the same dimensions mentioned in Chapter 3. Fig. 7.3 shows two heat transfer distributions with and without this amount of salt deposition (other conditions being identical). As can be seen, the effect of the salt is to cause earlier transition. (Note that usually the amount of salt deposited did not cause transition.)

This effect is further evidenced by the pictures taken with the resonant enhancement of the refractive index technique. Figs. 7.4 and 7.5 show very thick turbulent boundary layers. Under normal conditions, the boundary layer shown in Fig. 7.4 would be in the transitional regime whereas the one in Fig. 7.5 would be laminar. This discrepancy indicates the possibility that the salt crystals trip the boundary layer. This trip can either be a

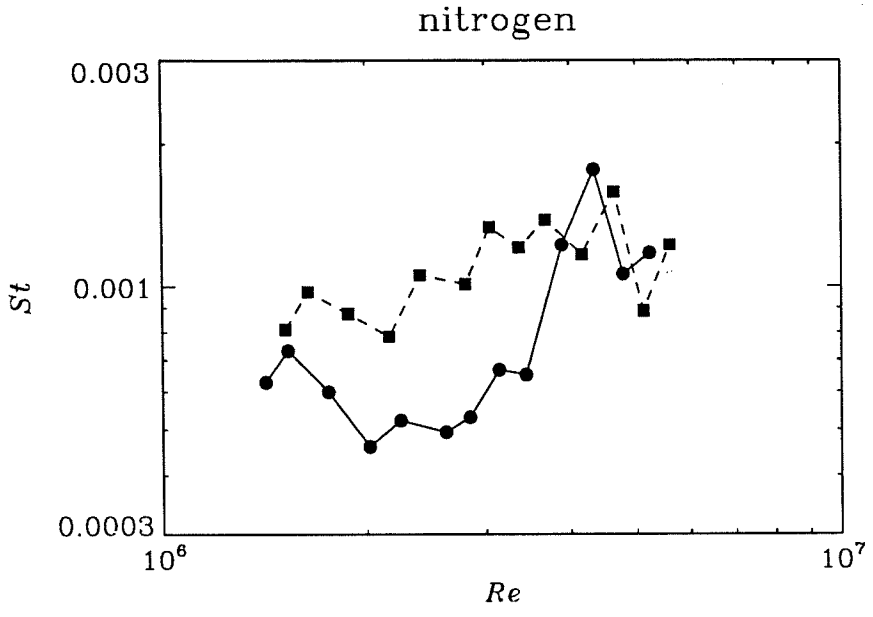

FIG. 7.3. Two heat transfer rate distributions for nitrogen flow with (squares, run 337) and without (circles, run 355) salt deposition, h_0 = 11 MJ/kg, p_0 = 60 MPa.

mechanical phenomenon which is known to be difficult to obtain in hypersonic flow or a chemical phenomenon where either sodium or chlorine ions act as a catalyst (speeding up the test gas dissociation and/or recombination reactions) or the dissociation of salt causes a heat-sink effect, both of which would lower the local static temperature. A lower static temperature is an indication of real-gas effects as mentioned in Chapter 5. Real-gas effects, however, stabilize the boundary layer under the same free-stream conditions. Therefore, it is likely that the observed phenomenon is mechanical in nature, *i.e.*, with no chemical reactions involved.

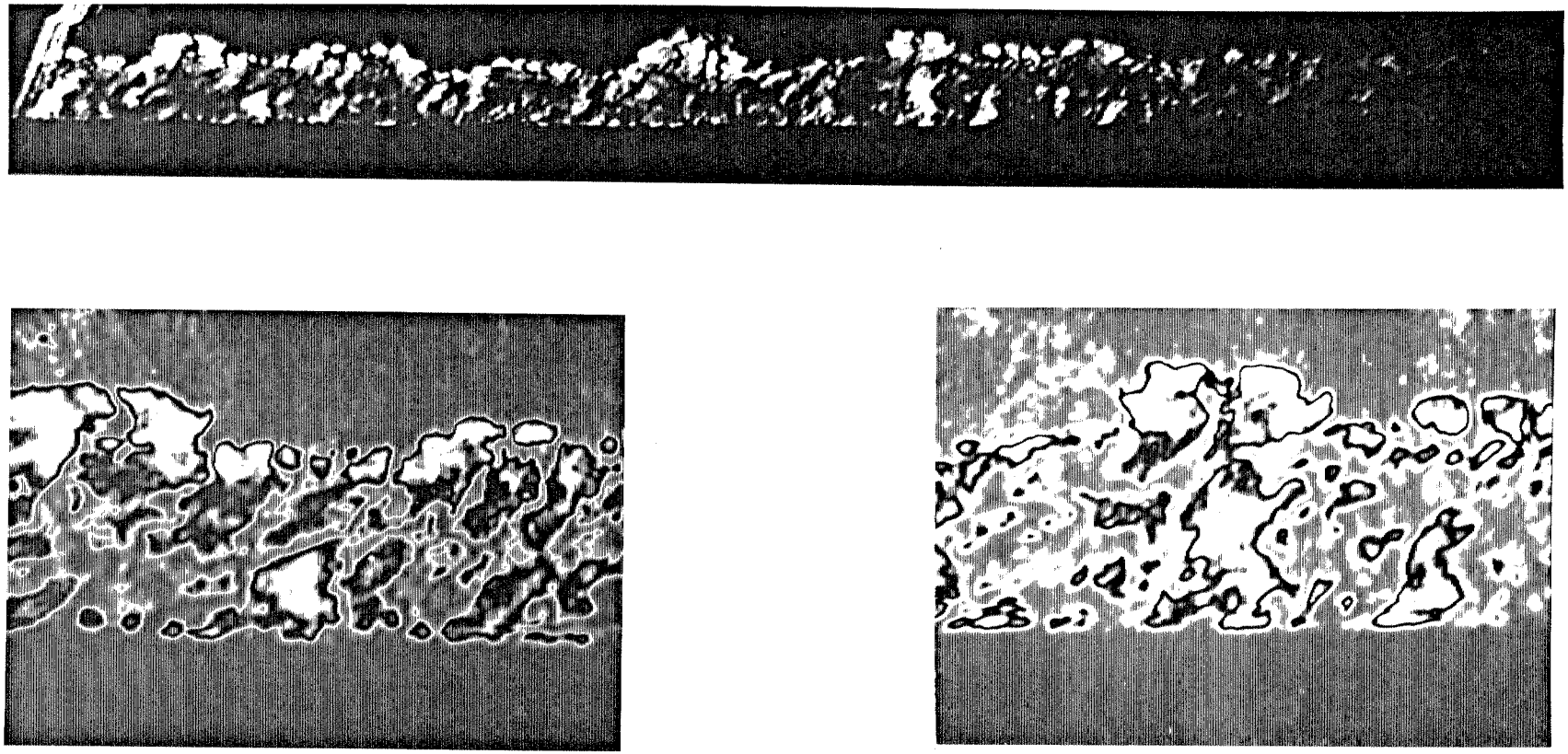

FIG. 7.4a. Flow of air at h_0 = 10 MJ/kg and p_0 = 55 MPa (run 338, refer to 549 in Table 2). This resonantly enhanced interferogram was taken 1 ms after the nozzle reservoir pressure rise. The picture shows the boundary layer on the top of the 5 deg. half-angle cone, starting on the left from x = 420 mm (corresponding to Re = 2.33 million) to x = 590 mm (Re = 3.27 million). The pictures below magnify portions of the one above three times (3×) and they were enhanced according to 'scheme B', described in Fig. 3.15.

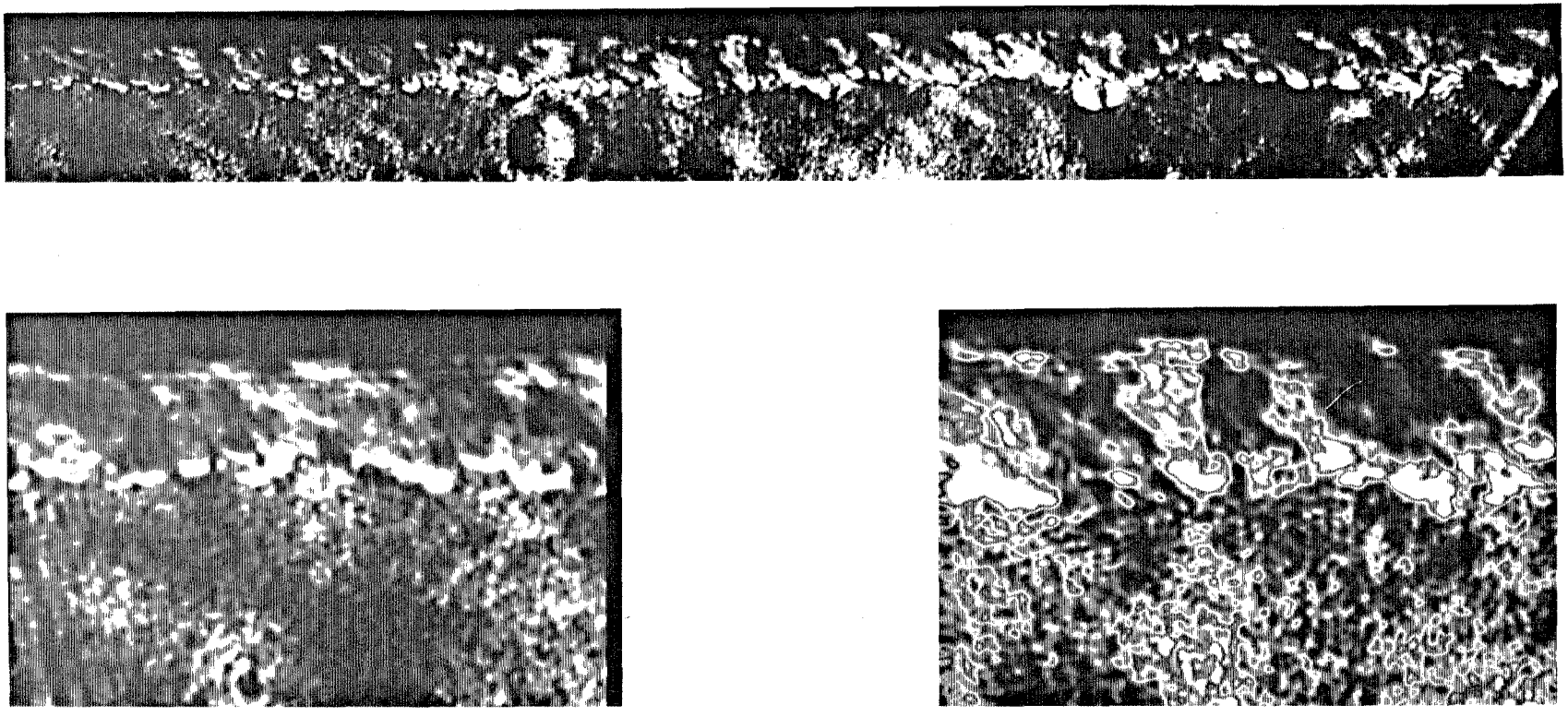

FIG. 7.4b. Flow of air at h_0 = 10 MJ/kg and p_0 = 55 MPa (run 338, refer to 549 in Table 2). This resonantly enhanced interferogram was taken 1 ms after the nozzle reservoir pressure rise. The picture shows the boundary layer below the 5 deg. half-angle cone, starting on the left from x = 420 mm (corresponding to Re = 2.33 million) to x = 590 mm (Re = 3.27 million). The pictures below magnify portions of the one above three times (3×). The image on the right was enhanced according to 'scheme B', described in Fig. 3.15.

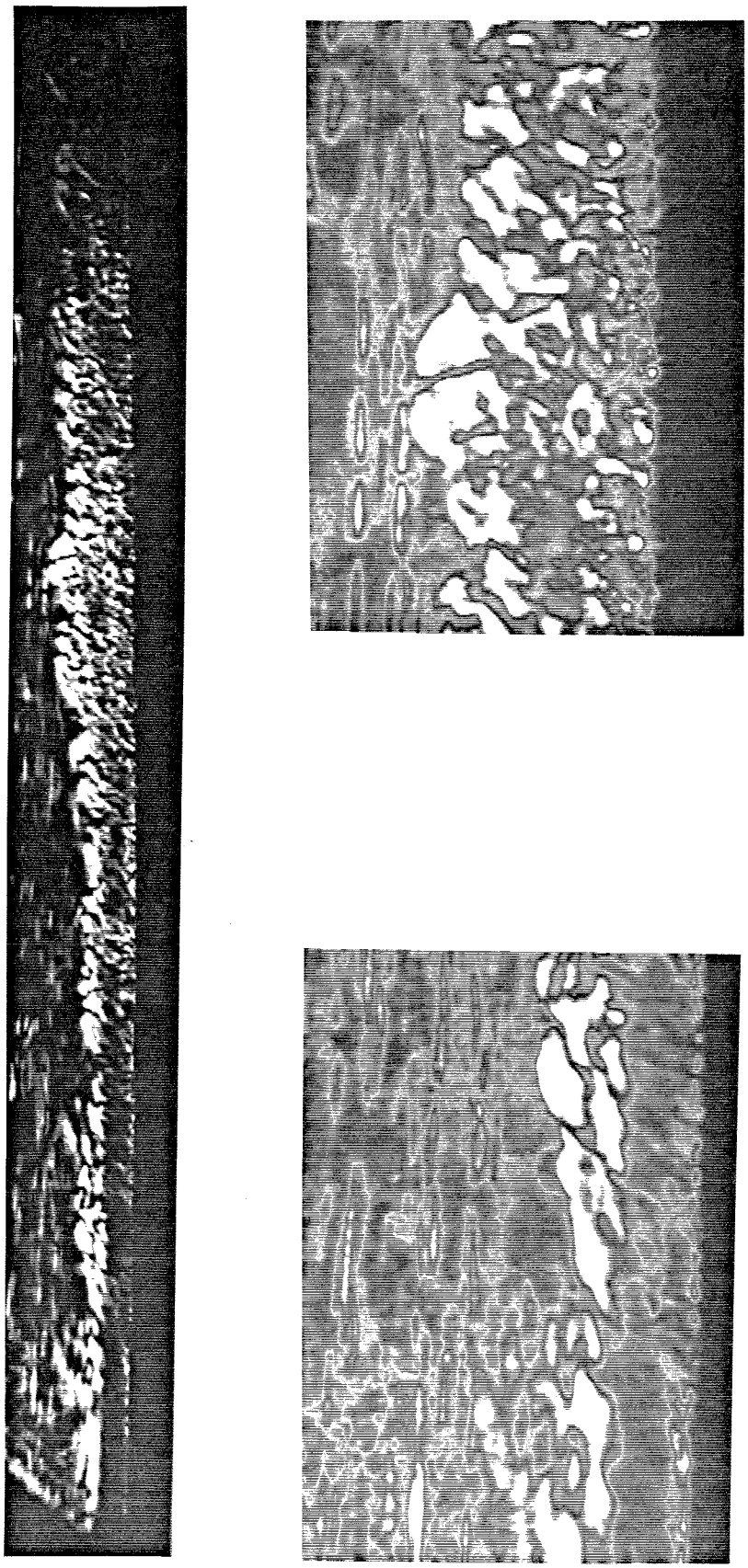

FIG. 7.5a. Flow of nitrogen at h_0 = 20 MJ/kg and p_0 = 55 MPa (run 340, refer to 140 in Table 2). This resonantly enhanced interferogram was taken 1 ms after the nozzle reservoir pressure rise. The picture shows the boundary layer on the top of the 5 deg. half-angle cone, starting on the left from x = 420 mm (corresponding to Re = 1.15 million) to x = 590 mm (Re = 1.62 million). The pictures below magnify portions of the one above three times (3×) and they were enhanced according to 'scheme B', described in Fig. 3.15.

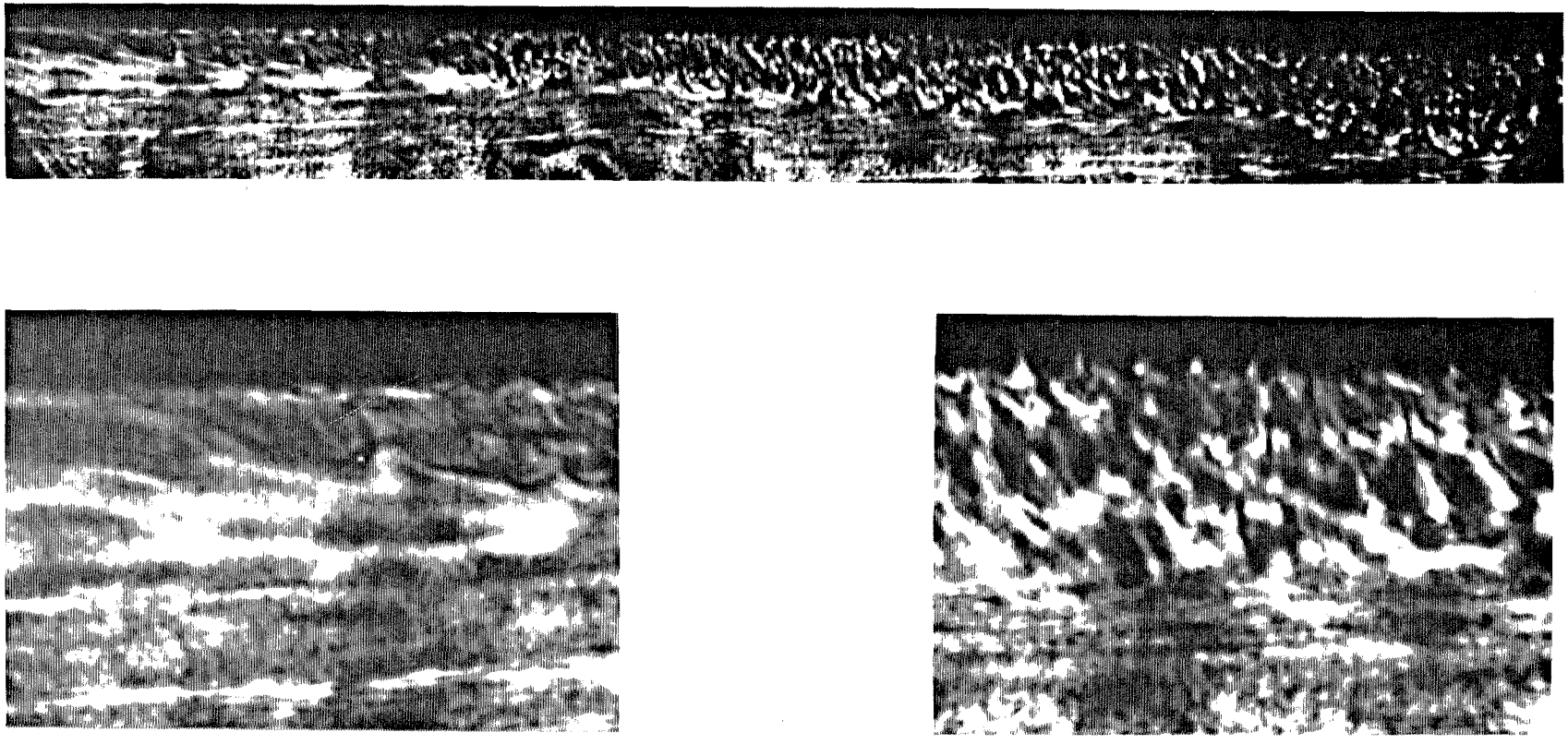

FIG. 7.5b. Flow of nitrogen at h_0 = 20 MJ/kg and p_0 = 55 MPa (run 340, refer to 140 in Table 2). This resonantly enhanced interferogram was taken 1 ms after the nozzle reservoir pressure rise. The picture shows the boundary layer below the 5 deg. half-angle cone, starting on the left from x = 420 mm (corresponding to Re = 1.15 million) to x = 590 mm (Re = 1.62 million). The pictures below magnify portions of the one above three times (3×). On the top picture, the turbulent flow patterns appear to be hairpin vortices viewed from the side. The angle between the vortices and the flow direction can clearly be seen to increase as Re increases.

An idea to check whether this trip is mechanical or chemical in nature is to try to mount on the model small obstacles (or roughness) with dimensions in the order of those of the salt crystals. This operation was done by installing small pieces of copper wire 125 μm thick. These little 'spikes' were clamped between the Waspalloy tip and the solid aluminum section (at x = 76 mm from the tip) and between this piece and the main body (at x = 203 mm from the tip). The pieces of wire were aligned in the radial direction, 3 or 4 mm apart. On the first test, the wires were protruding above the cone surface by about 250 μm. No salt was deposited. Fig. 7.6 shows two heat transfer rate distributions with and without the spikes. As in the case of the circumferential salt distribution on the first two conical sections, there is clearly an effect. On the next step, the spikes were shortened down close to 100 μm, but as can be seen also in Fig. 7.6 , there is no noticeable effect. The difference is probably due to the fact that the salt crystals, although shorter, are distributed randomly from x = 0 to x = 203 mm, whereas the copper spikes are positioned only at x = 76 mm and at x = 203 mm.

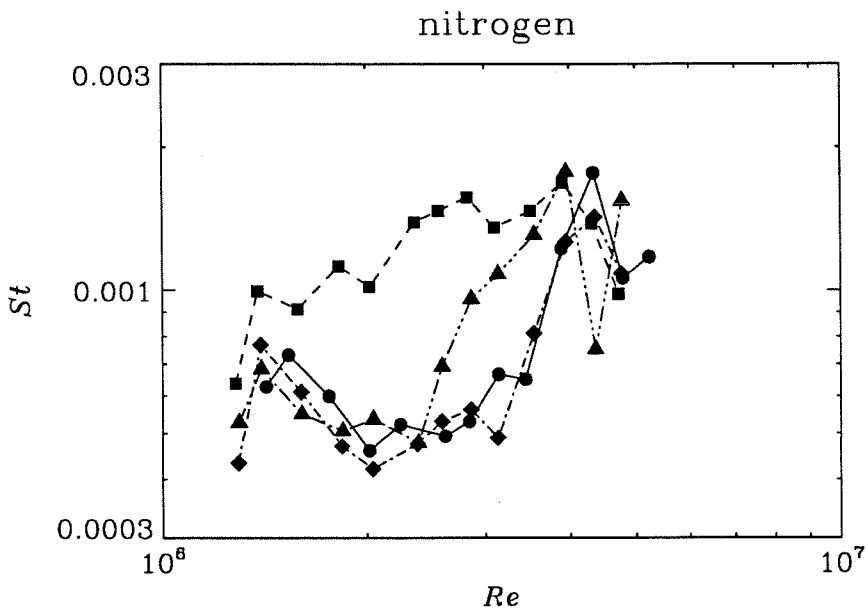

FIG. 7.6. Four heat transfer rate distributions for nitrogen flow with 250 μm high spikes radially distributed at x = 76 mm and at x = 203 mm (squares, run 577), with 100 μm high spikes (diamonds, run 579), without any (circles, run 355) and with a 1 mm high single spike (triangles, run 155). All these runs were conducted at h_0 = 11 MJ/kg, p_0 = 60 MPa.

The necessity of the circumferential distribution of the roughness was evidenced by a run in which a single stainless steel spike was present at x = 203 mm. It was made of a 100 μm thick shim, 1 mm high and 1 mm wide (more than the displacement boundary layer thickness). It was installed at the same angular position as the first thermocouple, *i.e.*, the spike was directly in front it. No effect can be detected as shown in Fig. 7.6. Hence a trip of the hypersonic boundary layer is achievable and can be obtained successfully if it consists of circumferentially and longitudinally distributed single obstacles.

However, in the above experiments, there was always a gap left in between the model sections because of the thickness of the wire or the shim. Further experiments were carried out to check if this gap had a possible tripping effect. This gap or cavity was located at x = 203 mm on the surface perpendicular to the flow direction so that inviscid-viscous interactions (if there were any) would create harmonic acoustic disturbances which would propagate downstream and destabilize the boundary layer. This gap was obtained by unscrewing the second section of the cone leaving a circumferential cavity 5 mm deep and of various widths: 0.127, 0.254, 0.508 and 0.889 mm. The four runs were conducted with nitrogen at p_0 = 55 MPa and h_0 = 12 MJ/kg. The results shown in Fig. 7.7 show no significant effect.

7.4 Signal quality

It was found that the signal-to-noise ratio of the heat transfer measurements decreases when $h_0 > 19$ MJ/kg. It also decreases at high stagnation pressure ($p_0 > 60$ MPa). This increase is probably due to charged particles in the boundary layer (in which there could be some ionization). We speculate that these particles cause the voltage of either the model or the gauge (or both) to fluctuate greatly with respect to the ground level of the differential amplifiers. This ground is common to that of the entire data acquisition system. In other words, there is a possibility of a transient earth loop. For various conditions, the possibility of an earth loop is evidenced in Fig. 7.8 which shows the time traces of a sixteenth gauge which was not exposed to the flow but was connected to the data acquisition system in the

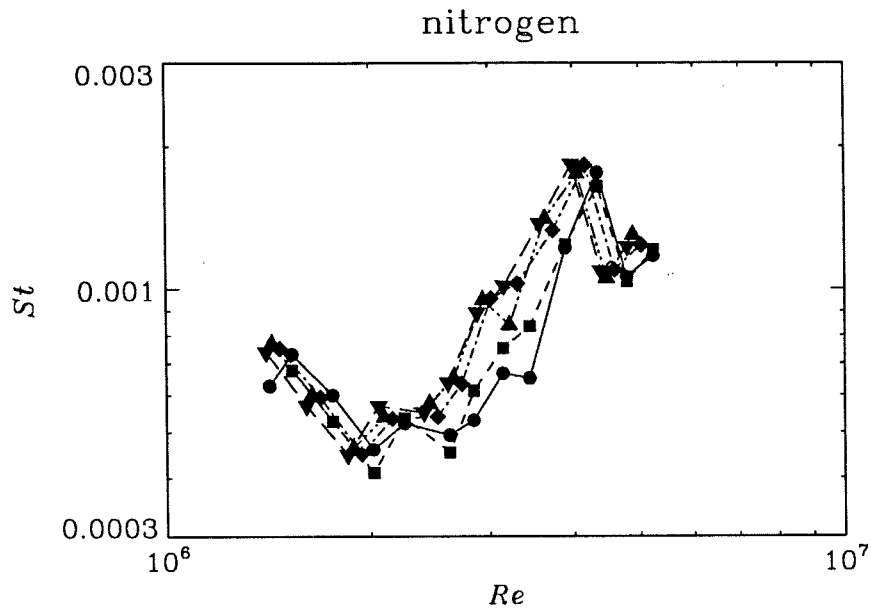

FIG. 7.7. Heat transfer rate distributions for shots with different cavity sizes: 0 mm (circles, run 355), 0.127 mm (inverted triangles, run 353), 0.254 mm (diamonds, run 357), 0.508 mm (squares, run 356), 0.889 mm (triangles, run 358), h_0 = 12 MJ/kg, p_0 = 60 MPa, pure nitrogen.

same manner as the other ones. When $h_0 > 19$ MJ/kg, it is very likely that the measured heat fluxes are all affected by this problem. The time trace of the sixteenth gauge was processed as the other gauges for three typical cases as shown in Fig. 7.9. For run 142, the heat flux signals (shown in Fig. 4.1) were averaged between t = 0.75 ms and t = 1.25 ms. The difference between each of the averages and the average of the sixteenth gauge signal is of order $\pm 10\%$ (whereas it is less than $\pm 1\%$ at the other conditions). This causes an additional uncertainty in the heat flux distribution which explains the larger data scattering when $h_0 > 19$ MJ/kg.

One can show that the fluctuations recorded by the data acquisition system are broad-band noise. As shown in Fig. 7.10, a digital Fourier transform of typical time traces gives a fairly flat spectrum, going from 0 to 100 kHz (the actual Nyquist frequency, the sampling rate being at 200 kHz). The frequency spectra are similar for all flow regimes and free-stream conditions. Cross-correlations and auto-correlations of these time traces were performed and the results are inconclusive.

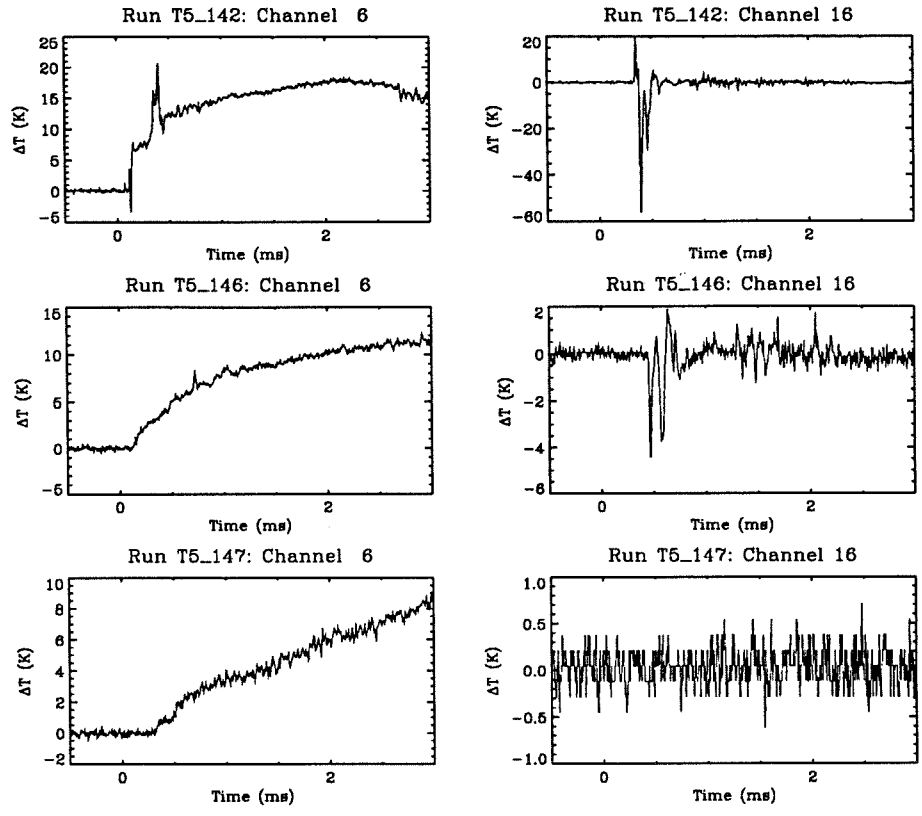

FIG. 7.8. On the left are typical temperature time traces for various conditions (p_0 = 60 MPa, h_0 = 22 MJ/kg for run 142, h_0 = 11 MJ/kg for run 146 and h_0 = 3.4 MJ/kg for run 147). On the right are the corresponding time traces of a sixteenth gauge which was not exposed to the flow but connected to the data acquisition system like the other ones.

Three different problems have been addressed. It was found that there was no presence of angle of incidence or bluntness effects. It was also found that an exaggerated amount of salt deposition on the cone tip trips a stable boundary layer. This effect can be useful in studying the structure of a more developed hypersonic turbulent boundary layer. The quality of the time traces has also been examined by a Fourier analysis. No meaningful information can be extracted from the time traces except a time-averaged value of the local heat transfer rate.

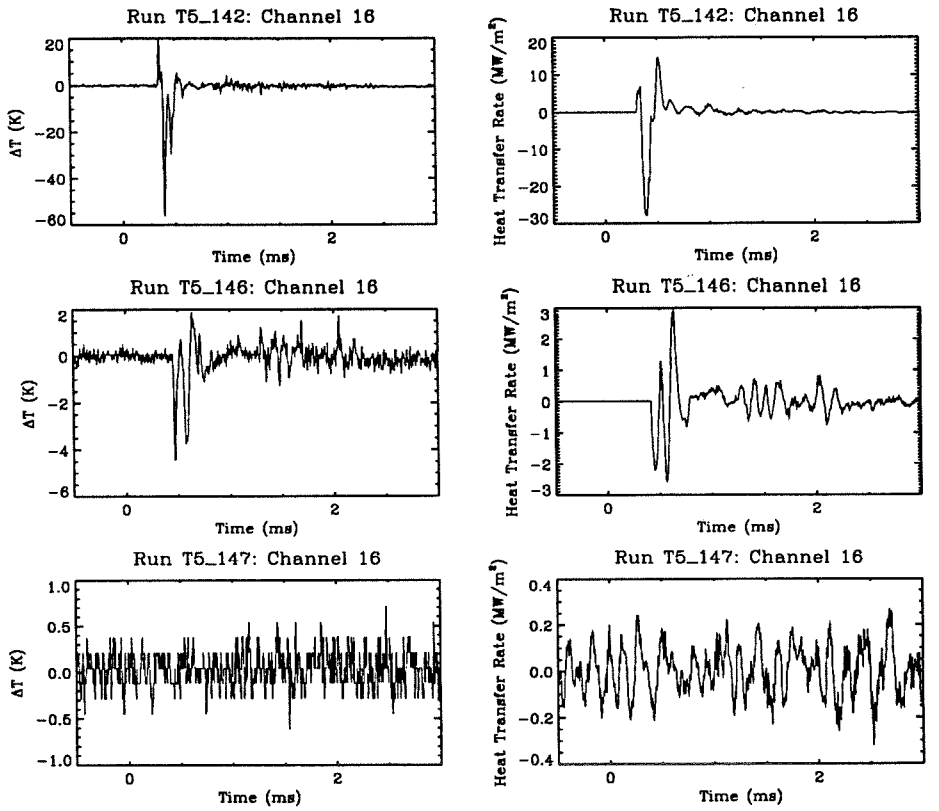

FIG. 7.9. On the left are the corresponding time traces of a sixteenth gauge which was not exposed to the flow but connected to the data acquisition system like the other ones (p_0 = 60 MPa, h_0 = 22 MJ/kg for run 142, h_0 = 11 MJ/kg for run 146 and h_0 = 3.4 MJ/kg for run 147). On the right are the corresponding heat flux time traces.

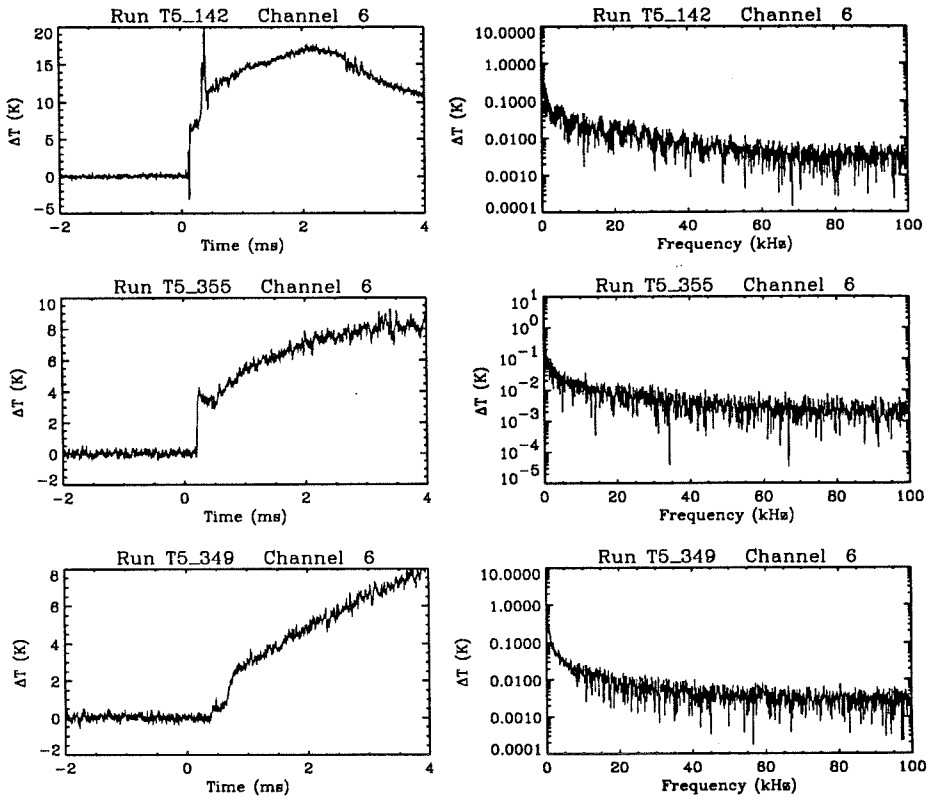

FIG. 7.10. Spectral analysis of three of the time traces presented in Fig. 7.8. If a harmonic frequency was present, it would show in the spectrum as a spike. Clearly, because none is present, the high frequencies content indicates that only broad-band noise is present.

CHAPTER 8

Conclusions

8.1 Summary

In this chapter, a summary is presented together with the conclusions obtained from this experimental work. The first chapter is a review of earlier investigations made in connection with this project. The first part concerns the laminar boundary layer with an emphasis on real-gas effects on the heat transfer rate at the model surface. The second part concerns several possible scenarios to explain the transition of the boundary layer from the laminar to the turbulent regime on a sharp cone. Most of the experimental investigations covered were conducted in continuous-flow facilities where $h_0 < 1$ MJ/kg (whereas the T5 facility generates h_0 up to 25 MJ/kg). Some of these investigations have confirmed results obtained from the linear stability theory extended to compressible flows. Finally, the third part concerns the hypersonic turbulent boundary layer. This particular review is aimed at understanding whether or not approximation methods valid for the supersonic turbulent regime are still applicable in the Mach number range of concern here for predicting the surface heat transfer level.

The second chapter presents a description and discussion of selected methods to predict the heat transfer rate in the different regimes in the limits of a frozen gas as well as for equilibrium gas behavior. An approximate prediction method has been adapted to high-enthalpy flows on a sharp cone for the latter case.

The third chapter gives a description of the shock tunnel facility T5 as well as the instrumentation used (including pressure transducers and surface thermocouples). A new qualitative flow visualization system is also described. The new system is similar to conventional flow visualization system (like differential interferometry or shadowgraphy) except that part of the flow (the boundary layer for instance) is seeded with a tracer which will either absorb the source light or cause significant change in its index of refraction. The source light wavelength was tuned specifically for this purpose. This technique has been called the resonant enhancement of the refractive index of the medium.

The next three chapters gives a presentation of the experimental results. These chapters are divided according to the nature of the boundary layer (laminar, transitional and turbulent). Figs. 8.1 and 8.2 show, for nitrogen and air respectively, some heat transfer measurements from these three chapters. The plots show how broad the survey of these measurements was in the Re range and h_0 range.

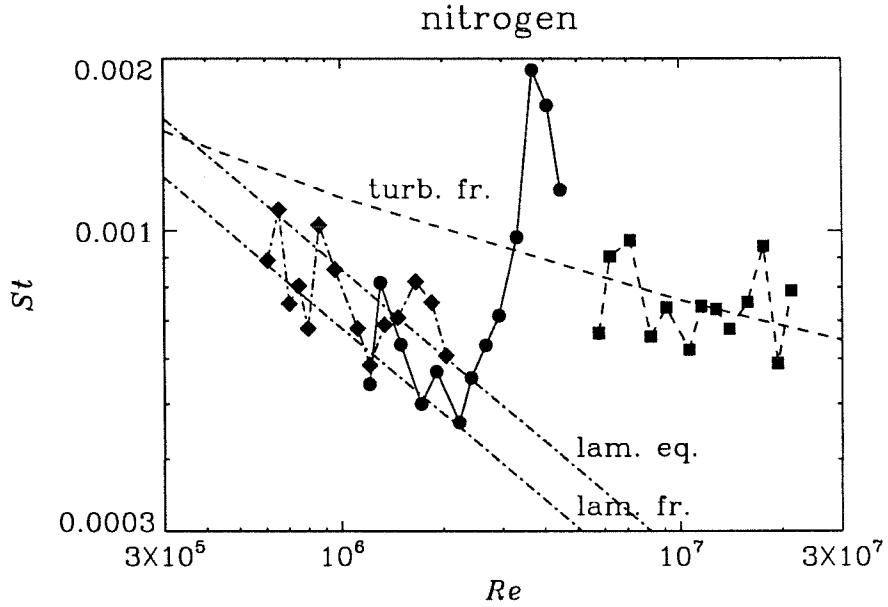

FIG. 8.1. Normalized heat transfer measurements of three different shots in T5 at p_0 = 55 MPa. Squares (run 349): h_0 = 3.5 MJ/kg and p_0 = 47 MPa; circles (run 533): h_0 = 11 MJ/kg and p_0 = 55 MPa; diamonds (run 140): h_0 = 22 MJ/kg and p_0 = 60 MPa. The theoretical predictions for runs 349 and 140 are also plotted.

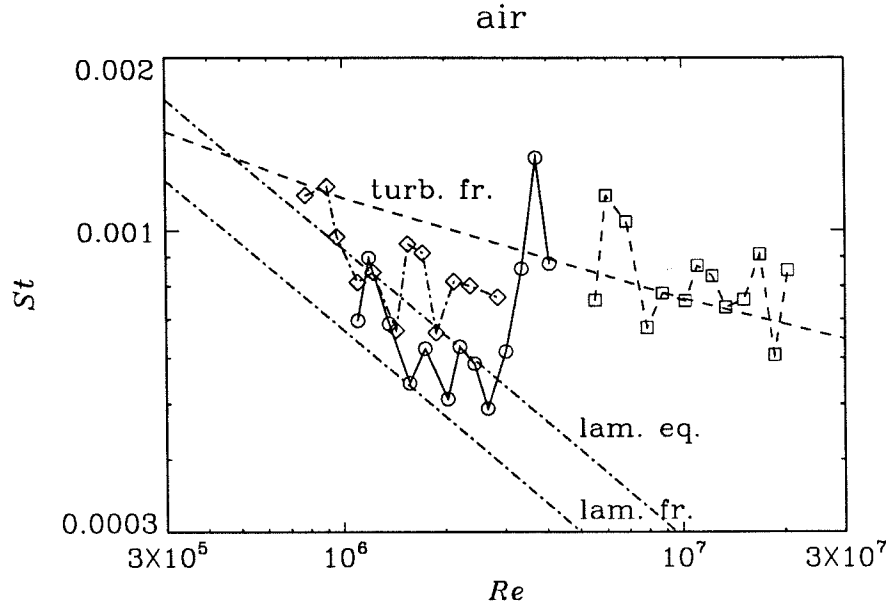

FIG. 8.2. Normalized heat transfer measurements of three different shots in T5 at p_0 = 55 MPa. Squares (run 336): h_0 = 3.4 MJ/kg and p_0 = 42 MPa; circles (run 554): h_0 = 12 MJ/kg and p_0 = 55 MPa; diamonds (run 157): h_0 = 19 MJ/kg and p_0 = 60 MPa. The theoretical predictions for runs 336 and 157 are also plotted.

Conclusions

Flow visualization and wall heat flux measurements were used to study the laminar, transitional, and turbulent boundary layers on a slender cone in high-enthalpy flow of air, nitrogen, and carbon dioxide.

High-enthalpy real-gas effects on the heat flux in the boundary layer were clearly in evidence for laminar and transitional flows. As either pressure or enthalpy were increased, recombination heat flux could be increased. The recombination of atomic species (an exothermic chemical reaction) near the cold wall causes an additional heat release, as detected by surface temperature measurements. The presence of these atomic species is due to the combined effects of free-stream dissociation and frictional heating in the boundary layer. In similar experiments with the same reservoir conditions but with α_e = 0, it is presumed that the real-gas effects already observed would be qualitatively the same. The enthalpy at which real-gas effects appear is lower for gases whose lower dissociation energy is lower. The results follow approximately the predictions according to similarity theory.

The results on the transition location can be correlated by using the reference temperature concept. Evaluation of the transition Reynolds number at the reference temperature appears to remove the dependence of the transition Reynolds number on the Mach number, the ratio of specific heats, the Prandtl number, and wall-to-reservoir temperature ratio. This correlation collapses the data for each gas in a plot of the renormalized Reynolds number against reservoir enthalpy. The boundary layer is significantly stabilized by an enthalpy increase. The lower the lowest dissociation energy of the gas, the faster does the renormalized transition Reynolds number increase with reservoir enthalpy. The unit Reynolds number effect observed in some facilities is absent in our experiments.

The flow visualization experiments clearly show that the Tollmien-Schlichting mode is the dominant instability mode in these experiments. The presence of this mode is consistent with the linear stability theory which predicts that this mode is stabilized by real-gas effects. For flows in the T5 facility, this theory predicts also that the mode with the highest growth rate at high Mach number (especially when real-gas effects are present), the second mode, is sensitive to very high frequency free-stream noise (1 MHz). Since the boundary layer is stabilized by real-gas effects and since noise at high frequency is unlikely to be present in this facility, we conclude that the second mode does not dominate the transition process. This conclusion is consistent with the linear stability theory.

The flow visualization produced pictures showing the structure of the transitional and turbulent boundary layer. Many of the same features are observed in the turbulent boundary layer as in low speed flows. To our knowledge, these are the first turbulent boundary layer structure photographs from hypervelocity flows.

Future work

Linear stability calculations, that include high-enthalpy real-gas effects, need to be performed to check the values of the growth rates of the various instability modes for the present test conditions. These calculations will probably not confirm the observations made in this project. It would also be important to characterize the spectrum of the free-stream perturbations which are a very important factor in determining the nature of the transition process. More runs need to be performed with different gases to confirm the 'picture' of the transition process outlined in this work. The cone model needs to be instrumented with more thermocouples whose signal-to-noise ratio is improved at high specific enthalpy. Similarly, a flat plate needs to be instrumented to compare the two Re^*_{tr} versus h_0 distributions. It is possible that a flat plate flow is more sensitive to free-stream noise as the frequency associated to the second mode is known to be lower in low specific enthalpy facilities ($h_0 < 1$ MJ/kg). Therefore, the transition process would be different than that on a sharp cone.

References

Anderson, J. D. (1989) *Hypersonic and High Temperature Gas Dynamics*, McGraw-Hill, New York.

Beckwith, I. E. (1975) "Development of a high Reynolds number quiet tunnel for transition research", *AIAA Journal* **13** (3), 300-306.

Beckwith, I. E. (1990) "Aerothermodynamics and transition in high-speed wind tunnels at NASA Langley", *Annual Review of Fluid Mechanics* **22**, 419-439.

Blenstrup, G., Bershader, D. and Langhoff, P. (1979) "Recent results of resonant refractivity studies for improved flow visualization", *Proceedings of the 12th International Symposium on Shock Tubes and Waves*, Jerusalem, Israel.

Blottner, F. G. (1964) "Chemical nonequilibrium boundary layer", *AIAA Journal* **2** (2), 232-240.

Bradshaw, P. (1977) "Compressible turbulent shear layers", *Annual Review of Fluid Mechanics* **9**, 33-54.

Cary, A. M. and Bertram, M. H. (1974) "Engineering prediction of a turbulent skin friction and heat transfer in high-speed flow", *NASA Technical Note* D-7507.

Demetriades, A. (1968) "Turbulence measurements in an axisymmetric compressible wake", *Physics of Fluids* **11** (9), 1841-1852.

Demetriades, A. and Laderman, A. J. (1973) "Reynolds stress measurements in a hypersonic boundary layer", *AIAA Journal* **11** (11), 1594-1596.

Demetriades, A. (1974) "Hypersonic viscous flow over a slender cone, Part III: Laminar instability and transition", *AIAA 7th Fluid and Plasma Dynamics Conference, AIAA Paper* 74-535, Palo Alto, California.

Demetriades, A. (1977) "Laminar boundary layer stability measurements at Mach 7 includ-

ing wall temperature effects", Rept. AFOSR-TR-77-1311, Air Force Office of Scientific Research, Washington, D. C.

DiCristina, V. (1970) "Three-dimensional laminar boundary-layer transition on a sharp 8° cone at Mach 10", *AIAA Journal* **8** (5), 852-856.

Dorrance, W. H. (1962) *Viscous Hypersonic Flow*, McGraw-Hill, New York.

East, R. A., Stalker, R. J. and Baird, J. P. (1980) "Measurements of heat transfer to a flat plate in a dissociated high-enthalpy laminar air flow", *Journal of Fluid Mechanics* **97**, 673-699.

Eckert, E. R. G. (1955) "Engineering relations for friction and heat transfer to surfaces in high velocity flow", *Journal of the Aeronautical Sciences* **22**, 585-587.

Fedorov, A. V. (1993) Private communication, Moscow Institute of Physics and Technology, Moscow, Russia.

Gai, S. L. and Joe, W. S. (1992) "Laminar heat transfer to blunt cones in high-enthalpy hypervelocity flows", *AIAA Journal of Thermophysics and Heat Transfer* **6** (3), 433-438.

He, Y. and Morgan, R. G. (1989) "Transition of compressible high enthalpy boundary layer over a flat plate", 10th Australasian Fluid Mechanics Conference, University of Melbourne, Australia.

Head, M. R. and Bandyopadhyay, P. (1981) "New aspects turbulent boundary-layer structure", *Journal of Fluid Mechanics* **107**, 297-338.

Hornung, H. G. (1992) "Performance data of the new free-piston shock tunnel at GALCIT", *AIAA 17th Aerospace Ground Testing Conference, AIAA Paper* 90-3943, Nashville, Tennessee.

Hornung, H. G. and Bélanger, J. (1990) "Role and techniques of ground testing for simulation of flows up to orbital speed", *AIAA 16th Aerodynamic Ground Testing Conference, AIAA Paper* 90-1377, Seattle, Washington.

Johnson, D. A. (1959) "Turbulence measurements in a Mach 2.9 boundary layer using laser velocimetry", *AIAA Journal* **12** (5), 711-714.

Keener, E. R. and Polek, T. E. (1972) "Measurements of Reynolds analogy for a hypersonic turbulent boundary layer on a non-adiabatic flat plate", *AIAA Journal* **10** (6), 845-846.

Kemp, J. H. and Owen, F. K. (1972) "Nozzle wall boundary layers at Mach numbers 20 to 47", *AIAA Journal* **10** (7), 872-879.

Kendall, J. M. (1975) "Wind tunnel experiments relating to supersonic and hypersonic boundary-layer transition", *AIAA Journal* **13** (3), 290-299.

King, R. A. (1992) "Three-dimensional boundary-layer transition on a cone at Mach 3.5", *Experiments in Fluids* **13**, 305-314.

Kistler, A. L. (1959) "Fluctuation measurements in a supersonic turbulent boundary layer", *Physics of Fluids A* **2** (3), 290-296.

Laderman, A. J. (1974) "Hypersonic viscous flow over a slender cone, Part II: Turbulence structure of the boundary layer", *AIAA 7th Fluid and Plasma Dynamics Conference, AIAA Paper* 74-534, Palo Alto, California.

Liepmann, H. W. and Roshko, A. (1957) *Elements of Gas Dynamics*, Wiley, New York.

Lighthill, M. J. (1957) "Dynamics of dissociating gas. Part I. Equilibrium flow", *Journal of Fluid Mechanics* **2**, 1-32.

Lin, Z. B. and Harvey, J. K. (1989) "Experimental study of the hypersonic turbulent boundary layer on a cold slender cone", *AIAA Journal of Thermophysics and Heat Transfer* **3**, (2), 105-111.

Mack, L. M. (1969) "Boundary layer stability", *Rept.* 900-277 *Rev.* A, *Jet Propulsion Laboratory*, Pasadena, California.

Mack, L. M. (1986) "Boundary layer stability analysis for sharp cones at zero angle-of-attack", *Rept.* AFWAL-TR-86-3022, Air Force Flight Dynamics Lab., Wright-Patterson Air Force Base, Ohio.

Maestrello, L., Bayliss, A. and Krishnan, R. (1991) "On the interaction between first- and second-mode waves in a supersonic boundary layer", *Physics of Fluids A* **3** (12), 3014-3020.

Malik, M. R. and Anderson, E. C. (1991) "Real gas effects on hypersonic boundary-layer stability", *Physics of Fluids A* **3**, 803-821.

Malik, M. R. and Spall, R. E. (1991) "On the stability of compressible flow past axisymmetric bodies", *Journal of Fluid Mechanics* **228**, 443-463.

Mangler, W. (1948) "Zusammenhang zwischen ebenen und rotationssymmetrischen Grenzschichten in kompressiblen Flüssigkeiten", *Zeitschrift für Angewandte Mathematik und Mechanik* **28** (4), 97-103.

Martellucci, A. and Laganelli, A. L. (1974) "Hypersonic viscous flow over a slender cone, Part I: Mean flow mesurements", *AIAA 7th Fluid and Plasma Dynamics Conference, AIAA Paper* 74-533, Palo Alto, California.

McIntosh, M. K. (1970), "A computer program for the numerical calculation of equilibrium and perfect gas conditions in shock tunnels", Australian Defence Scientific Service, *Technical Note* CPD 169, Salisbury, South Australia.

Morgan, R. G. and Stalker, R. J. (1986) "Shock tunnel measurements of heat transfer in a model scramjet", *AIAA Journal of Spacecraft and Rockets* **23** (5), 470-475.

Morkovin, M. V. (1969) "Critical evaluation of transition from laminar to turbulent shear layers with emphasis on hypersonically travelling bodies", *Rept.* AFFDL-TR-68-149, Air Force Flight Dynamics Lab., Wright-Patterson Air Force Base, Ohio.

Omega Engineering, Inc. (1992) *The Temperature Handbook*, 28th edition, Stamford, Connecticut.

Owen, F. K. (1970) "Transition experiments on a flat plate at subsonic and supersonic speeds", *AIAA Journal* **8** (3), 518-523.

Owen, F. K. and Horstman, C. C. (1972) "On the structure of hypersonic turbulent boundary layers", *Journal of Fluid Mechanics* **53**, 611-636.

Owen, F. K., Horstman, C. C., Stainback, P. C. (1975) "Comparison of wind tunnel transition and freestream disturbance measurements", *AIAA Journal* **13** (3), 266-269.

Park, C. (1990) *Nonequilibrium Hypersonic Aerothermodynamics*, Wiley, New York.

Pate, S. R. (1971) "Measurements and correlations of transition Reynolds numbers on sharp slender cones at high speeds", *AIAA Journal* **9** (6), 1082-1090.

Potter, J. L. (1975) "Boundary-layer transition on supersonic cones in an aeroballistic range", *AIAA Journal* **13** (3), 270-277.

Pruett, C. D. and Ng, L. L. (1991) "On the stability of a high-speed, axisymmetric boundary layer", *Physics of Fluids A* **3** (12), 2910-2926.

Rein, M. (1989) "SURF: A program for calculating inviscid supersonic reacting flows in nozzles", *GALCIT Report* FM 89-1, Graduate Aeronautical Laboratories, California Institute of Technology, Pasadena, California.

Reshotko, E. (1976) "Boundary-layer stability and transition", *Annual Review of Fluid Mechanics* **8**, 311-349.

Reynolds, W. C. (1981) "STANJAN, Interactive computer programs for chemical equilibrium analysis", Thermosciences Division, Department of Mechanical Engineering, Stanford University, Stanford, California.

Rose, W. C. (1974) "Turbulence measurements in a compressible boundary layer", *AIAA Journal* **12** (8), 1060-1064.

Rousset, B. and Adam, P. (1993) "Electre experiments in T5", *GALCIT Report* FM 93-2, Graduate Aeronautical Laboratories, California Institute of Technology, Pasadena, California.

Schlichting, H. (1979) *Boundary-layer Theory*, McGraw-Hill, New York.

Schubauer, G. B. and Skramstad, H. K. (1947) "Laminar boundary-layer oscillations and stability of laminar flow", *Journal of the Aeronautical Sciences* **14** (2), 69-78.

Schultz, D. L. and Jones, T. V. (1973) "Heat transfer measurements in short duration facilities", *AGARD Report* 165.

Simen, M. and Dallmann, U. (1992) "On the instability of hypersonic flow past a pointed cone - Comparison of theoretical and experimental results at Mach 8", DLR, Institüt fur Theoretische Strömungsmechanik, DLR-FB 92-02, Göttingen, Germany.

Skinner, K. A. (1992) "Species measurement using mass spectrometry in high Mach number flows", *11th Australasian Fluid Mechanics Conference*, University of Tasmania, Australia.

Slade, J. C., Crane, K. C. and Stalker, R. J. (1993) "Driver gas detection by quadrupole mass spectrometry in shock tunnels", *Proceedings of the 19th International Symposium on Shock Tubes and Waves*, Marseille, France.

Smeets, G. and George, A. (1973) "Investigation of shock boundary layers with a laser interferometer", *Proceedings of the 9th International Symposium on Shock Tubes and Waves*, Stanford, California.

Stetson, K. F. and Rushton, G. H. (1967) "Shock tunnel investigation of boundary layer transition at M = 5.5", *AIAA Journal* **5** (5), 899-906.

Stetson, K. F., Thompson, E. R. and Donaldson, J. C. (1983) "Laminar boundary layer stability experiments on a cone at Mach 8, Part 1: Sharp cone", *AIAA 16th Fluid and Plasma Dynamics Conference, AIAA Paper* 83-1761, Danvers, Massachusetts.

Stetson, K. F., Thompson, E. R., Donaldson, J. C. and Siler, L. G. (1986) "Laminar boundary layer stability experiments on a cone at Mach 8, Part 4: On unit Reynolds number and environmental effects", *AIAA/ASME 4th Fluid Mechanics, Plasma Dynamics and Laser Conferences, AIAA Paper* 86-1087, Atlanta, Georgia.

Stetson, K. F. (1988) "On non-linear aspects of hypersonic boundary-layer stability", *AIAA Journal* **26** (7), 883-885.

Stetson, K. F., Thompson, E. R., Donaldson, J. C. and Siler, L. G. (1989) "Laminar boundary layer stability experiments on a cone at Mach 8, Part 5: Tests with a cooled model", *AIAA 20th Fluid Dynamics, Plasma Dynamics and Lasers Conference, AIAA Paper* 89-1895, Buffalo, New York.

Stetson, K. F. and Kimmel, R. L. (1992) "On hypersonic boundary-layer stability", *AIAA 30th Aerospace Sciences Meeting and Exhibit, AIAA Paper* 92-0737, Reno, Nevada.

Stetson, K. F. (1993) Private communication, Air Force Flight Dynamics Lab., Wright-Patterson Air Force Base, Ohio.

Stuckert, G. K. and Reed, H. L. (1990) "Stability of hypersonic, chemically reacting viscous flows", *AIAA 21st Fluid Dynamics, Plasma Dynamics and Lasers Conferences, AIAA Paper* 90-1529, Seattle, Washington.

Taylor, G. I. and Maccoll, J. W. (1933) "The air pressure on a cone moving at high speed", *Proceedings of the Royal Society (London) ser. A* **139**, 278-311.

Van Driest, E. R. (1952) "Turbulent boundary layer on a cone in a supersonic flow at zero angle of attack", *Journal of the Aeronautical Sciences* **19** (1), 55-57.

Van Driest, E. R. (1956) "The problem of aerodynamic heating", *Aeronautical Engineering Review* **15** (10), 26-41.

Van Driest, E. R. (1959) "Convective heat transfer in gases", *High Speed Aerodynamics and Jet Propulsion* **5**: *Turbulent Flows and Heat Transfer*, Princeton, New Jersey.

Vidal, R. J. and Golian, T. C. (1967) "Heat-transfer measurements with a catalytic flat plate in dissociated oxygen", *AIAA Journal* **5** (9), 1579-1588.

Vincenti, W. G. and Kruger, C. H. (1965) *Introduction to Physical Gas Dynamics*, Wiley, New York.

Wen, C. Y. and Hornung, H. G. (1993) "Experiments on hypervelocity dissociating flow over spheres", *Proceedings of the 19th International Symposium on Shock Tubes and Waves*, Marseille, France.

White, F. M. (1974) *Viscous Fluid Flow*, McGraw-Hill, New York.